

COHERENT LIGHT GENERATION IN RAMAN-ACTIVE CRYSTALS AND  
HOLLOW-CORE OPTICAL FIBERS DRIVEN BY ULTRAFAST LASERS

A Dissertation

by

AYSAN BAHARI MORADALA

Submitted to the Graduate and Professional School of  
Texas A&M University  
in partial fulfillment of the requirements for the degree of  
DOCTOR OF PHILOSOPHY

Chair of Committee,	Alexei V. Sokolov
Co-Chair of Committee,	Marlan O. Scully
Committee Members,	Alexey M. Zheltikov
	M. Suhail Zubairy
	Philip Hemmer
Head of Department,	Grigory Rogachev

May 2023

Major Subject: Physics

Copyright 2023 Aysan Bahari Moradala

## ABSTRACT

The integration of short laser pulses with crystals and photonic crystal structures offers a versatile platform for exploring fundamental light-matter interactions and discovering novel techniques in ultrashort pulse generation and shaping, as well as spectroscopy. In this thesis, I will first discuss the coherent generation of a broad spectrum in Raman-active crystals such as lead tungstate ( $\text{PbWO}_4$ ) and single-crystal diamond, which enables us to study the transfer of orbital angular momentum (OAM) of light in ultrashort shaped pulses through coherent Raman processes as well as near-single-cycle pulse generation with pulses as short as 4.8 femtoseconds (fs) and ability to be shaped temporally and spatially. We characterize these pulses through a nonlinear technique called interferometric cross-correlated frequency-resolved optical gating (ix-FROG). Multi-photon ionization is another reliable technique to characterize our synthesized near-single-cycle pulse. As proof of principle, we perform mass spectroscopy on xenon ionized by our ultrashort pulses. In this thesis, we study another nonlinear interaction in Raman media in the form of picosecond (ps) coherent anti-stokes Raman scattering (CARS) spectroscopy in hollow-core photonic crystal fibers (HC-PCFs) and hollow-core fibers (HCFs). CARS spectroscopy is a reliable nonlinear technique that probes the vibrational and rotational modes of a target molecule, enabling chemical-selective microscopy and spectroscopy. We take advantage of hollow-core optical fibers to enhance the CARS signal in gaseous media up to two orders of magnitude. We also conduct a similar study on biological analytes such as Immunoglobulin G (IgG) antibody samples. I will introduce a type of HCF called anti-resonance HCF (AR-HCF), which provides low-loss broadband light guidance for relatively large core diameters. AR-HCF also reduces the pulse energies required for strong nonlinear interactions from the millijoule to the microjoule level, thus, allowing scaling from kHz to MHz repetition rates. I will discuss the results that illustrate the absence of a substantial non-resonant background (NRB), an unavoidable by-product of the CARS spectroscopy, using an AR-HCF.

## DEDICATION

To my husband, Amin, my daughter, Arwen, and my parents.

## ACKNOWLEDGMENTS

My journey would not have been possible without the support of many wonderful people. I would like to thank my advisor and the chair of my committee, Prof. Alexei V. Sokolov for his immense guidance, support, and kindness throughout my Ph.D. I would also like to thank my co-chair Prof. Marlan O. Scully, and my committee members, Profs. Alexey M. Zheltikov, M. Suhail Zubairy, and Philip Hemmer, for their time and consideration. Many thanks to my colleagues Dr. Alexandra Zhdanova, Kyle Sower, Dr. Kai Wang, Dr. Zehua Han, Dr. Mariia Shutova, Dr. Ben Stricker, and Dr. Yujie Shen for their valuable contributions to my work. I am grateful to Prof. Alexey M. Zheltikov, Dr. Kai Wang, Dr. Zhenhuan Yi, and Navid Rajil for valuable discussions. I also acknowledge Profs. Artem Abanov, David Lee, and Glen Agnolet for believing in me when I did not. In addition, I thank Dr. Tian Liu for lending me lots of tools and optics, generously. I would also like to thank the staff at the Department of Physics and Astronomy, IQSE, the Office of Graduate and Professional Studies, and Texas A&M High-Performance Research Computing for their assistance and support throughout my graduate studies.

I am very lucky to have such wonderful and supportive friends; thank you Dr. Elham Azadbakht, Bassam Aboona, and Prof. Kim Vy Tran. I also extend my sincere thanks to my lovely parents, my amazing sisters Sarah and Samira, and my brother Babak who always encouraged me to continue my hard work at times when I felt discouraged and unmotivated.

Thanks should also go to my cat, Rory, for her cuddles and purrs during the most stressful times, and to my beautiful daughter, Arwen, for teaching me valuable lessons that no one ever could; through motherhood, I learned about the strength I did not know I had. And last but not least, my spatial appreciation goes to my husband, and my best friend, Dr. Amin Barzegar. Without his unconditional love and support, I could not have undertaken this journey and been here.

## CONTRIBUTORS AND FUNDING SOURCES

### **Contributors**

This work was supported by a dissertation committee consisting of Profs. Alexie V. Sokolov (advisor), Marlan O. Scully (co-advisor), Alexey M. Zheltikov, and M. Suhail Zubairy from the Department of Physics and Astronomy, and Prof. Philip Hemmer from the Electrical and Computer Engineering Department.

The data in Chapter 3 was collected and analyzed in collaboration with Dr. Alexandra A. Zhdanova from Google and Dr. Mariia Shutova from Apple. This work was published in Optics Express in 2015.

The data in Chapters 4, 5, and 6 is collected and analyzed in collaboration with Dr. Alexandra A. Zhdanova and was published in the Physical Review A. Journal in 2020.

The data collection depicted in chapters 8 and 9 is performed in collaboration with Kyle Sower from the Department of Physics and Astronomy of Texas A&M University. This work was published in the Optics Letters Journal in 2022.

The rest of the co-authors on the aforementioned publications contributed to data analysis, discussions, and preparing the manuscripts. All other work conducted for this dissertation was completed by the student independently.

### **Funding Sources**

Graduate study was supported by funding from the National Science Foundation (grants No. PHY-1307153 and CHE-1609608), Welch Foundation (grant No. A-1547), the Stephen E. Harris Professorship in Quantum Optics (held by Prof. Alexei V. Sokolov), and the Herman F. Heep and Minnie Belle Heep Texas A&M University Endowed Fund held/administered by the Texas A&M Foundation.

## NOMENCLATURE

AS	Anti-Stokes
as	Attosecond
a.u.	Arbitrary Unit
BBO	Beta Barium Borate
CARS	Coherent anti-Stokes Raman scattering
CCD	Charge-coupled device
CEM	Channeltron Electron Multiplier
CEP	Carrier Envelope Phase
FEM	Finite-element Modeling
FFT	Fast Fourier Transform
FROG	Frequency Resolved Optical Gating
fs	Femtosecond
FTL	Fourier-Transform Limited
FWHM	Full-Width at Half-Maximum
FWM	Four Wave Mixing
GVD	Group Velocity Dispersion
ix-FROG	interferometric cross-correlation Frequency Resolved Optical Gating
kHz	Kilo Hertz
LCM	Liquid crystal modulator
LCOS	Liquid Crystal on Silicon
LMA	Large-Mode Area

LPF	Long-Pass Filter
MHz	Mega Hertz
MSLD	Mass Spectrometer Leak Detector
NA	Numerical Aperture
NDF	Nutral Density Filter
OAP	Off-Axis Parabola
OAM	Orbital Angular Momentum
OPA	Optical Parametric Amplifier
PbWO <sub>4</sub>	Lead Tungstate
PCF	Photonic Crystal Fiber
PCGP	Principal Component Generalized Projections
PS	Polystyrene
ps	Picosecond
RMS	Root Mean Square
SAM	Spin Angular Momentum
SEM	Scanning Electron Microscope
SFG	Sum Frequency Generation
SHG	Second Harmonic Generation
SLM	Spatial Light Modulator
SNR	Signal to Noise Ratio
SPF	Short-Pass Filter
St	Stokes
TAMU	Texas A& M University
TC	Topological Charge
TOF	Time of Flight

Xe

XFROG

ZDW

Xenon

Cross Correlation Frequency Resolved Optical Gating

Zero Dispersion Wavelength

## TABLE OF CONTENTS

	Page
ABSTRACT .....	ii
DEDICATION .....	iii
ACKNOWLEDGMENTS .....	iv
CONTRIBUTORS AND FUNDING SOURCES .....	v
NOMENCLATURE .....	vi
TABLE OF CONTENTS .....	ix
LIST OF FIGURES .....	xii
LIST OF TABLES.....	xv
1. INTRODUCTION.....	1
2. BASIC CONCEPTS.....	4
2.1 Broadband coherent light generation in Raman media .....	4
2.2 Coherent sideband generation in Raman-active crystals .....	4
2.3 Ultrashort Pulse Measurement.....	8
2.3.1 Frequency-Resolved Optical Gating (FROG) .....	9
2.3.2 Generalized Projections Algorithm .....	9
2.4 Orbital angular momentum of light .....	12
2.5 Coherent Anti-Stokes Raman Spectroscopy .....	13
2.5.1 Wave-guided CARS .....	16
2.5.2 Photonic Fiber Modes .....	19
2.5.3 Anti-resonant Guidance .....	22
2.6 Summary .....	25
3. TOPOLOGICAL CHARGE TRANSFER IN COHERENT RAMAN PROCESSES IN PbWO <sub>4</sub> CRYSTAL .....	26
3.1 Introduction.....	26
3.2 TC Transfer in Raman Processes .....	28
3.3 Experimental Setup .....	28
3.3.1 Optical Vortex Production.....	30
3.3.2 Tilted Bi-Convex Lens Technique .....	33

3.4	Results and Discussion.....	34
3.5	Summary and Conclusion .....	37
4.	SYNTHESIS OF ULTRAFAST WAVEFORMS USING COHERENT RAMAN SIDE-BANDS .....	38
4.1	Introduction.....	38
4.2	Experimental setup.....	40
4.3	ix-FROG pulse retrieval.....	43
4.4	Results .....	47
4.5	Conclusions.....	48
5.	TOWARDS ULTRASHORT PULSES BY SYNTHESIZING COHERENT RAMAN SIDEBANDS .....	49
5.1	Introduction.....	49
5.2	Experimental Setup .....	49
5.3	SHG-FROG and x-FROG Traces .....	54
5.4	Beat Notes Analysis.....	56
5.5	conclusion .....	65
6.	MULTI-PHOTON IONIZATION IN XENON USING SYNTHESIZED NEAR SINGLE-CYCLE PULSES GENERATED IN RAMAN INTERACTION .....	66
6.1	Introduction.....	66
6.2	Vacuum Chamber Preparation .....	67
6.3	Beams overlap potential solution .....	71
6.4	Experimental Setup .....	71
	6.4.1 Main Setup Description .....	71
	6.4.2 Channeltron Description .....	72
6.5	Results .....	74
6.6	Conclusion.....	76
7.	PRESSURE CONTROLLED PHASE MATCHING IN KAGOMÉ PC FIBER IN PICOSECOND CARS.....	77
7.1	Introduction.....	77
7.2	Theoretical Framework .....	77
7.3	Results and discussion .....	79
8.	BACKGROUND-PENALTY-FREE WAVE-GUIDE ENHANCEMENT OF CARS SIGNAL IN AIR-FILLED ANTI-RESONANCE HOLLOW-CORE FIBER .....	80
8.1	Introduction.....	80
8.2	AR-HCF Properties .....	82
8.3	Experimental Setup .....	84
8.4	Results .....	86

8.5	Conclusion.....	89
9.	COHERENT ANTI-STOKES RAMAN SPECTROSCOPY IN HOLLOW-CORE PHOTONIC CRYSTAL FIBERS .....	90
9.1	Introduction.....	90
9.2	HC-1060 PCF .....	91
9.2.1	Photonic Bandgap Wave-Guiding Mechanism.....	91
9.2.2	HC-1060 PCF Properties.....	92
9.3	AR-HCF (Revolver).....	95
9.4	Stack and Draw Technique .....	99
9.5	Gas Cell for Pressure controlled CARS.....	100
9.6	CARS in AR-HCPCF filled with Goat Anti-Human IgG Antibody .....	102
9.7	Conclusion and Future Work .....	106
10.	SUMMARY AND FUTURE WORK .....	107
	REFERENCES .....	108
	APPENDIX A. BASIC ALIGNMENT METHODS .....	125
	APPENDIX B. USING CARS MICROSCOPE FOR BEAM ALIGNMENT .....	130
B.1	CARS Microscope Description.....	130
B.2	Beam alignment method .....	130

## LIST OF FIGURES

FIGURE	Page
2.1 Generation of Raman sidebands in single-crystal diamond .....	6
2.2 Schematic of two simple setups for frequency-resolved optical-gating (FROG) and cross-correlation FROG (XFROG) .....	10
2.3 Laguerre-Gaussian modes ( $L_{pl}$ ).....	14
2.4 Energy diagrams for coherent anti-Stokes Raman scattering (CARS) and the associated non-resonant background (NRB) generation .....	15
2.5 Several types of micro-structured photonic crystal fibers .....	17
2.6 AR-HCF SEM image and the anti-resonance mechanism .....	23
3.1 Optical vortices and their computer-generated phase masks .....	29
3.2 Experimental setup for the generation of the vortex Raman sidebands in $PbWO_4$ crystal.....	32
3.3 Tilted bi-convex lens technique to measure the TC of vortex Raman sidebands.....	34
3.4 Generation of the first sideband (AS1) in the Raman process using two modulated beams .....	36
4.1 Experimental setup to synthesize a sub-5-fs FWHM pulse .....	41
4.2 Experimental XFROG spectrograms of all beams employed in the Raman sidebands synthesis setup .....	44
4.3 Ultrafast waveform analysis .....	46
5.1 The experimental setup for the synthesis of a near-single-cycle pulse by adding 7 coherent Raman sidebands collinearly. ....	50
5.2 Real photograph of the Generation of the coherent Raman sidebands in diamond ....	51
5.3 Spectrum of the SFG of the reference and AS2 beams.....	52
5.4 Spectra of all the coherent Raman sidebands .....	55

5.5	x-FROG spectrograms of each sideband taken after the 10-micron BBO crystal.....	57
5.6	Retrieved pulse phase and retrieved pulse envelope for all coherent Raman sidebands	58
5.7	Synthesized pulse produced from the linear combination of 7 coherent Raman sidebands.....	59
5.8	Comparison of the theoretical and experimental interferograms of different combinations of the nonlinear signals (SHGs and SFGs) of the sidebands .....	60
5.9	Time resolved interferograms of the nonlinear signals (SHG and SFG) of the 6 sidebands (S1, Ref, AS1-4) .....	61
5.10	Time-resolved interferograms of 6 beams (S1, Ref, AS1-4). .....	62
5.11	Four interferograms resulted from different interference between the nonlinear signals. ....	63
5.12	Interferograms of the SFG of AS1 + AS3 with SHG of AS2 while tuning AS3's delay stage and AS1's delay stage in 1 mm BBO at the same time resolution. ....	64
6.1	Vacuum chamber used for the Xe ionization experiment.....	70
6.2	Experimental setup used for phase-controlled multi-photon ionization in xenon in a pressure-controlled ( $\sim 10^{-7}$ mbar) vacuum chamber.....	72
6.3	Channeltron.....	73
6.4	First trial of measuring the TOF from the mass spectroscopy .....	74
6.5	TOF Spectrograms measured by an oscilloscope of the photonized species detected in Xe gas using the FTL pulse .....	75
6.6	TOF spectra dependence of the photonized Xe gas on the Ref beam's power .....	76
7.1	Calculated GVD of air-filled Kagome fiber, comparison of the experimental and calculated D factor of air-filled Kagome fiber, phase mismatch factor as a function of Raman shift and pressure for Argon-, Krypton-, Nitrogen-, and air-filled Kagome fiber .....	79
8.1	Properties of the AR-HCF used in our experiment .....	83
8.2	Schematic of our experimental wave-guided CARS setup .....	85
8.3	The CARS signal of nitrogen at $2331\text{ cm}^{-1}$ (Q-branch vibrational transition) in a 2.96 cm long air-filled AR-HCF compared to the CARS signal from the ambient air (no fiber present).....	87

9.1	Properties of HC-1060 originally used for this experiment. ....	93
9.2	Spectra of the SC generated in an LMA fiber which is used as the Stokes beam before (green) and after (red) a 3-cm-long HC-1060 HCPCF. ....	94
9.3	Characterizations of three AR-HCFs by the manufacturer. ....	95
9.4	Spectra of the SC generated in an LMA fiber which is used as the Stokes beam before (red) and after (purple) a 2.96-cm-long AR-HCF. ....	96
9.5	Transmission Loss for AR-HCF. ....	97
9.6	The Stack-and-draw technique used for manufacturing an AR-HCF. ....	98
9.7	Coherence length calculated and plotted as a function of wavelength for an air-filled AR-HCF. ....	99
9.8	CARS setup and the 3D-printed gas cell. ....	100
9.9	Beam profiles of the pump and Stokes beams after the air-filled revolver fiber. ....	101
9.10	The schematic of the IgG-filled AR-HCPCF's interior filled with two different methods. ....	103
9.11	Process of filling AR-HCF with goat anti-human IgG antibody. ....	104
9.12	The Raw data from an IgG sample on a glass substrate (blue curve) compared to a 2.96 cm IgG-filled AR-HCPCF (the red curve is scaled to be comparable with the blue curve). ....	105
A.1	The overlapping procedure of the pump and Stokes in the BBO and the diamond crystals to generate the multi-color Raman sidebands. ....	126
A.2	The OPA panel allows the generation of pulses with adjustable frequencies. ....	127
A.3	SFG signal detection for different combinations of the sideband pairs. ....	129
B.1	Using the CARS microscope to align the fundamental beams. ....	131

## LIST OF TABLES

TABLE	Page
2.1	Properties of the single crystal diamond ..... 8
3.1	TC values of output sidebands and the number and the direction of the bright spots in tilted lens technique for different $l_{Stokes}$ . ..... 30
3.2	Properties of the specific $PbWO_4$ crystal used in the experiment..... 30
3.3	TC values of output sidebands and the number and the direction of the bright spots in tilted lens technique for different $l_{Stokes}$ . ..... 35
3.4	TC values for AS1 as $l_{pump}$ and $l_{Stokes}$ vary. The last column shows the number and the direction of the bright spots after the tilted bi-convex lens verifying the value and the sign of the TC of AS1 in each case. .... 36
4.1	Part numbers for the dichroic mirrors and translation stages; focal lengths for the collimation lenses used in this setup. Part numbers starting with “TL” correspond to Thorlabs part numbers, “NP” - Newport, “EO” - Edmund Optics, and “SR” - Semrock..... 42
5.1	Part numbers for the dichroic mirror and translation stage..... 50
5.2	The power of each sideband after exiting the single-crystal diamond ..... 53
6.1	The measured power and wavelength of each sideband (Ref, Stokes, AS1,2) before entering the pressure-controlled vacuum chamber. .... 67
6.2	The part numbers and descriptions of the vacuum system. All the vacuum parts are from Pfeiffer Vacuum systems and all the pump parts are from Kurt J. Lesker. Manuals are available upon request. OD and ID stand for outer and inner diameters, respectively. P stands for pressure. .... 67
7.1	Experimental values for constants A, B, C, and D for Argon, Krypton, Nitrogen, and air. .... 78
9.1	Physical properties of HC-1060, NKT Photonics..... 92
9.2	Optical properties of HC-1060, NKT Photonics. .... 94

## 1. INTRODUCTION

Coherent nonlinear processes offer a variety of applications in ultrafast laser physics, chemistry, and spectroscopy. The interaction of two mutually coherent and narrowband laser fields offset in frequency with an ensemble of molecules results in Raman transitions. Raman effect is named after Sir Chandrasekhara Venkata Raman, who discovered the inelastic scattering of photons by matter in 1928 [1]. Soon after, he received the 1930 Nobel Prize in physics as the first Asian to receive a Nobel Prize in any field of science. Despite the weakness of Raman scattering compared to Rayleigh scattering (only 1 in  $10^7$  photons get scattered) [2], countless studies have been done following Raman's discovery, and more than 2500 chemical compounds were examined by Raman spectroscopy in the following decades [3].

Although Raman spectroscopy is known for providing valuable information about a sample, its applicability is limited by long integration time or high pump laser power required, which are not ideal for biological samples. On the other hand, coherent Raman spectroscopy is capable of generating much stronger vibrational signals through nonlinear techniques. In coherent Raman spectroscopy, an ensemble of molecules interacts with light coherently, resulting in the molecules vibrating in unison and producing more efficient Raman scattering [4]. The coherent Raman effect has numerous remarkable applications, two of which include broadband coherent Raman production enabling sub-fs pulse generation, and coherent anti-Stokes Raman scattering (CARS) spectroscopy.

Ultrafast time-resolved spectroscopy approached attosecond resolution by the emergence of the near single-cycle phase-controlled laser pulses. The future aspiration of the attoscience is to understand and measure events that occur on the infinitesimal time scale of electron motion. Ultrafast pulses in extreme ultraviolet (EUV) and soft X-Ray regions are possible through the high harmonic generation (HHG) technique; however, this technique cannot produce pulses in the optical region [5]. Ultrafast waveforms in the visible range are essential for sub-cycle field shaping, direct and precise control of electron trajectories in photoionization, and high-order harmonic gen-

eration since their duration is shorter than an optical cycle. Several groups have recently developed advanced techniques to generate single-cycle optical pulses. Some examples of these techniques are optical parametric chirped pulse amplification with pulses as short as 4.2 femtoseconds (fs) [6], self-compressed filaments with 30 fs pulses [7], and divided supercontinuum with 380 attosecond (as) pulses [8]. Molecular modulation is another promising technique that envisions pulses as short as 500 as [9, 10]. This technique relies on adiabatic preparation of molecular coherence to excite a single superposition state of a molecule by driving the molecular transition slightly off-resonance. In turn, molecular motion modulates the frequency of the driving lasers, and a mutually coherent set of colorful Raman sidebands is generated. By using this technique and recombining these sidebands that are frequency-shifted copies of the driving laser, we can synthesize pulses as short as 4.8 fs with desired pulse shape where the electric field's oscillation is not limited to quasi-sinusoidal [11]. In chapter 3, I discuss the spatial shaping of the coherent Raman sidebands and the transfer of the orbital angular momentum (OAM) through the Raman processes. I will detail the generation of near single-cycle pulses with adjustable spectral phase in chapters 4 and 5. Chapter 6 covers our experimental results from the xenon multi-photon ionization using our synthesized pulses.

Another consequential application of the Raman effect is CARS spectroscopy which is non-invasive, label-free, high sensitivity, and high speed, with a much higher signal-to-noise ratio, compared to more traditional spectroscopy. CARS produces a coherent signal using several photons to address the molecular vibrations. As a result, it outperforms spontaneous Raman spectroscopy by several orders of magnitude. In their 1965 paper, P. D. Maker and R. W. Terhune from the Scientific Laboratory at the Ford Motor Company reported the CARS phenomena by detecting a blue-shifted signal from a benzene sample [4]. This signal was produced by two driving laser beams with a frequency difference corresponding to benzene's chemical bond vibrational frequency. The formal name "CAR" was coined a decade later by Begley [12].

The modern form of CARS spectroscopy was not introduced until after the development of new techniques and more advanced laser technology, especially femtosecond lasers [13–15]. A critical factor that played a massive role in improving CARS spectroscopy and expanding its ap-

plications was background suppression [16, 17]. A few examples of many applications of CARS spectroscopy are high-speed imaging of biomedical samples such as cells and tissues [18–22], fast 3D imaging [13], and gas-phase analysis [23]. A prominent advantage of CARS spectroscopy is that the signal is blue-shifted relative to the excitation frequencies. Therefore, it can be easily detected in the presence of the one-photon fluorescence background.

Numerous efforts have been made after the emergence of CARS spectroscopy to improve the signal resolution and overcome limitations such as non-resonant background [16, 17, 24]. One great way to enhance the CARS signal is to use hollow-core photonic crystal fibers (HC-PCFs) and hollow-core fibers (HCFs). The difference between these two classes is the absence of the periodic structure of the cladding in the latter. These optical fibers can enhance the nonlinear optical processes by providing high degrees of light confinement in a few-micron scale of their hollow core for long distances [25, 26]. Moreover, their cladding can be designed with desired dispersion properties for further enhancements [27, 28]. CARS in HC-PCF and HCF is extendable to various multi-species gas samples and chemical and biomedical analytes. In chapter 7, I will discuss the phase matching consideration in Kagome HC-PCF as a possible candidate for a gas-based CARS signal measurement. Chapters 8 and 9 cover our study of the CARS signal enhancement by using a type of HCF called anti-resonance (AR) or revolver fiber.

## 2. BASIC CONCEPTS

In this chapter, we review and impart a short introduction to several basic but essential phenomena used throughout this thesis. We also offer theoretical treatments for some of these concepts.

### 2.1 Broadband coherent light generation in Raman media

First femtosecond (fs;  $10^{-15}$ s) laser pulses were generated in 1975 by using dye lasers; the pulse duration was in the range of 100's fs [29]. In 1991, using titanium-doped sapphire crystals and mode-locking techniques, pulses as short as 6.5 fs were produced [30]. Femtosecond laser pulses have a unique ability to measure short events, such as electron motion in an atom with the goal of miniaturization of electronic and photonic elements. This modeling is essential in developing quantum technologies, materials science, and electronics. Generation of subfemtosecond pulses with a spectrum centered around the visible region is even more desirable since the pulse duration will be shorter than the optical period and will allow sub-cycle field shaping. As a result, direct and precise control of electron trajectories in photoionization and high-order harmonic generation will become possible. One of the methods utilized to generate these pulses and manipulate their waveforms is through synthesizing a broadband coherent Raman generation [31]. Precise phase control over this broad coherent spectrum enables ultrashort pulse synthesis and temporal shaping. The broader the band, the shorter the resultant synthesized pulse. This broadband generation happens via what is called "molecular modulation" [11].

### 2.2 Coherent sideband generation in Raman-active crystals

Molecular modulation is a relatively recent technique that has played a critical role in the generation of ultrashort pulses (femtosecond and attosecond) in the visible range in the past few years. This technique is based on the preparation of near-maximal molecular coherence adiabatically by driving the molecular transition slightly off resonance to excite a single molecular superposition

state. In return, the created molecular vibration modulates the driving laser frequencies, and thereafter, a very broad FM-like spectrum of multi-color sidebands gets produced. These sidebands are called "coherent Raman sidebands". By exploiting the molecular modulation technique, Sokolov et al. demonstrated the generation of a near single-cycle pulse through Raman interaction in deuterium gas [32]. Concomitantly, Zhavoronkov et al. synthesized pulses as short as 4 fs by using a hollow-core waveguide filled with a pre-excited Raman-active gas [33]. Along the same direction, Suzuki et al. produced an octave-spanning Raman comb from single-frequency lasers in gaseous parahydrogen [34].

In addition to ultrashort pulse synthesis, the Raman sideband generation technique can also be used in many other ways, such as:

- using each individual generated Raman sideband as a new source of radiation in the regions that are not easily accessible by other techniques,
- controlling the refractive index in the molecular ensembles, using two Raman sidebands [35] or the full frequency comb [36, 37],
- studying the transfer of the orbital angular momentum (OAM) of light in nonlinear Raman processes.

To better understand the process of coherent broadband sideband generation, one can closely follow Hickman's method described in [38] and arrive at the same formulation described in [39] which uses another method. This will give us a  $2 \times 2$  Hamiltonian and an eigenvalue equation of:

$$i\hbar \frac{\partial}{\partial t} \begin{bmatrix} C_1 \\ C_2 \end{bmatrix} = -\frac{\hbar}{2} \begin{bmatrix} \sum_j a_j |V_j^2| & \sum_j b_j V_j V_{j-1}^* \\ \sum_j c_j V_j V_{j+1}^* & \sum_j d_j |V_j^2| - 2\Delta\omega \end{bmatrix} \begin{bmatrix} C_1 \\ C_2 \end{bmatrix}. \quad (2.1)$$

Here  $V_j$ s are the amplitudes of the time dependence interaction potential and equal to  $E_j e^{i\phi_j}$ ,  $C_j$ s are the probability amplitude of the state  $j$ .  $a_j$ ,  $b_j$ ,  $c_j$ , and  $d_j$  are related to the Raman polarizability matrix and can be found in [39].

The propagation equation for the  $q$ th Raman sideband which is separated from the  $(q+1)$ th and

(q-1) sideband by the Raman frequency, and is moving in the time frame with the speed of light  $c$  in the  $z$  direction can be described as follows [39]:

$$\frac{\partial E_q}{\partial z} = -i\hbar\eta\omega_q N(a_q\rho_{aa}E_q + d_q\rho_{bb}E_q + b_q^*\rho_{ab}E_{q-1} + b_{q+1}\rho_{ab}^*E_{q+1}), \quad (2.2)$$

where  $\eta = \sqrt{\mu_0/\epsilon_0}$  is the free space impedance,  $\omega_q$  is the frequency of the  $q$ th sideband,  $N$  is the molecular density, and  $\rho_{ij}$ s are the elements of the density matrix. This equation is driven with the assumption of negligible diffraction, however, it gives us an approximate spectral distribution over distance.

In this thesis, instead of gaseous media, we focus on the generation of coherent Raman sidebands in crystals which is more efficient; however, fewer sidebands per train may be generated due to the use of fs pulses instead of ns or ps pulses as well as reduced interaction length.

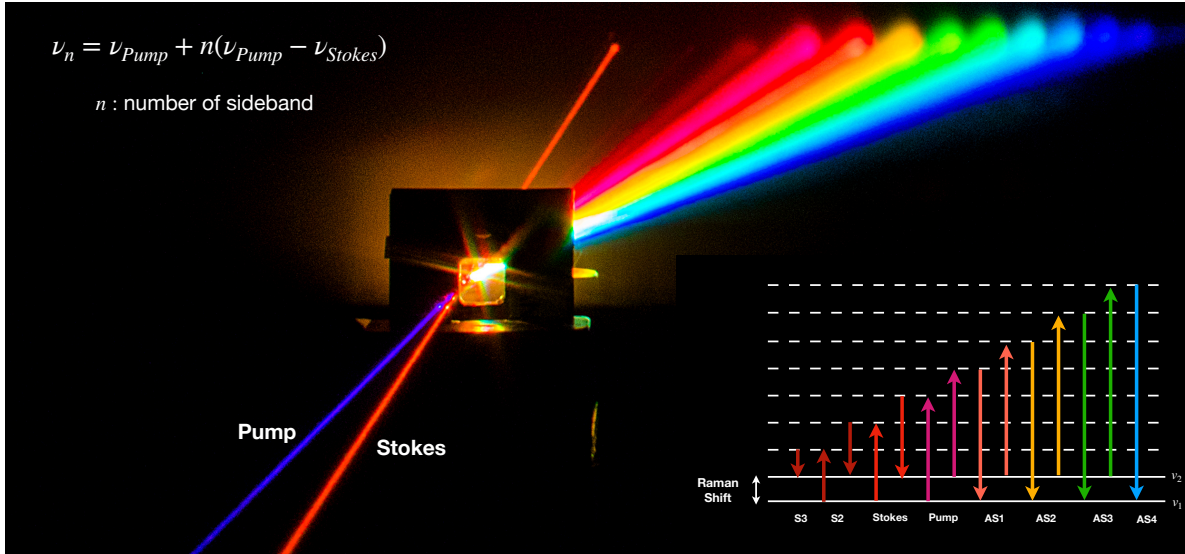


Figure 2.1: Generation of Raman sidebands in a single-crystal diamond. An 800 nm pulse out of a Ti:Sapphire laser is used as pump, and an 890 nm OPA-generated pulse is used as the Stokes beam. The anti-Stokes beams' orders are marked as  $n$  and their frequencies as  $\nu_n$  while the frequencies of the pump and Stokes beams are labeled as  $\nu_{pump}$  and  $\nu_{Stokes}$ , respectively (OPN image of the week, Jan. 2020). Inset: Energy level diagram for Raman Stokes and anti-Stokes generation.

Similar to gaseous media, collinear interaction is possible in crystals, but is not as efficient due

to the dispersion of the medium, requiring the geometry of the two driving fields to be adjusted to cross at a larger angle. This causes a reduced effective interaction length  $L_{eff}$ . Hence, the generated Raman sidebands propagate at different group velocities and exit the crystal with different angles. This Raman generation has a much broader spectrum spanning the infrared, visible, and ultraviolet spectral regions. Molecular gases used as Raman media have many advantages. For example, they have a much higher optical homogeneity. They also have higher frequency vibrational modes with small spectral broadening, which leads to much larger Raman frequency shifts and larger Raman scattering cross sections. On the other hand, one main disadvantage of using them as a Raman medium is the need for a long gas cell to provide a longer interaction length. This is due to the lower particle concentration of gaseous media compared to crystals. We can calculate the interaction length,  $L_{eff}$ , for this configuration as follows:

$$L_{eff} = 2\tau_p |\Delta V_G| = 2\tau_p \left| \left( \frac{1}{V_{G,i}} - \frac{1}{V_{G,j}} \right)^{-1} \right|, \quad (2.3)$$

where  $\tau_p$  is the input pulse duration at FWHM,  $V_{G,i}$  and  $V_{G,j}$  are the group velocities of the two interacting waves  $i$  and  $j$ ,  $\Delta V_G$  is the group velocity mismatch (GVM). Equation 2.3 is easily achieved by knowing that the group velocity  $V_G = d\omega/dk = \frac{c}{n - \lambda dn/d\lambda}$ .  $c$  is the speed of light,  $n$  is the refractive index of the propagating medium, and  $\lambda$  is the wavelength of the propagating field.

Equation 2.3 gives us a thickness of 0.5 mm for the diamond crystal in our experiment to obtain an optimum phase matching. The properties of this diamond are shown in Table 2.1.

Figure 2.1 shows the configuration that is achieved by crossing the two deriving beams (pump and Stokes) at a specific angle inside this crystal. As a result, the generated sidebands exit the diamond at different angles, and, therefore, additional experimental alignments and techniques are required to recombine these sidebands to synthesize ultrafast waveforms. Chapters 4 and 5 are dedicated to these techniques, and present promising results on the generation of near single-cycle pulses.

Table 2.1: Properties of the single crystal diamond (C) used in the experiments throughout this thesis [40].

Single-crystal Diamond's Properties	
Crystal Type	Isotropic
Crystal Density	3.5 g/cm <sup>3</sup>
Atom Density	1.77 × 10 <sup>23</sup> cm <sup>-3</sup>
Optical Transparency	0.225 μ m (far IR)
Bandgap	5.45 eV
Main Raman Mode	1332 cm <sup>-1</sup>

### 2.3 Ultrashort Pulse Measurement

As Rick Trebino, the inventor of frequency-resolved optical gating (FROG), stated: "In order to measure an event in time, you must use a shorter one. But then, to measure the shorter event, you must use an even shorter one. And so on. So, now, how do you measure the shortest event ever created [41]?" The shortest events ever observed are ultrashort laser pulses. The only tool to measure them is themselves. There are several techniques to measure ultrashort laser pulses:

- Spectral interferometry (SI)
- Spectral phase interferometry for direct electric-field reconstruction (SPIDER)
- Multiphoton intrapulse interference phase scan (MIIPS)
- Grating-eliminated no-nonsense observation of ultrafast incident laser light e-fields (GRENOUILLE)
- Frequency-resolved optical gating (FROG) .

In this thesis, we focus on the last technique which we use in our experiment to measure the ultrashort near single-cycle pulses that we synthesize by the linear combination of the coherent Raman sidebands generated in a single-crystal diamond.

### 2.3.1 Frequency-Resolved Optical Gating (FROG)

FROG is a non-linear technique for measuring the spectral phase of ultrafast laser pulses, ranging from sub-femtosecond to nanosecond, by generating a spectrogram known as FROG trace of the measured pulse. The FROG trace on its own can provide useful information about the measured pulse; however, to obtain quantitative information, an iterative 2D phase retrieval algorithm is needed. The traditional FROG uses the pulse itself to gate it. Collecting FROG traces experimentally is relatively fast and simple. The data acquisition time can be as short as 33ms using a CCD camera [42]. Figure 2.2 (a,b) shows the two different types of FROG: auto-correlated and cross-correlated. In the first one, the original pulse, known as probe, is split into two legs. One leg then is temporally delayed relative to the other one, and both are focused into a nonlinear medium in which one leg gates a portion of the other leg, and the power spectrum is recorded. This process is basically resolving the gated pulse spectrally. The collected spectrogram is called a FROG trace which can provide qualitative information about the measured pulse. However, to produce quantitative data, a 2D phase retrieval is needed. On the other hand, cross-correlation FROG involves two pulses (the gate and the unknown pulse) that are not necessarily a replica or a function of each other. A prominent algorithm that can invert all types of these spectrograms [43] is called "the method of generalized projection" (MGP) or "generalized projection algorithm" (GPA). After the introduction of the GPA, the measurement rates are no longer algorithm limited. The only factor that would limit the 2D phase retrieval is the data acquisition rate.

### 2.3.2 Generalized Projections Algorithm

In 1994 DeLong et al. implemented the GPA for the first time to retrieve the phase and intensity of an ultrashort laser pulse collected from the experimental trace in FROG by numerically minimizing the least-square FROG error with respect to  $E(t)$  [44]. Despite its complexity, the method of GP has proven to be the most reliable way to retrieve the phase and the amplitude of an unknown pulse whose its FROG traces are experimentally collected. Inherently a blind algorithm, GPA can be

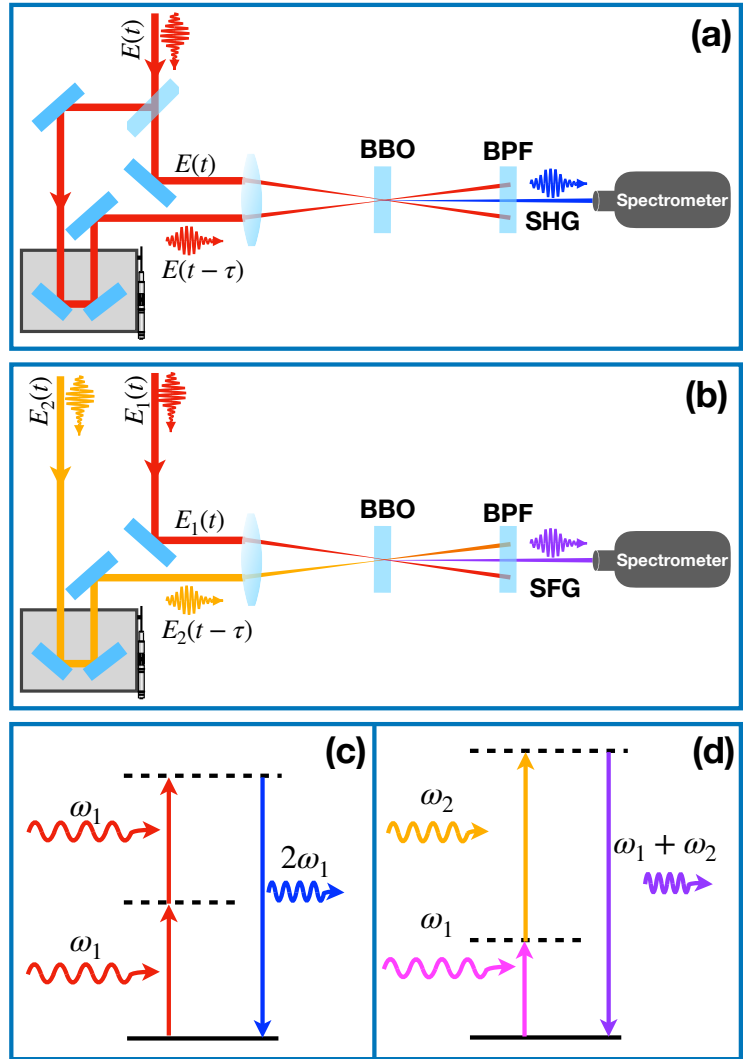


Figure 2.2: Schematic of two simple setups for (a) frequency-resolved optical-gating (FROG) and (b) cross-correlation FROG (XFROG). In (a), a strong known pulse is used to gate itself by interacting non-collinearly with a delayed copy of itself. To generate this copy, the original pulse is divided into two legs by a 50/50 non-polarizing beam splitter at the beginning of its path. One leg then is delayed temporally, and both are focused in a nonlinear crystal (beta barium borate (BBO) in this case) using a thin convex lens. The second harmonic generation (SHG) signal is then generated in the non-linear crystal and detected by a spectrometer. Usually, a bandpass filter (BPF) is used to separate the strong fundamental from the SHG signal. In (b), however, a strong known signal is used to measure a weak unknown signal. The setup resembles the FROG setup with a difference in the input beams. Moreover, the detected signal is sum frequency generation (SFG). The energy levels of these two nonlinear signal generations (i.e., SHG and SFG) are shown in (c) and (d).

adapted to the FROG inversions, where the gate is or is not a function of the measured pulse. The way that this algorithm works is by assigning two different sets of points in a space that contains all possible signal electric fields. There is one set of these complex fields ( $E(t)$ ) that satisfies the measured FROG trace  $I_{FROG}(\omega, t)$ . The algorithm starts by guessing a signal field generated from the original pulse electric field,  $E(t_i)$ . The first guess is called  $E_{sig}(t_i, \tau_j)$ .  $t$  is the pulse time and  $\tau$  is the time delay created between the two legs.  $i$  and  $j$  are different points on the grid in a 2D FROG trace. This guess can be a Gaussian or a non-Gaussian noise, depending on the most similar trace to the collected FROG spectrogram each can generate. In the next step, a “generalized projection” is made by replacing  $E_{sig}(t_i, \tau_j)$  with the square root of the magnitude of the intensity of the FROG trace,  $E'_{sig} = \frac{E_{sig}(\omega, t)}{|E_{sig}(\omega, t)|} \sqrt{I_{FROG}}$  which enables the access to the waveforms that satisfy the FROG data constraint of  $I_{FROG}(\omega, t) = |\int_{-\infty}^{+\infty} E_{sig}(t_i, \tau_j) \exp(-i\omega t) dt|^2$ . After this step is executed, the algorithm makes another iteration by projecting onto the set of fields that is assumed to consist of all the fields coming from the nonlinear interactions involved in this specific measurement which can be expressed as follows:

$$E_{sig}(t, \tau) = E(t)\Gamma[E(t - \tau)]. \quad (2.4)$$

$E(t)$  is the electric field of the probe pulse and can be written as:

$$E(t) = Re\{\sqrt{I(t)} \exp[i(\omega_0 t - \phi(t))]\}. \quad (2.5)$$

$E(t-\tau)$  is the time-delayed version of it; both  $E(t)$  and  $E(t-\tau)$  are depicted in figure 2.2 (a).  $\Gamma$  is a function so-called, the gate function which converts the pulse into the gate, and depends on the nonlinear interaction used. The inverse of the gate function;  $\Gamma^{-1}$  produces the probe from the gate. For an auto-correlated SHG FROG,  $\Gamma[E(t - \tau)] = E(t - \tau)$ . A distance function  $Z$  can be defined and minimized between the two consecutive iterations;  $k$  and  $k+1$  as:

$$Z = \sum_{i,j=1}^n |E_{sig}^k(t_i, \tau_j) - E_{sig}^{k+1}(t_i, \tau_j)|^2. \quad (2.6)$$

Now, by replacing  $E_{sig}(t_i, \tau_j)$  in equation 2.6 with what we had in equation 2.4, and finding the gradient of  $Z$  with respect to  $E_{sig}^{k+1}(t_i)$  and minimizing it we can arrive to  $E_{sig}^{k+1}(t_i)$ , and Fourier transform it into the frequency domain. We then substitute its intensity with the FROG intensity. We continue this step over and over until we reach a 2% RMS error between the measured FROG trace obtained experimentally and the reconstructed FROG trace. The process of minimization in this algorithm can be very time-consuming; therefore, it is not as straightforward to use for blind retrievals. Hence, a slightly different generalized projections algorithm called principal component generalized projections (PCGP) is used for standard FROG geometries (e. g. SHG and polarization-gated (PG)) and blind retrievals. The minimization step is skipped in this algorithm causing an increase in the iteration rate by a factor of 2 or higher. PCGP can invert FROG traces in real time [45].

## 2.4 Orbital angular momentum of light

Electromagnetic (EM) waves can carry both linear and angular momentum. The angular part can be divided to spin angular momentum (SAM), which is related to polarization, and orbital angular momentum (OAM), which is associated with the distribution of the EM field in space. It is well expected that an EM field can exchange momentum while interacting with matter. The concept of optical vortices (OVs) was first proposed by Cullet et al. in 1989 [46]. The idea came from a similar phenomenon in hydrodynamics, superconductivity, and superfluidity. They showed that laser cavities with large Fresnel numbers exhibit a similar manner which can be studied in the Maxwell-Bloch model framework. Two years later, Brambilla et al. demonstrated the formation of the phase singularity around dark points in the cavity where both the real and the imaginary parts of the electric field vanish, and the field phase changes by a multiple of  $2\pi$ , corresponding to the topological charge (TC) of that point [47]. Soon after, Allen et al. showed that laser lights exhibiting a Laguerre-Gaussian amplitude distribution carry orbital angular momentum (OAM) [48]. They also demonstrated the generation of higher-order OVs experimentally. Through the next few years, OVs and their transfer in non-linear processes have been studied by several groups

in multitudinal areas [49–53]. There are several ways to generate OVs, such as using static spiral phase plates (SPPs), computer-generated holograms (CGHs), deformable mirrors, mode conversion, spatial light modulators (SLMs), etc. OVs have a variety of crucial applications that are listed below:

- Increasing the contrast ratio of the extrasolar planets and their parent star for more effective detection as an OV coronagraph\*.
- Trapping and manipulating micron-sized objects as optical tweezers [54, 55].
- Increasing communication bandwidth by using a large number of vortical states [56].
- Quantum computing due to their infinite numbers of states in free space.
- Achieving high spatial resolution in microscopy beyond normal diffraction limits by stimulated emission depletion (STED) microscopy technique [57].
- ...

Unlike Hermite-Gaussian beams with rectangular symmetry, Laguerre-Gaussian beams (OVs) have rotational symmetry around the axis of propagation and carry a rotational OAM of  $l\hbar$  per photon. This indicates that OVs exert torque on a mirror placed in their propagation axis, making them an excellent tool for optical trapping. Figure 2.3 demonstrates the different Laguerre-Gaussian modes ( $L_{pl}$ )<sup>†</sup>. I will detail more on Laguerre-Gaussian beams and their properties in chapter 3.

## 2.5 Coherent Anti-Stokes Raman Spectroscopy

Coherent anti-Stokes Raman scattering (CARS) was first reported at the Ford Motor Company in 1965 [4]. Maker and Terhune observed a blue-shifted signal generated in benzene when tuning the two incident lasers such that their frequency difference matched the benzene Raman mode.

---

\*A coronagraph is an optical instrument used as an accessory on a telescope to block out extremely bright objects to detect nearby deem objects

<sup>†</sup>Source code is available at <https://opticspy.github.io/lightpipes/LaguerreGaussModes.html>

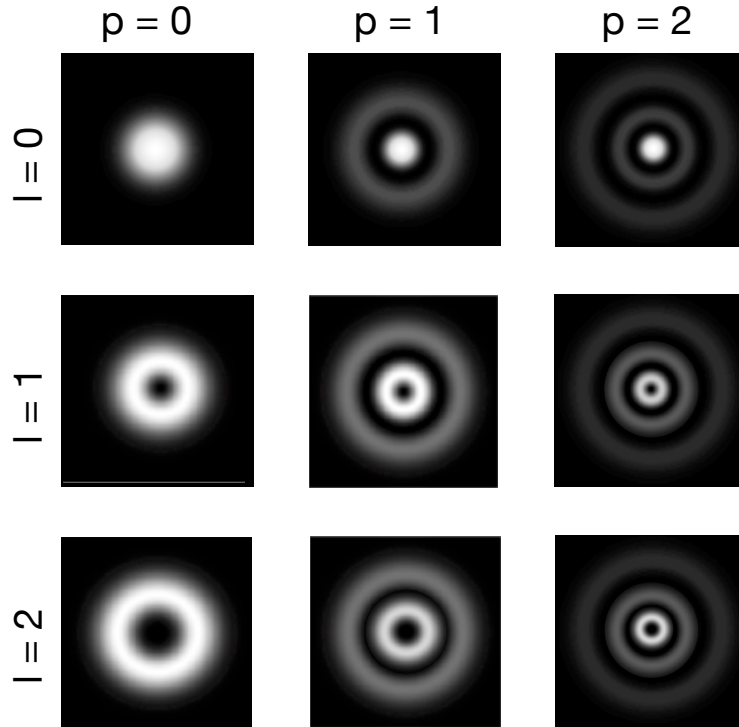


Figure 2.3: Laguerre-Gaussian modes ( $L_{pl}$ ).

CARS is a particular type of four-wave mixing (FWM) process and is a third-order nonlinear process ( $\chi^{(3)}$ ). There are two main advantages that CARS spectroscopy has over spontaneous Raman (SR) spectroscopy [58]: first, the CARS signal is up to nine orders of magnitude more robust than the SR signal. This is because of the molecular vibration due to the difference in frequency of the two laser pulses that modulate the dielectric constant, changing the polarisation, intensity, and frequency of the incident beams to produce an enormous coherent Raman signal amplitude [59]. The second advantage is that the CARS signal is blue-shifted from the pump and hence, is immune to the fluorescent background, which is especially significant for biological samples.

Figure 2.4 shows the energy diagrams for the CARS process and the non-resonant background (NRB) generation. The two laser fields are chosen such that  $\omega_{pump} - \omega_{Stokes} = \omega_{vib}$ . These two waves generate a large population density of vibrationally excited molecules. These excited

molecules act as a nonlinear medium for the generation of AS radiation at  $\omega_{CARS} = \omega_{pump} + \omega_{probe} - \omega_{Stokes}$ .

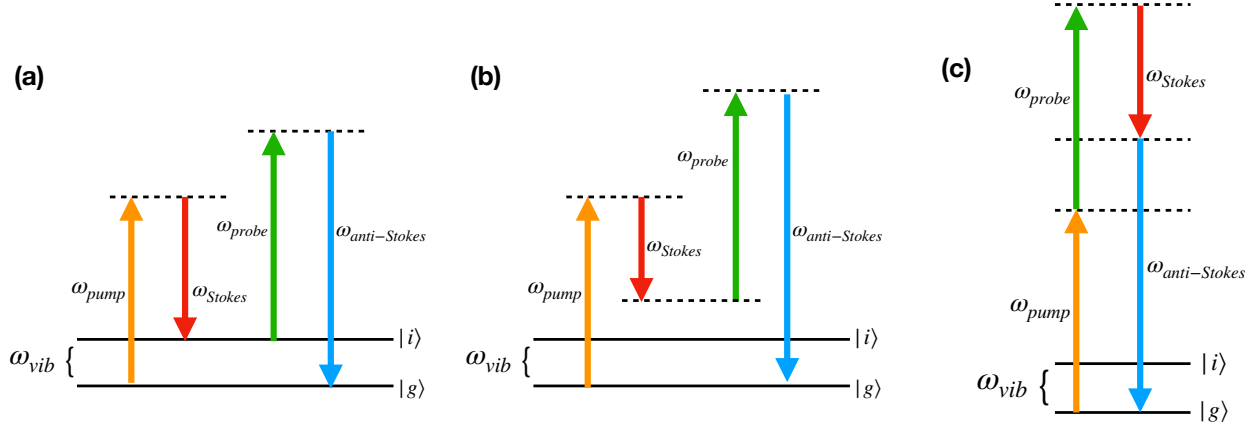


Figure 2.4: Energy diagrams for (a) coherent anti-Stokes Raman scattering (CARS) and the associated (b) non-resonant background (NRB) generation. (c) Electronic contribution enhanced by a two-photon resonance of the pump beam associated with an excited electronic state. CARS signal can deteriorate in the presence of the NRB signal, which interferes with the resonant vibrational signal, distorting the line shapes in the fingerprint area and degrading the chemical information of the analyte that is being studied.

The NRB originates from four-wave mixing caused by the electronic Kerr effect and is independent of Raman scattering as shown in Figure 2.4. The CARS signal is proportional to [60]

$$\begin{aligned}
 I_{CARS}(\omega) &\propto |\chi^{(3)}(\omega)|^2 \\
 &= |\chi_R^{(3)}(\omega) + \chi_{NR}^{(3)}(\omega)|^2 \\
 &= |\chi_R^{(3)}(\omega)|^2 + \chi_{NR}^{(3)}(\omega)^2 + 2\text{Re}(\chi_R^{(3)}(\omega))\chi_{NR}^{(3)}(\omega),
 \end{aligned} \tag{2.7}$$

where  $\chi_R^{(3)}(\omega)$  is the third-order vibrational susceptibility that contains the chemical information of the analyte and can be written as:

$$\chi_R^{(3)}(\omega) = \sum_j \frac{A_j(\omega)}{\Omega_j - \omega - i\Gamma_j}. \tag{2.8}$$

Here,  $A_j$  represents the amplitude for the  $i$ th resonance, and its value is proportional to the incident cross section and the concentration of the  $i$ th scatterer,  $\Omega_j$  is the vibrational frequency, and  $\Gamma_j$  is the linewidth. Unless the two-photon absorption presents for a certain analyte,  $\chi_{NR}^{(3)}(\omega)$  in equation 2.7 can usually be assumed as a real contribution. Hence, the third-order susceptibility for the CARS process involving four beams; pump, Stokes, probe, and anti-Stokes can be written as follows:

$$\chi^{(3)}(\omega_{as}; \omega_p, -\omega_S, \omega_{pr}) = \sum_j \frac{A_j(\omega_{as}; \omega_p, -\omega_S, \omega_{pr})}{\Omega_j + (\omega_p - \omega_S) - i\Gamma_j} + \chi_{NR}^{(3)}(\omega_{as}; \omega_p, -\omega_S, \omega_{pr}). \quad (2.9)$$

When the resonance condition;  $\Omega_j = (\omega_p - \omega_S)$  is met, we see a significant enhancement in the CARS signal. The signal intensity as a function of frequency can conveniently be written as follows [61]:

$$I_{CARS}(\omega_{as}) \propto \left| \iiint \chi^{(3)}(\omega_{as}; \omega_p, -\omega_S, \omega_{pr}) E_p(\omega_p) E_{pr}(\omega_{pr}) E_S^*(\omega_S) \times \delta(\omega_{as} - \omega_p, +\omega_S - \omega_{pr}) d\omega_p d\omega_S d\omega_{pr} \right|^2, \quad (2.10)$$

where  $E_p(\omega_p)$ ,  $E_{pr}(\omega_{pr})$ , and  $E_S(\omega_S)$  are the electric fields of the pump, probe, and Stokes beams, respectively, and  $\delta(\omega_{as} - \omega_p, +\omega_S - \omega_{pr})$  is Kronecker delta function. From equation 2.10, we can easily calculate the CARS signal level by knowing the excitation fields.

### 2.5.1 Wave-guided CARS

A prominent method for enhancing the CARS sensitivity is to embed the target molecule into a hollow-core (HC) fiber [62]. The primary enhancement comes from the elongated interaction length provided by the hollow core of the fiber. However, for the ultra-short pulses in such non-linear processes, temporal walk-off due to dispersion in the medium is unavoidable[63]. Hence, the dispersion inside the fiber should be manipulated somehow to fulfill the phase-matching condition [62, 64].

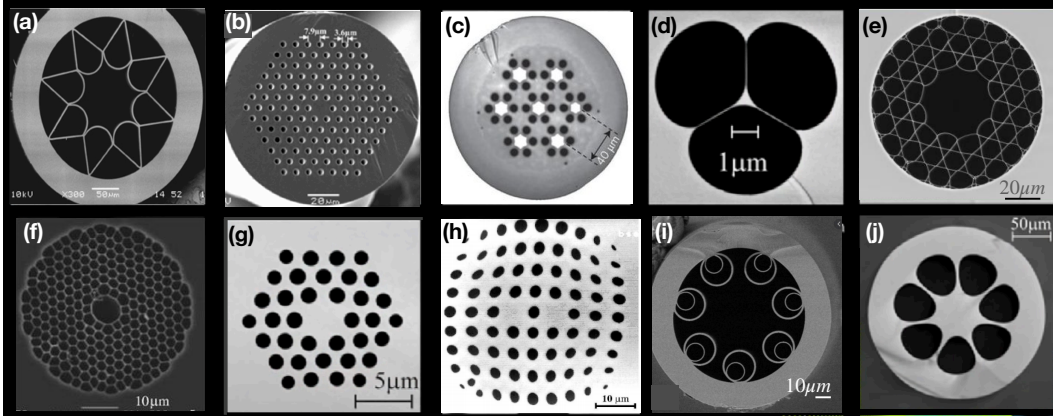


Figure 2.5: Several types of micro-structured photonic crystal fibers. (a) hollow-core fiber with negative curvature of the core wall [65], (b) solid core PCF [66], (c) multicore optical fiber [67], (d) suspended core photonic crystal fibers (SC-PCFs) with triangular-like microcores [68], (e) 7-cell Kagome fiber [69], (f) PBG fiber, SEM image is commercially available from NKT Photonics (Denmark), (g) hexagonal pattern and solid-core PCF, SEM image is commercially available from Cybel Photonics (Bethlehem, PA), (h) a double core PCF fiber with a square lattice [70], (i) AR-HCPCF [71], and (j) six-hole suspended-core fiber (SH-SCF) [72].

Structured fibers were first introduced to guide the light in materials with a low refractive index, such as gases. More importantly, they had confinement characteristics not possible in conventional optical fibers. Regular optical fibers have a solid core of a dielectric material, such as different kinds of glasses with high refractive indices, surrounded by a lower refractive index material called cladding. Hence, the light is trapped in the glass core and can travel for hundreds of kilometers without attenuation. But what if we want to transmit the light in a gaseous material like air or another type of material that does not have a compatible material to be used for its cladding?

One of the first generations of structured fibers, also known as hollow-core photonic-crystal fiber (HCPCF), has a hollow core and a holey cladding around it. The cladding is designed so that every time the light comes in the surface between the material (typically silica) and the air, some of it gets reflected and some transmitted. In a similar fashion, at the next interface, some get reflected and some transmitted, and so on. Using the right pattern, we can make all the transmitted waves destructively cancel each other out, so no light gets transmitted, and hence, the structure is just a mirror that does not transmit light. If we wrap this design around a hole, the light has no

choice but to travel in the air inside the core because it is surrounded by a perfect mirror, which is precisely the mechanism of the photonic bandgap (PBG) fibers. These structured fibers can guide the light in the air, which would never have been possible before due to the low refractive index of the air. Another class of fibers has a different waveguiding mechanism, so-called inhibited coupling (IC). In these fibers, the cladding is designed in such a way that although unlike PBG fibers, the cladding modes are allowed, the coupling between the core modes and the cladding modes is strongly inhibited due to the exquisite control of the nanometric design features of the cladding. Kagomé HCPCF is an example that exhibits IC guidance.

Here, we study the coherent anti-Stokes Raman scattering (CARS) in two different types of HCPCFs. The reason for using these fibers is, first, to elongate the interaction length for the four-wave-mixing (FWM) process and, second, to adjust factors such as pressure and temperature to improve the phase-matching for the FWM. The enhancement scales as  $\lambda^2 l^2 / a^4$ , where  $\lambda$  is the radiation wavelength,  $l$  is the length of the hollow-core fiber, and  $a$  is the radius of its core. To improve this factor, one might make the fiber length very large, but the interaction length  $l$  is limited by the losses in the core [73]. These losses are caused by absorption, scattering, and bending losses and can be calculated as:

$$\alpha = \frac{10}{l} \log \frac{P_i}{P_o}, \quad (2.11)$$

with  $P_i$  and  $P_o$  being the powers of the input and output light at the two ends of the fiber, respectively. These three losses are associated with the amount of light leakage into the cladding: absorption of the cladding material, radiative leakage due to the finite crystal size, and scattering from disorder. All these losses can diminish by the increase in the core radius  $a$ . It is shown that they typically decrease asymptotically as  $1/a^3$  [74].

## 2.5.2 Photonic Fiber Modes

For photonic crystal fibers which the material is generally dielectric, the electric displacement,  $\mathbf{D}$ , and the magnetic fields,  $\mathbf{B}$ , can be described as follows:

$$\mathbf{D} = \epsilon_0 \mathbf{E} + \mathbf{P}, \quad (2.12)$$

$$\mathbf{B} = \mu_0 \mathbf{H}, \quad (2.13)$$

where  $\epsilon_0$  is the permittivity of vacuum (also called the permittivity of free space),  $\mu_0$  is the vacuum permeability, and  $\mathbf{P}$  is the density of the electric dipole moments in the material known as electric polarization. In other words,  $\mathbf{P}$  is the response of a medium to an applied electric field  $\mathbf{E}$ .

Substituting these equations into the main Maxwell's equations, we can obtain the general wave equation as follows:

$$\nabla^2 \mathbf{E} - \frac{1}{c^2} \frac{\partial^2}{\partial t^2} \mathbf{E} = \mu_0 \frac{\partial^2}{\partial t^2} (\mathbf{P}_L + \mathbf{P}_{NL}), \quad (2.14)$$

where  $P_L$  and  $P_{NL}$  are the linear and nonlinear polarization. This means that  $P_L$  and  $P_{NL}$  have linear and nonlinear dependence on the electric field  $\mathbf{E}$ , respectively. While considering mode formation in photonic fibers, the nonlinear polarization can be neglected in equation 2.14 since its value is much smaller than the value of the linear polarization  $\mathbf{P}_L$ , which is given as,

$$\mathbf{P}_L(\mathbf{r}, t) = \epsilon_0 \int_{-\infty}^t \chi^{(1)}(t - t') \mathbf{E}(\mathbf{r}, t') dt'. \quad (2.15)$$

Here,  $\chi^{(1)}$  is the first-order susceptibility. Hence, equation 2.14 in the frequency domain can be simplified as:

$$\nabla^2 \hat{\mathbf{E}}(\omega) + \frac{\omega^2}{c^2} (1 + \hat{\chi}^{(1)}(\omega)) \hat{\mathbf{E}}(\omega), \quad (2.16)$$

where  $\hat{\mathbf{E}}$  and  $\hat{\chi}^{(1)}$  represent the Fourier transform of the propagating field and the electric susceptibility, respectively. In general, for the optical frequencies  $\text{Im}(\chi^{(1)}) \ll \text{Re}(\chi^{(1)})$ . And since  $\hat{\chi}^{(1)} \ll 1$ , with a good approximation  $(1 + \hat{\chi}^{(1)}(\omega)) \approx 1 + 1/2 \text{Re}(\hat{\chi}^{(1)}) = n$ , with  $n$  being the refractive index of the propagation medium which we assume does not change based on the spatial coordinate, meaning that the propagation medium is isotropic. Therefore, we can rewrite equation 2.16 as follows:

$$\nabla^2 \hat{\mathbf{E}}(\omega) + n^2(\omega) k_0^2 \hat{\mathbf{E}}(\omega) = 0, \quad (2.17)$$

where  $k_0^2 = \frac{\omega^2}{c^2}$  represents the wave number in the free space. To solve equation 2.17, let us use the separation method and assume a solution in the Cartesian coordinates as:

$$\hat{\mathbf{E}}(\mathbf{x}, \mathbf{y}, \mathbf{z}, \omega) + n^2(\omega) = E(\omega) \mathbf{f}(\mathbf{x}, \mathbf{y}) \exp(i\beta z). \quad (2.18)$$

$E(\omega)$  is the modal electric field's amplitude,  $\mathbf{f}(\mathbf{x}, \mathbf{y})$  is the transverse component of the mode's complex distribution, and  $\beta$  is the propagation constant which is the amount of change in the phase of an electromagnetic field as it propagates in a medium. By substituting this solution into the equation 2.17 and taking the final results to the cylindrical coordinate ( $E(\rho, \phi, z) = F(\rho)\Phi(\phi)Z(z)$ ) for the convenience due to the cylindrical shape of the PCFs, we will obtain the three following equations:

$$\frac{\partial^2 Z}{\partial z^2} + \beta^2 Z = 0, \quad (2.19)$$

$$\frac{\partial^2 \Phi}{\partial \phi^2} + m^2 \Phi = 0, \quad (2.20)$$

and,

$$\frac{\partial^2 F}{\partial \rho^2} + \frac{1}{\rho} \frac{\partial F}{\partial \rho} + (n^2 k_0^2 - \beta^2 - \frac{m^2}{\rho^2}) F = 0, \quad (2.21)$$

with  $m$  being an integer related to the azimuthal period of the fields in cylindrically symmetric waveguides with a radius of  $a$ .  $\rho$ ,  $\phi$ , and  $z$  are the axial distance or radial distance, the azimuthal angle (or azimuth), and the axial coordinate in cylindrical coordinate, respectively. Equations 2.19 and 2.20 simply lead to  $Z(z) = \exp(i\beta z)$  and  $\Phi(\phi) = \exp(im\phi)$ . The last equation (equ.2.21), however, will lead to  $F(\rho)$ s which satisfies the Bessel equation. The solutions for the last equation are an  $m$ th order Bessel functions ( $J_m$ ) and  $m$ th order modified Bessel functions ( $K_m$ ):

$$F_\rho = \begin{cases} J_m(p\rho) & , \text{ for } \rho \leq a \\ K_m(q\rho) & , \text{ for } \rho > a \end{cases} \quad (2.22)$$

with  $p = \sqrt{n_{co}^2 k_0^2 - \beta^2}$  and  $q = \sqrt{\beta^2 - n_{cl}^2 k_0^2}$ .  $n_{co}$  and  $n_{cl}$  are the refractive indices of the fiber core and fiber cladding, respectively. We can have a similar argument for the magnetic field, therefore, writing the electric field ( $E$ ) and the magnetic field ( $H$ ) components as follow:

$$E_z = \begin{cases} A J_m(p\rho) e^{(im\phi)} e^{(i\beta z)} & , \text{ for } \rho \leq a \\ B K_m(q\rho) e^{(im\phi)} e^{(i\beta z)} & , \text{ for } \rho > a \end{cases} \quad (2.23)$$

and,

$$E_\rho = \frac{i}{p^2} \left( \beta \frac{\partial E_z}{\partial \rho} + \mu_0 \frac{\omega}{\rho} \frac{\partial H_z}{\partial \phi} \right) \quad , \quad E_\phi = \frac{i}{p^2} \left( \frac{\beta}{\rho} \frac{\partial E_z}{\partial \phi} - \mu_0 \omega \frac{\partial H_z}{\partial \rho} \right) \quad (2.24)$$

Similarly,

$$H_z = \begin{cases} C J_m(p\rho) e^{(im\phi)} e^{(i\beta z)} & , \text{ for } \rho \leq a \\ D K_m(q\rho) e^{(im\phi)} e^{(i\beta z)} & , \text{ for } \rho > a \end{cases} \quad (2.25)$$

and,

$$H_\rho = \frac{i}{p^2} \left( \beta \frac{\partial H_z}{\partial \rho} - \epsilon_0 n^2 \frac{\omega}{\rho} \frac{\partial E_z}{\partial \phi} \right) \quad , \quad H_\phi = \frac{i}{p^2} \left( \frac{\beta}{\rho} \frac{\partial H_z}{\partial \phi} + \epsilon_0 n^2 \omega \frac{\partial E_z}{\partial \rho} \right), \quad (2.26)$$

where  $A, B, C$ , and  $D$  are four constants to be determined, and  $\epsilon_0$  and  $\mu_0$  are the vacuum permittivity and the vacuum permeability, respectively. After applying the boundary condition at the interface of the core and the cladding which means the continuity of the electric and the magnetic fields, the four equations for the  $H_z$  and  $E_z$  can be reduced to the following eigenvalue equation:

$$\left[ \frac{J'_m(pa)}{pJ_m(pa)} + \frac{K'_m(qa)}{aK_m(qa)} \right] \left[ \frac{J'_m(pa)}{pJ_m(pa)} + \left(\frac{n_{cl}}{n_{co}}\right)^2 \frac{K'_m(qa)}{aK_m(qa)} \right] = \left[ \frac{n_{co}^2 - n_{cl}^2}{n_{co}} \times \frac{m\beta k_0}{ap^2q^2} \right]^2. \quad (2.27)$$

This is a decent approximation for optical fibers with a relatively simple structure such as capillary or capillary-like fibers, however, for more complex cladding lattice, it is preferable to use a finite-element modeling (FEM) method on a scanning electron microscope (SEM) image of the fiber's cross-section to obtain the guided modes.

### 2.5.3 Anti-resonant Guidance

In this section, we elaborate on the guiding mechanism of an anti-resonant hollow-core fiber (AR-HCF), also known as Revolver fiber, which is used in the experiment described in chapters 8 and 9. AR-HCF has a similar but much simpler design than the well-known Kagomé fiber which is described in chapter 7. This fiber is also known as single-ring fiber because the cladding consists of a single ring instead of a complex photonic crystal lattice. AR-HCF has an excellent capability of guiding light through its air core with low loss over a broad spectral range making it a great candidate for laser-based spectroscopy of gaseous substances. The anti-resonance waveguiding mechanism can be explained by the antiresonant reflecting optical waveguiding (ARROW) model, treating the core boundary area like a Fabry–Perot resonant cavity since it consists of low refractive index (air) and high refractive index (glass) layers as shown in figure 2.6 (inset).

This cavity transmits only the frequencies that are not in resonance with the capillary walls of the core, therefore, they reflect back into the fiber core and propagate through it without a

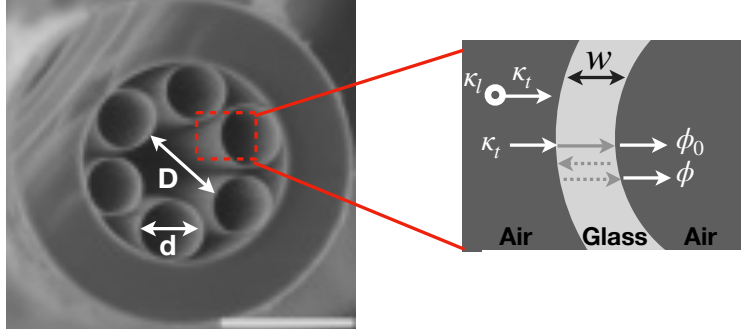


Figure 2.6: SEM image of an AR-HCF with a core diameter  $D$ , and capillary ring diameter  $d$ . Inset: the anti-resonance concept at the air-glass interference.  $w$  is the capillary wall thickness,  $k_t$  and  $k_l$  are the transverse and the longitudinal components of the wave vector.  $\Phi_0$  is the initial phase of the leaking light whose part of it transmits with no acquired extra phase.  $\Phi_1$  is the phase of the part of the leaking light which gets reflected twice at the air-glass interfaces.

significant loss. The resonant frequencies, however, easily leak from the core to the cladding and could not be transferred through the fiber. Figure 2.6 shows the SEM image of the AR-HCF. The inset illustrates the light leakage through the glass walls which are perpendicular to the core where  $k_l$  and  $k_t$  are the longitudinal and the transverse components of the wave vector, respectively. As shown in this figure, some part of the incident light at the wall acquires an extra phase by reflecting twice at the glass-air interface. The phase difference between the original light which transmits through the glass with a phase of  $\phi_0$  and the other part that transmits with the phase of  $\Phi_1$  is:

$$\Delta\Phi = \begin{cases} 2k_t w = 2\pi m & , \text{ for constructive interference} \\ 2k_t w = (2\pi + 1)m & , \text{ for destructive interference} \end{cases} \quad (2.28)$$

where  $w$  is the wall thickness of the capillaries as shown in figure 2.6 (inset), and  $m = 0, 1, 2, \dots$ . These two light waves will interfere constructively or destructively depending on the phase difference  $\Delta\Phi$ . The first case, i.e. constructive interference happens at the resonance frequencies and is responsible for high losses. Moreover, since the transverse component of the vector is:

$$k_t = \frac{2\pi}{\lambda} \sqrt{n_{cl}^2 - n_{co}^2} \quad (2.29)$$

The anti-resonant and resonant wavelengths can be calculated by substituting  $k_t$  in the equation 2.28 which gives [75]:

$$\lambda_{AR} = \frac{4w}{(1 + 2m)} \sqrt{n_{cl}^2 - n_{co}^2}, \quad (2.30)$$

and,

$$\lambda_{res} = \frac{2w}{(m)} \sqrt{n_{cl}^2 - n_{co}^2}, \quad (2.31)$$

In the vicinity of each  $m$  value, core modes are coupled into light in the cladding walls. Thus, high- and low-loss bands in a transmission spectrum are determined by the air-glass refractive index contrast and the thickness of the high-index layer of the cladding structure according to equations 2.30 and 2.31, however, Carter et al. showed that both the core diameter and the diameter of the capillary rings play an essential role in the bending properties and single-mode guidance of ARHCF. They showed that selecting these two dimensions carefully to reach the perfect ratio of the core to capillary diameter to be around 0.65, enables single-mode transmission within the fiber low-loss window due to the increased loss ratio between the fundamental mode and the higher-order modes [76].

## 2.6 Summary

In this chapter, we detailed several basic concepts that are used throughout this thesis. We also briefly reviewed some of the theoretical considerations. These concepts include:

- broadband coherent Raman generation,
- OAM of light and its transfer in Raman processes,
- methods of ultrashort pulse measurements, such as FROG,
- anti-resonant wave-guidance mechanism,
- CARS spectroscopy and in particular CARS in HC-PCFs,
- ... .

### 3. TOPOLOGICAL CHARGE TRANSFER IN COHERENT RAMAN PROCESSES IN PbWO<sub>4</sub> CRYSTAL

#### 3.1 Introduction

Structured light has an astonishingly wide range of prospective applications for the non-contact optical manipulation of matter. Focused laser trapping [77], optical tweezers [54, 55], biological cell handling [78], nano-fabrication [79], photonics [80, 81], data transmission in optical fibers [82], and high-order quantum entanglement [83] are only a few of the many applications that structured light, in particular, optical vortices (OVs) have to offer. Laser vortex beams or OVs can also be utilized for stimulated emission depletion (STED) microscopy and nanoscopy to achieve super-resolution [57]. Considering the ubiquitousness of the OVs in multitudinal science, studying these light waves in the physical systems is extremely important. This chapter focuses on the interaction of optical vortices, and femtosecond optical vortices in particular with nonlinear Raman-active crystals. An OV beam with a phase singularity at the center exhibits a hollow intensity distribution (a ring of light) with a helical phase-front. Depending on how many twists the light makes in one wavelength these OVs are given an integer number called the topological charge (TC) which sometimes can be the same as the integer amount of orbital angular momentum (OAM) that the vortex carries. The sign of the TC depends on the direction of the twists. The OAM should not be confused with the spin angular momentum (SAM); the OAM of a light beam is related to the phase distribution while the SAM determines the polarization. A vortex beam is essentially a paraxial light that possesses Hilbert factor  $\exp(il\theta)$  carrying OAM of  $l\hbar$  for each photon.  $l$  represents the TC and  $\theta$  is the azimuthal angle in cylindrical coordinates. The TC of a singularity for a phase distribution  $\phi$  is defined as:

$$TC = \frac{1}{2\pi} \oint_C \nabla_{\mathbf{r}} \phi(\mathbf{r}) \cdot d\mathbf{r}, \quad (3.1)$$

where  $C$  is a closed loop around the singularity [84]. For OVs that are radially symmetric (Laguerre-Gaussian and Bessel-Gaussian beams [85]), TC is defined by OAM normalized to the

beam's power and equals  $l$ . OV's with different orders can be generated from a Gaussian beam through a spatial modulation using different experimental methods that will be discussed later in this chapter.

In this thesis, we are exploring the possibility of adding another aspect to the light-field shaping by adjusting the transverse input beam profiles in Raman interaction, and hence, generating coherent multi-color Raman sidebands of different orders of OV's. Generating these OV's and exploring the transfer of their TCs throughout the non-linear Raman process is the main interest of this chapter. In general, the phase of the field for a Laguerre–Gaussian beam traveling along the  $z$ -axis in cylindrical coordinate can be expressed as [86]:

$$\Phi(\rho, \theta, z) = kz + \frac{k\rho^2}{2R(z)} + l\theta - \psi(z), \quad (3.2)$$

where

$$R(z) = \sqrt{z(1 + \frac{z_R^2}{z^2})}, \quad (3.3)$$

and

$$\psi(z) = (2p + |l| + 1)\tan^{-1}(z/z_R), \quad (3.4)$$

where  $k$  is the wave number,  $z_R = \frac{k\omega_0^2}{2}$  is the Raleigh range,  $R$  is the radius of the curvature,  $\theta$  is the angular coordinate,  $p$  is the radial index which for an OV equals to zero,  $l$  ( $= TC$ ) is the angular index, and  $\psi(z)$  is the Gouy phase [87]. The phase of the beam at  $z = 0$  becomes  $l\theta$ , which contains an optical singularity. Hence, we can describe the electric field of an OV in cylindrical coordinates and as a function of time as follows:

$$E(\rho, \theta, z, t) = E_0 \frac{\omega_0 \rho^{|l|}}{\omega^{|l|+1}} \exp(\frac{-\rho^2}{\omega^2}) \exp[i(\Phi(z) - \Omega t)], \quad (3.5)$$

where  $E_0$  is the amplitude of the electric field,  $\Omega$  is the frequency of the field,  $\omega_0$  is the beam waist, and  $\omega = \omega_0 R(z)$  is the transversal beam radius.

### 3.2 TC Transfer in Raman Processes

The goal of this section is to explore the process of transferring TC from input femtosecond (fs) beams into Raman-generated vortex sidebands. The equation that governs TC transfer is derivable from either OAM conservation for created and annihilated photons in the Raman process or from considerations of phase-matching conditions between the input and output beams involved in the Raman interaction [83, 88, 89]. TC or  $l$  can be driven for each sideband as follows:

$$l_n = (n + 1)l_{pump} - nl_{Stokes}, \quad (3.6)$$

where  $n$  is the order of the anti-Stokes (AS) sidebands meaning that  $n = 1, 2, 3, \dots$  correspond to AS1, AS2, AS3, ... and  $n = -1, -2, -3, \dots$  correspond to S1, S2, S3, ... (Stokes sidebands). When  $l_{Pump} = l_{Stokes} = l$ , the TC for all the orders stays the same:  $l_n = l$  for  $n = 0, 1, 2, \dots$ .

Equation 3.6 in the phase-matching language can be equally written as:

$$\phi_n = (n + 1)\phi_{pump} - n\phi_{Stokes}, \quad (3.7)$$

where  $\phi_n$  is the relative phase of the  $n$ th interacting field, in the transverse plane [90]. This equation indicates that, for example, the phase of the first anti-Stokes sideband (AS1) is equal to twice the phase of the pump beam minus the phase of the Stokes beam;  $\Phi_{AS1} = 2\Phi_{pump} - \Phi_{Stokes}$ .

### 3.3 Experimental Setup

The schematic of the experimental setup for generating the vortex coherent Raman sidebands is shown in figure 3.2. In this configuration, we use a reference beam at 800 nm, 1 KHz repetition rate (RR), and 1 W average power out of a Ti:Sapphire ultrafast laser system and divide it into two separate legs (named pump and Stokes in coherent anti-Stokes Raman spectroscopy (CARS) terminology) by using a 50/50 non-polarizing beam splitter. The power of each beam is then adjusted by two separate neutral density (ND) filters to avoid parasitic effects such as self-phase modulation

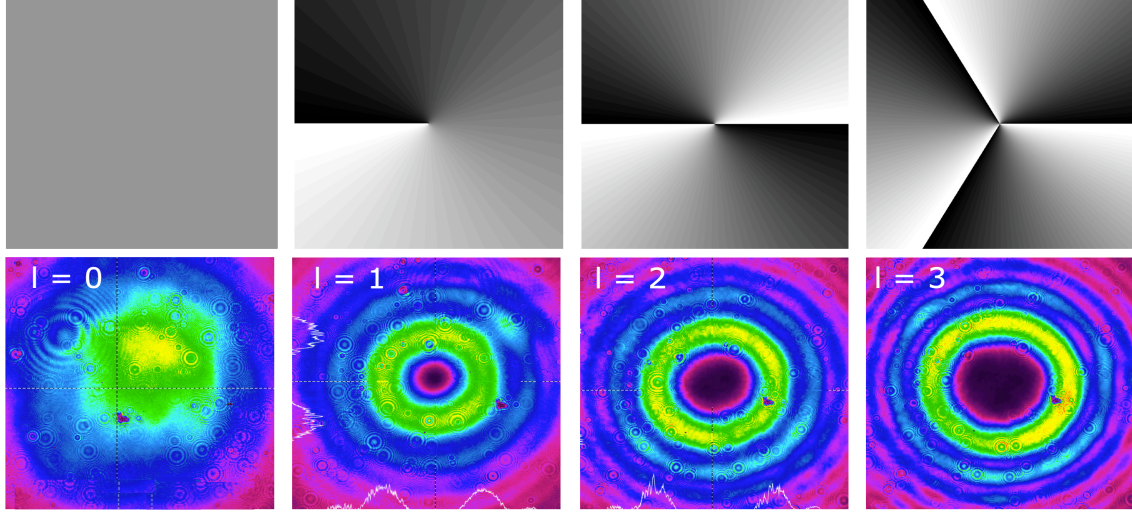


Figure 3.1: Four phase masks generated by using computer holography technique (top row) and corresponding beam profiles (bottom row). From left to right, the masks and beam profiles are for the Gaussian pump beam ( $l = 0$ ), AS1 ( $l = 1$ ), AS2 ( $l = 2$ ), and AS3 ( $l = 3$ ) that are exiting the  $\text{PbWO}_4$  crystal in our vortex Raman generation setup. Each vortex is readjusted in size to match the size of the Gaussian beam with  $l = 0$  (adapted from [91]).

(SPM), higher harmonic generation (HHG), and surface-induced scattering in the crystal, resulting in higher quality sidebands.

The Ti:Sapphire laser system is fully described in chapter 2. The amplifier (Coherent, Legend) has the ability to chirp the reference pulse from 35 fs up to 2 ps pulses. Chirping both pulses provides a broader band for the interaction and the possibility of overlapping in the proper range needed to excite the  $\text{PbWO}_4$  crystal's different Raman modes, which are driven by the frequency difference  $\Delta\omega = b\tau$ , where  $b$  is the beams' chirp rate and  $\tau$  is their relative time delay. Chirping the original reference pulse is enabled by varying the grating distance inside the compressor unit of the amplifier. Table 3.1 shows the corresponding chirp rate for each Raman mode of the  $\text{PbWO}_4$  Crystal. To excite the  $\text{PbWO}_4$  crystal's  $325 \text{ cm}^{-1}$  Raman mode, We positively chirp the reference pulse to 200 fs. A second harmonic frequency-resolved optical gating (SH-FROG) setup is used to retrieve and verify the pulse chirp precisely [92]. Furthermore, we confirm the chirp's sign by placing an SH-FROG setup before and after a piece of glass in the beam path. Table 3.1 shows the

corresponding pulse power, phase matching angle in the  $\text{PbWO}_4$  crystal, and the chirp rate out of the amplifier for the different Raman Modes of the crystal. After both beams (we label them as pump and Stokes) get separated on the polarizing beam splitter, we shape one or both of them into optical vortices.

Table 3.1: TC values of output sidebands and the number and the direction of the bright spots in tilted lens technique for different  $l_{Stokes}$ .

Raman Mode of $\text{PbWO}_4$	Pump Power	Phase-Matching Angle	Chirp Rate
$191 \text{ cm}^{-1}$	7.5 mW	$1^\circ$	$2100 \text{ cm}^{-1}/\text{ps}$
$325 \text{ cm}^{-1}$	2.5 mW	$2.5^\circ$	$2100 \text{ cm}^{-1}/\text{ps}$
$903 \text{ cm}^{-1}$	10 mW	$4^\circ$	$620 \text{ cm}^{-1}/\text{ps}$

Table 3.2: Properties of the specific  $\text{PbWO}_4$  crystal used in the experiment [93].

$\text{PbWO}_4$ Crystal's Properties	
Crystal Type	Negative Uniaxial ( $n_o > n_e$ )
Optical Transparency	$0.33 - 5.5 \mu \text{ m}$
Bandgap	4.5 eV
Main Raman Modes	191, 325, and $903 \text{ cm}^{-1}$

### 3.3.1 Optical Vortex Production

There are several ways to produce OV's in the laboratory. The two well-known methods are using spiral phase plates (SPP) [94] and computer-controlled spatial light modulators (SLM) [95]. In our experiment, we use an LCOS-SLM (liquid crystal on silicon-based spatial light modulator-

Hamamatsu 10468-02) which is a reflective spatial modulator that modulates optical phases off a liquid crystal. OVs can be generated with a spiral phase distribution through computer holography. Figure 3.1 shows four computer phase maps for the SLM-generated OVs and the corresponding beam profiles that we recorded for each map after the SLM using a beam profiler (Spiricon SP620U). The darkness of each pixel on these phase maps varies based on the phase that needs to be added to a Gaussian beam to generate different orders of OVs. For example, the added phase to a Gaussian to generate a first-order vortex beam is  $\Phi = \tan(x/y)$  where  $x$  and  $y$  are the two perpendicular spatial directions in the plane of the beam. If the phase angle continually increases clockwise along a closed loop from 0 to  $2\pi l$  and returns to the origin, the angle zero is exactly equal to  $2\pi l$ , forming a continuous phase distribution along the closed loop. This is analogous to the seemingly impossible scenario of the Penrose Stairs: while the stairs are ascending clockwise, they have a connection to their origin after a round trip.

In our study, we shape pump and Stokes beams into OVs with various integer values of TC and cross them in a 1 mm thick  $\text{PbWO}_4$  crystal to generate multiple Stokes and anti-Stokes sidebands (depending on the type of transition between energy levels in molecules/atoms we call these sidebands Stokes or anti-Stokes, as shown in figure 2.1). The properties of the  $\text{PbWO}_4$  crystal used for this section are shown in table 3.2. Two separate spherical bi-convex lenses with focal lengths of +50 cm focus pump and Stokes at an angle of  $3.16^\circ$  into the crystal. However, the crystal is placed at a distance slightly before the focus to avoid the parasitic effects as well as burning the crystal. This distance is set by trial and error until we achieve the highest power and quality for the sidebands. For the case of one modulated beam (i.e., only Stokes is vortex), the beam diameter for both pump and Stokes is  $\sim 1$  mm on the  $\text{PbWO}_4$ . However, when we modulate both beams for the second part of the experiment, we reduce the size of the beams by 25% so that both beams fit on the SLM. This reduction is done using a telescope before the polarizing beam splitter. To prevent spherical aberration, we build the telescope using thin negative meniscus and plano-convex lenses.

After the vortex sidebands are generated, we measure their TCs using a tilted bi-convex lens technique [96]. Finally, for each sideband, we can verify that the value and the sign of the TC

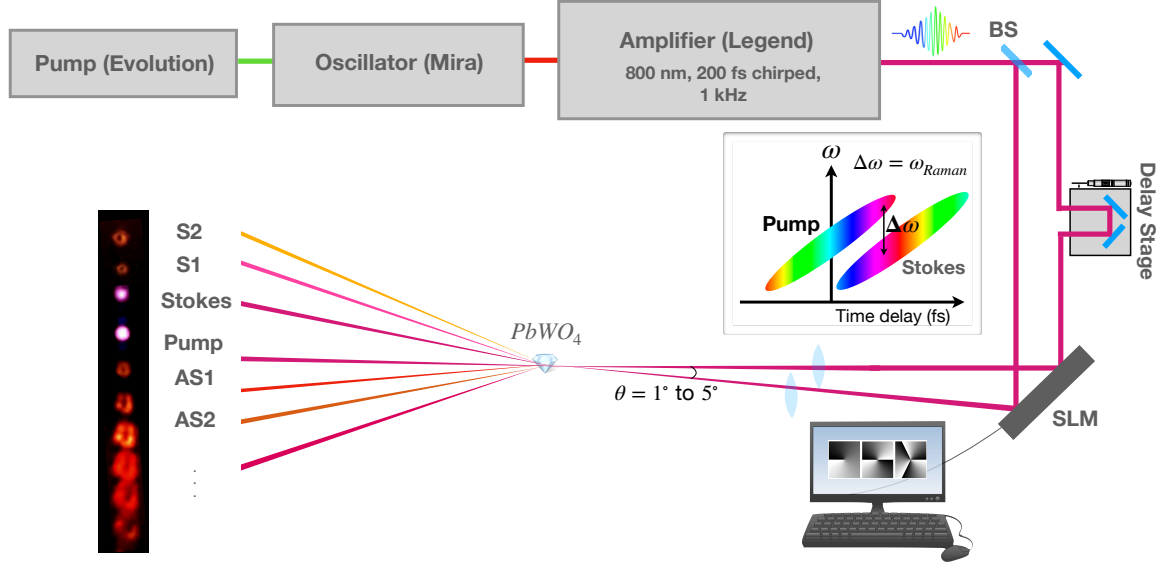


Figure 3.2: Schematic of the experimental setup which shows the generation of the vortex Raman sidebands in  $\text{PbWO}_4$  crystal. BS stands for a 50/50 beam splitter, SLM stands for spatial light modulator, S1 and S2 stand for Stokes 1 and Stokes 2, and AS1 and AS2 stand for anti-Stokes 1 and anti-Stokes 2. One leg of the reference beam out of the amplifier is split into two separate legs by a 50/50 BS. Hence, at the crystal, one input beam is a time-delayed copy of the other. This delay is controlled by using a manual delay stage in the path of one of the legs. The OVs and their orders are shown and labeled at the end of the setup after the  $\text{PbWO}_4$  crystal. The angle between the two input beams is between 1 to 5 degrees depending on the different Raman modes of the crystal that are excited each time. Anything between this range results in the appearance of the sidebands; however, the distance between the sidebands, color, and clarity of the sidebands changes at every different angle. This is due to the different phase-matching conditions between the beams at each angle. The angle of the incident and reflection on the SLM are exaggerated for clarity. Inset: the schematic of the two input chirped pulses and the time delay between them. The time delay (horizontal distance between the two chirped pulses) is controllable by adjusting the delay stage.

obey a simple relationship with the TC of the input pump and Stokes beams, resulting from the conservation of angular momentum for created and annihilated photons, or in other words, from phase-matching conditions for the interacting beams [83, 89]. Moreover, we observe that the size of each beam increases by the order of the sideband as  $r \propto |l|^2$ , meaning that the vortex with a larger TC has a larger radius. There are several methods to measure the TC of the resultant sidebands. One popular technique is to interfere the sideband with a Gaussian beam and analyze

the interference pattern [97]. A much simpler method which is called the tilted bi-Convex lens technique, can be applied to achieve the same result. The tilted bi-Convex lens technique was first proposed by Vaity et al. [96]. We use this technique to measure the value and the sign of our generated vortex sidebands. I will discuss this method in detail in the next section.

### 3.3.2 Tilted Bi-Convex Lens Technique

In this part of the experiment, we measure the sign and the magnitude of the TC for each vortex sideband only by tilting a spherical bi-convex lens in front of it and observing the change in the intensity distribution of the hot spots created after the lens [96]. The focal length of the lens is arbitrary, and we were able to obtain the same result using several spherical lenses with various focal lengths.

Figure 3.3 shows the output sidebands' beam profiles for three different values for  $l_{Stokes}$ . This figure also shows the resultant beam profiles for the hot spots appearing after the tilted lens for each case. The number of hot spots after the convex lens corresponds to the TC+1 of each sideband. For example: if there are four bright spots after the lens, the integer value for TC of the vortex sideband passing through the tilted lens is 3. The direction of the tilt of the spots corresponds to the sign of the TC.

Table 3.3 summarizes our predicted and measured TC for AS1, AS2, and AS3 where  $l_{pump} = 0$  and  $l_{Stokes}$  varies ( $\pm 1$  and  $\pm 2$ ). The last column indicates the number of hot spots and their directions on the focal plane of the convex lens that is located after each vortex. As it is shown in table 3.3, for the anti-Stokes sidebands, which have a negative value of TC, the direction of the tilt of the hot spots is from right to left (columns 2 and 6), and for the Stokes sidebands the direction is opposite (columns 4 and 8). We also repeat the experiment when both input beams are modulated, meaning that  $l_{pump}$  and  $l_{Stokes}$  both have non-zero values.

In this case, we pass both beams through the two separate desired phase masks on the SLM. To fit both pump and Stokes on the SLM, we use a telescope before the non-polarizing beam splitter to reduce the size of the original beams down to 25%. Although, as seen in figure 3.4, the intensity

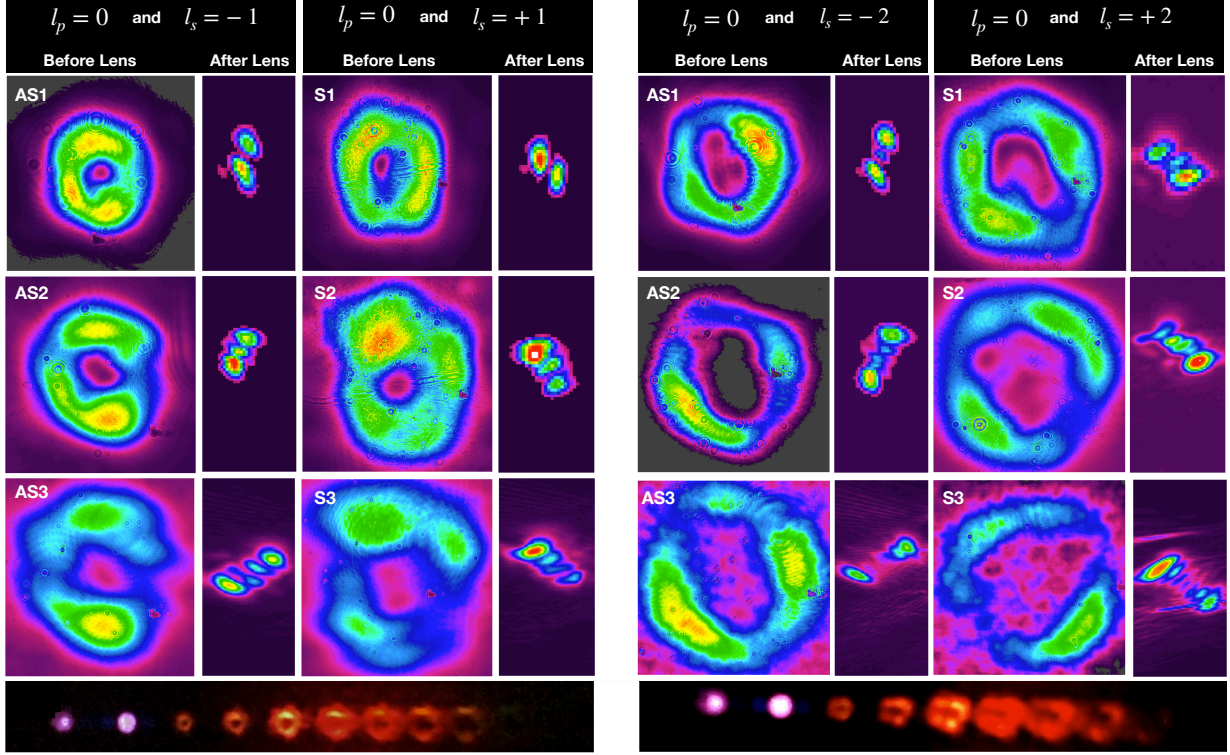


Figure 3.3: Tilted bi-convex lens technique to measure the TC of vortex Raman sidebands.  $l_p$  stands for  $l_{pump}$ ,  $l_s$  stands for  $l_{Stokes}$ , and  $ASn$  stands for the  $n$ th anti-Stokes. Four different configurations are considered:  $l_p = 0$  and  $l_s = \pm 1, \pm 2$ . In all four cases, a Gaussian beam is used as the pump ( $l_p = 0$ ), but the Stokes beam's TC varies. The output sidebands' TCs can be detected by the number of bright spots and the direction of their tilt at the focal plane of a bi-convex lens. In our experiment, we find that the optimal angle that this lens was located with respect to the incoming sideband was  $\sim 6^\circ$ . The last row shows the real footage of the vortex Raman sidebands on the screen inserted after the  $PbWO_4$  crystal. The bottom left shows the anti-Stokes sidebands on the screen when the  $l_s = -1$ , and the bottom right is the counterpart but for  $l_s = -2$  (adapted from [91]).

distribution of the output sidebands is not as clear as in the former case, we still can verify the value and sign of their TC easily by observing the hot spots after the tilted bi-convex lens.

### 3.4 Results and Discussion

In the first part of the experiment, we successfully generate up to 7 high-quality Stokes and anti-Stokes sidebands while only one input beam is modulated ( $l_{pump} = 0$  and  $l_{Stokes} = \pm 1$ ). These sidebands are present without any parasitic backgrounds and noise. Although we are able to

Table 3.3: TC values of output sidebands and the number and the direction of the bright spots in tilted lens technique for different  $l_{Stokes}$ .

Sideband's order (n)	$l_{Stokes}$	Measured TC	Number and direction of the spots
1	$\mp 1$	$\pm 1$	2 spots in the positive (negative) direction
2	$\mp 1$	$\pm 2$	3 spots in the positive (negative) direction
3	$\mp 1$	$\pm 3$	4 spots in the positive (negative) direction
1	$\mp 2$	$\pm 2$	3 spots in the positive (negative) direction
2	$\mp 2$	$\pm 4$	5 spots in the positive (negative) direction
3	$\mp 2$	$\pm 6$	7 spots in the positive (negative) direction
1	$\mp 3$	$\pm 3$	4 spots in the positive (negative) direction
2	$\mp 3$	$\pm 6$	7 spots in the positive (negative) direction
3	$\mp 3$	$\pm 9$	10 spots in the positive (negative) direction

increase the number of the generated vortex sidebands up to 15 by increasing the power of the input beams right before reaching the burning point of the  $PbWO_4$  crystal, the quality of the sidebands reduces significantly, and the noise is unavoidable. We also perform the same experiment where  $l_{pump} = 0$  and  $l_{Stokes} = \pm 2$  and  $\pm 3$ . In all these four cases, the intensity of the generated sideband is less than for  $l_{Stokes} = \pm 1$  with the same input intensity, limiting our results to only six high-quality sidebands for  $l_{Stokes} = \pm 2$  and 5 for  $l_{Stokes} = \pm 3$ . This fact is due to the increase in the bright area of the OVs as  $l_{Stokes}$  increases as shown in and calculable from [98, 99]. So, as we expect, the intensity of a beam with  $l = 2$  is 75% of that for a beam with  $l = 1$ , and the intensity of a beam with  $l = 3$  is 83% of that for an  $l = 2$  beam.

According to the section 3.3.2, by counting the number of hot spots and checking the direction of their tilt, we can measure the TC of AS1 and verify that it indeed satisfies equation 3.6. Table 3.4 summarizes the results of the TC measurement for this part of the experiment.

Figure 3.4 summarizes the result for the second part of the experiment where both input beams are modulated ( $l_{pump} \neq 0$  and  $l_{Stokes} \neq 0$ ). We vary the values of the TC for the input pump and Stokes while keeping the difference constant, meaning that  $|l_{Stokes} - l_{pump}| = 3$ , and then record

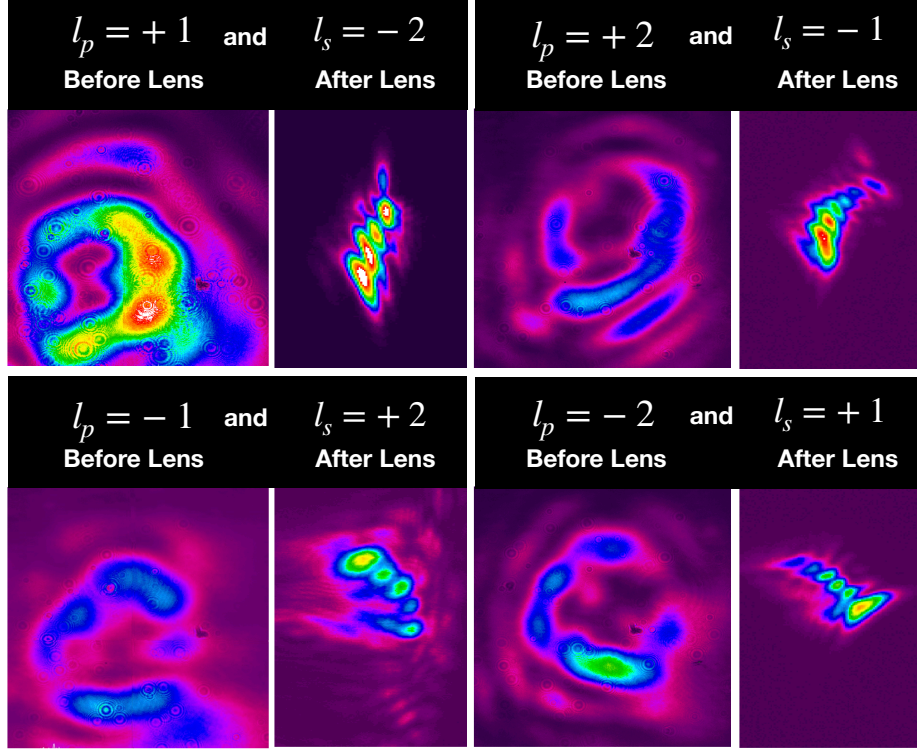


Figure 3.4: Generation of the first sideband (AS1) in the Raman process using two modulated beams;  $l_{Stokes}$  and  $l_{pump}$  both have non-zero values.  $l_p$  stands for  $l_{pump}$  and  $l_s$  stands for  $l_{Stokes}$ . The first and the third columns show the AS1 itself, and the second and the last columns show the hot spots after the tilted bi-convex lens to verify the value and the sign of the TC. The heading shows the  $l$  values for each input beam. The values for the TC of AS1 in each case are shown in table 3.4.

Table 3.4: TC values for AS1 as  $l_{pump}$  and  $l_{Stokes}$  vary. The last column shows the number and the direction of the bright spots after the tilted bi-convex lens verifying the value and the sign of the TC of AS1 in each case.

$l_{pump}$	$l_{Stokes}$	Measured TC for AS1	Number and direction of the spots
+1	-2	4	5 spots in the positive direction
-1	+2	-4	5 spots in the negative direction
+2	-1	+5	6 spots in the positive direction
-2	+1	-5	6 spots in the negative direction

the beam profile for the first sideband, i.e., AS1. We then pass AS1 through a tilted lens with an angle of  $\sim 6^\circ$  with respect to the plane that is perpendicular to the direction of the incident sideband.

### 3.5 Summary and Conclusion

The importance of OVs in science and technology motivates our study of the TCs and their transfer during the coherent Raman interaction in solid transparent material such as Raman crystals. We explore the possibility of adding another aspect to the light-field shaping by adjusting the transverse input beam profiles in coherent Raman interaction in  $\text{PbWO}_4$  crystal, and hence, generating coherent multi-color Raman sidebands of different orders of OVs. We initially shape one or two of the input pulses, called pump and Stokes in CARS terminology, using an LCOS-SLM which is a reflective spatial light phase modulator. We then generate higher orders of OVs throughout the coherent Raman interaction in the  $\text{PbWO}_4$  crystal. We use two positively chirped pulses whose duration can vary from 200 fs to 2 ps in two separate cases: 1) only one input beam initially has OAM and the other beam is a Gaussian with  $l = 0$ , and 2) both beams have OAM. Although in the latter case, due to the reduction of the bright area of the vortices, the intensity and the quality of the vortex sidebands increase compared to the first case, we still are able to measure the value and the sign of the TC for the sidebands accurately. Our findings verify the magnitude and the sign of the TC of each sideband generated in the coherent Raman process, measured using a tilted bi-convex lens technique, confirming that for each sideband, the relation between the TC of the input and output beams follows a simple equation.

## 4. SYNTHESIS OF ULTRAFAST WAVEFORMS USING COHERENT RAMAN SIDEBANDS<sup>†</sup>

### 4.1 Introduction

The need to understand and control electron motion on faster and faster time scales [100, 101] has driven ultrashort laser pulse technology towards shorter and shorter pulses. Ultrashort laser pulses are often generated with mode-locked lasers by passive and active mode-locking followed by various compressive techniques [102–104]. One of the most popular methods of generating attosecond pulses is high harmonic generation (HHG) [105, 106]. However, there are several intrinsic limitations to this technique, including its fundamental inefficiency, small energy throughput and the difficulty of controlling and maintaining single-cycle x-ray pulses [107]. Another popular method utilizes fiber-generated supercontinua split into multiple branches, compressed, and recombined to generate very short, single or sub-femtosecond pulses [8, 108, 109]. While this approach has been shown to generate relatively high power (several hundred  $\mu\text{J}$ ) and ultrafast (on the order of a single cycle or less) pulses, the pulse power is fundamentally limited by the power output of the generating fiber. Another approach utilizes noncollinear optical parametric chirped pulse amplifiers to produce pulses of several hundred mJ with pulse durations down to the approximately 6-7 fs range [110, 111]. The results reported in this work are, in principle, only limited in power by what the pump laser can produce and in bandwidth by the total generated bandwidth of the Raman process (which routinely spans 350-1100 nm). Our work is based on a technique dubbed “molecular modulation”.

In the past few decades, the molecular modulation technique has played an essential role in producing such short pulses (femtosecond and attosecond) in the optical region [112–114]. This technique is based on the frequency modulation of a laser pulse propagating through a coherently vibrating ensemble of molecules, which results in the generation of multi-color sidebands that are

---

<sup>†</sup>Reprinted with permission from “Synthesis of ultrafast waveforms using coherent Raman sidebands” by A. Bahari, A. A. Zhdanova, M. Shutova, and A. V. Sokolov, 2020, *Phys. Rev. A*, vol. 102, p. 013520. Copyright [2020] by A. Bahari.

spaced by the vibration frequency of the molecule. These sidebands, dubbed “Raman sidebands”, are all produced coherently, in phase, potentially generating sub-femtosecond pulses with any desired pulse shape where the electric field is not limited to a quasi-sinusoidal oscillation [11]. Using this technique, Sokolov *et al.* demonstrated the synthesis of a pulse train of nearly single-cycle waveforms in the adiabatic excitation of the D<sub>2</sub> molecule [32]. In a similar direction, Zhavoronkov and Korn generated pulses with duration below 4 fs [33] by utilizing a hollow-core waveguide filled with an impulsively pre-excited Raman-active gas, while Suzuki *et al.* generated an octave-spanning Raman comb from single-frequency lasers in gaseous parahydrogen [34].

The molecular modulation technique is not limited to gaseous media and has been extended to nonlinear solids such as diamond and PbWO<sub>4</sub> crystals [91, 115]. In solid-state media, it is possible to use femtosecond pulses (instead of picosecond or nanosecond) to produce coherent Raman sidebands, opening up the possibility for synthesizing single-cycle, isolated, visible pulses. Similar to gaseous media, collinear interaction is possible in solids, but due to the dispersion of the medium, result in a situation where sideband generation is optimized at a certain non-zero crossing angle. This configuration is achieved by crossing the pump and Stokes input beams at a specific angle inside the crystal [115]. As a result, the generated sidebands are produced at different output angles, and therefore, additional techniques are required to recombine these sidebands and synthesize ultrashort pulses [116–118].

In this work, we apply a novel scheme to generate and characterize a few-cycle pulse in a single polychromatic beam. Our setup uses dichroic mirrors to recombine the spatially separated sidebands, and the resulting waveform is characterized via a technique we dub interferometric cross-correlation frequency resolved optical gating (ix-FROG). This technique is a combination of cross correlation FROG (XFROG) [41] and interferometric FROG [119–122].

The cross-correlation part of the technique allows us to retrieve the waveform of each sideband, while the interferometry allows us to determine the phase of each beam with respect to the others. Although several experimental factors limit our current synthesized pulse energy and duration, a number of adjustments can be applied to the setup to overcome some of these limitations. For

instance, increasing the pump energy without reaching the damage threshold of the Raman crystal can significantly increase the energy of the sidebands, and therefore, the energy of the synthesized ultrashort pulses. Focused on the niche of molecular modulation technique, our Raman source presents a broad range of applications, for example, in optical coherent tomography, ultrafast spectroscopy, and precision metrology. Moreover, our technique can be potentially used in generating coherent radiations in the UV and IR spectral regions, where laser sources are not readily available. This work is a step toward expanding the flexibility and applicability of our technique, while paving the way towards ever-shorter pulses.

## 4.2 Experimental setup

Fig. 4.1 shows the experimental setup we used to synthesize and characterize our ultrashort pulse. We split the main laser line at 800 nm with a low-group-delay-dispersion (GDD) beamsplitter. We use one leg (called pump in coherent anti-Stokes Raman scattering (CARS) terminology) in conjunction with the second-harmonic generation (SHG) of the idler out of the optical parametric amplifier (OPA) at 870 nm (called Stokes, S1 in CARS terminology) to stimulate the  $1332\text{ cm}^{-1}$  Raman line of a 0.5 mm thick, single-crystal diamond. The OPA (Coherent OPerA) is pumped directly from the main laser line and is seeded by white light generated from a fraction of pump in a sapphire plate; hence, S1 has a carrier-envelope-phase which is, in principle, related to the carrier-envelope-phase of pump.

We combine the two beams at a  $\sim 3^\circ$  angle, focusing each individually with a 50 cm lens (S1) and a 30 cm lens (pump). The S1 beam profile is optimized with an iris prior to focusing. The average pulse energy in each beam is  $18.28\ \mu\text{J}$  (pump) and  $1.86\ \mu\text{J}$  (Stokes) as measured by a Coherent PM10 power meter. This configuration produces many orders of Anti-Stokes (AS) Raman sidebands. These sidebands are essentially frequency-shifted copies of the original femtosecond pulses. After exiting the crystal, we collimate each sideband individually. Wherever possible, thin lenses were used to avoid adding substantial dispersion. However, adding the dispersion of the lenses has a minimal effect on the final synthesized pulse so long as the relative phase between

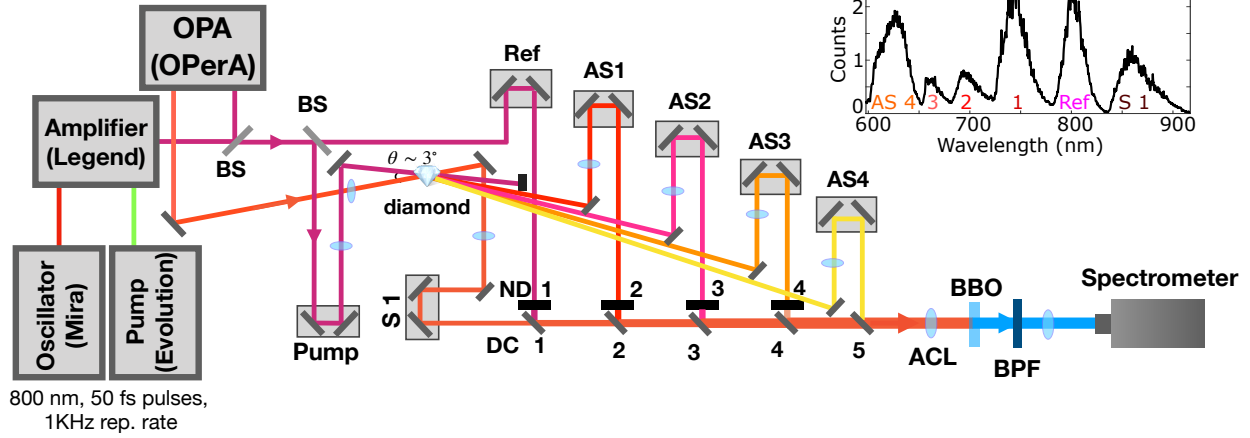


Figure 4.1: Our experimental setup to synthesize a sub-5-fs FWHM pulse. The black bars (ND 1-4) before each DC mirror represent variable neutral density filters which we use to adjust the intensity of each beam to match the intensity of AS4. Abbreviations for the optical elements: BS, 50/50 beamsplitter, DC 1-5, dichroic mirror 1-5, ACL, achromatic lens, BBO, beta-barium-borate crystal, BPF, band-pass filter. Inset: recorded average spectrum of our synthesized pulse, spanning from AS4 to S1 ( $\sim 300$  nm of bandwidth). The bands are not optimized for phase recombination.

each band is properly adjusted as part of the interferometric setup. This is because, despite the dispersion of the lenses, the phase in the most intense part of each beam remains relatively flat (smooth,  $< 2\pi$  change across 100 fs), as shown in Fig. 4.2. Moreover, the synthesized pulse duration is mainly affected by the total frequency span of the sidebands which participate in the synthesis, and this factor is not affected by the dispersion added from the lenses, neutral density (ND) filters, etc. used in our setup.

After collimation, each band is aligned to a separate delay line to allow for full control of phase and flexibility of position. These bands are then recombined with the remains of S1 after the diamond and the other leg of the split main laser line (dubbed “Reference”).

We used commercially available dichroic mirrors for this recombination, and the recombined spectrum is shown in the inset of Fig. 4.1. Some sidebands’ spectra have reduced bandwidth due to the cutoff frequencies of the dichroic mirrors, as is consistent with the retrieved pulse shapes in Fig. 4.2. Full information on the collimation lenses, dichroic mirrors, and translation stages used in the setup are available in Table 4.1. We found the power of the least powerful sideband (i.e.

Table 4.1: Part numbers for the dichroic mirrors and translation stages; focal lengths for the collimation lenses used in this setup. Part numbers starting with “TL” correspond to Thorlabs part numbers, “NP” - Newport, “EO” - Edmund Optics, and “SR” - Semrock.

Band	Delay stage	Collimating lens(es)	DC mirror
S1	NP 423 series	50 cm	N/A
Ref.	TL LNR25ZFS	N/A	EO 69-895
AS1	NP GTS150	40 cm	SR FF776-Di01
AS2	NP 443 series/TL PAS005	15 cm & -10 cm	SR FF735-Di02
AS3	TL LNR25ZFS	25 cm & -10 cm	SR FF685-Di02
AS4	NP 423 series	30 cm & -10 cm	SR Di03-R635-t1

AS4) after recombination to be 6.5 nJ (in comparison to AS1’s 200 nJ of power); the power of all other sidebands was reduced with ND filters to match this power.

After dichroic recombination, we used a single achromatic doublet lens to focus the beams into a 10 micron beta-barium-borate (BBO) crystal to characterize the resultant pulse. Specifically, second harmonic and sum frequency signals of the sidebands are generated in the BBO in the spectral range 340 – 450 nm, with intensity dependent on phase relation between individual sidebands in an interferometric configuration. After exiting the crystal, the fundamental sideband frequencies are filtered depending on which spectral region is under investigation. For signals above 390 nm, a lone Thorlabs FGB25 UV band-pass filter (BPF) was used; otherwise, an additional Thorlabs FGUV11 BPF was added.

The resulting UV signal was focused with a 7.5 cm lens into a multi-mode fiber and analyzed via a spectrometer (Ocean Optics HR4000). Different nonlinear signals result from blocking or unblocking different bands, as discussed in the following sections.

It is important to note that our setup currently has no active stabilization or noise jitter suppression. While this does preclude the use of the setup presented herein from single-shot measurements, we use the results presented in Fig. 4.3 to show that the setup is stable enough to repeatedly and reliably measure intensity fluctuations on the sub-single-femtosecond scale. Hence, our setup allows us to take repeated interferometric measurements which we can then average to reduce the

noise. Active suppression of the noise would result in more consistent results and can be implemented in future iterations of this setup.

### 4.3 ix-FROG pulse retrieval

The first step in our ix-FROG technique is to record standard XFROG spectrograms for each beam. These spectrograms were taken and recorded individually (i.e. by blocking and unblocking various beams) to ensure no extra noise or background from the interference terms described below. However, it is also possible to take all spectrograms simultaneously by removing the resultant sum-frequency generation (SFG) background and filtering out the higher-order interference terms, as is done in [120]. We used the 800 nm band dubbed Reference as our known pulse; we first characterized this pulse with a separate homebuilt SHG-FROG setup. This setup utilized a very small ( $< 3^\circ$ ) recombination angle and 10 micron BBO, achieving results consistent with what we expect from our commercial laser amplifier. This SHG-FROG trace is shown in Fig. 4.2(b).

Collinear XFROGs were then taken with all dichroics and filters in place; we varied the delay of Reference with respect to all other beams as our gating pulse. We used the standard XFROG algorithm provided on Dr. Trebino's website for pulse retrieval [123]. Fig. 4.2 displays the results. We successfully retrieved the Raman sideband pulse shapes with  $< 2\%$  RMS difference between the experimentally obtained spectrograms and FROG-reconstructed spectrograms, indicating very good retrieval. Severe distortions in the pulse shapes of AS2 and AS3 stem from the variable group-delay-dispersion (GDD) in their respective dichroic mirrors close to the cut-off frequency [124].

Once collinear XFROGs were individually taken, a full spectrogram was obtained by unblocking all beams. This full spectrogram shows clear interference on all bands, at a period roughly equal to  $1.2 \text{ fs}$  or  $1/f$ , where  $f$  is the frequency of the band under question. This is expected by the interaction and coherence between all nonlinear signals. For example, in Fig. 4.3(a, d), the 350 nm band represents the interference between the second harmonic of AS3 with the sum-frequency of AS2 and AS4. Similarly, the 360 nm band represents the interference between the second harmonic

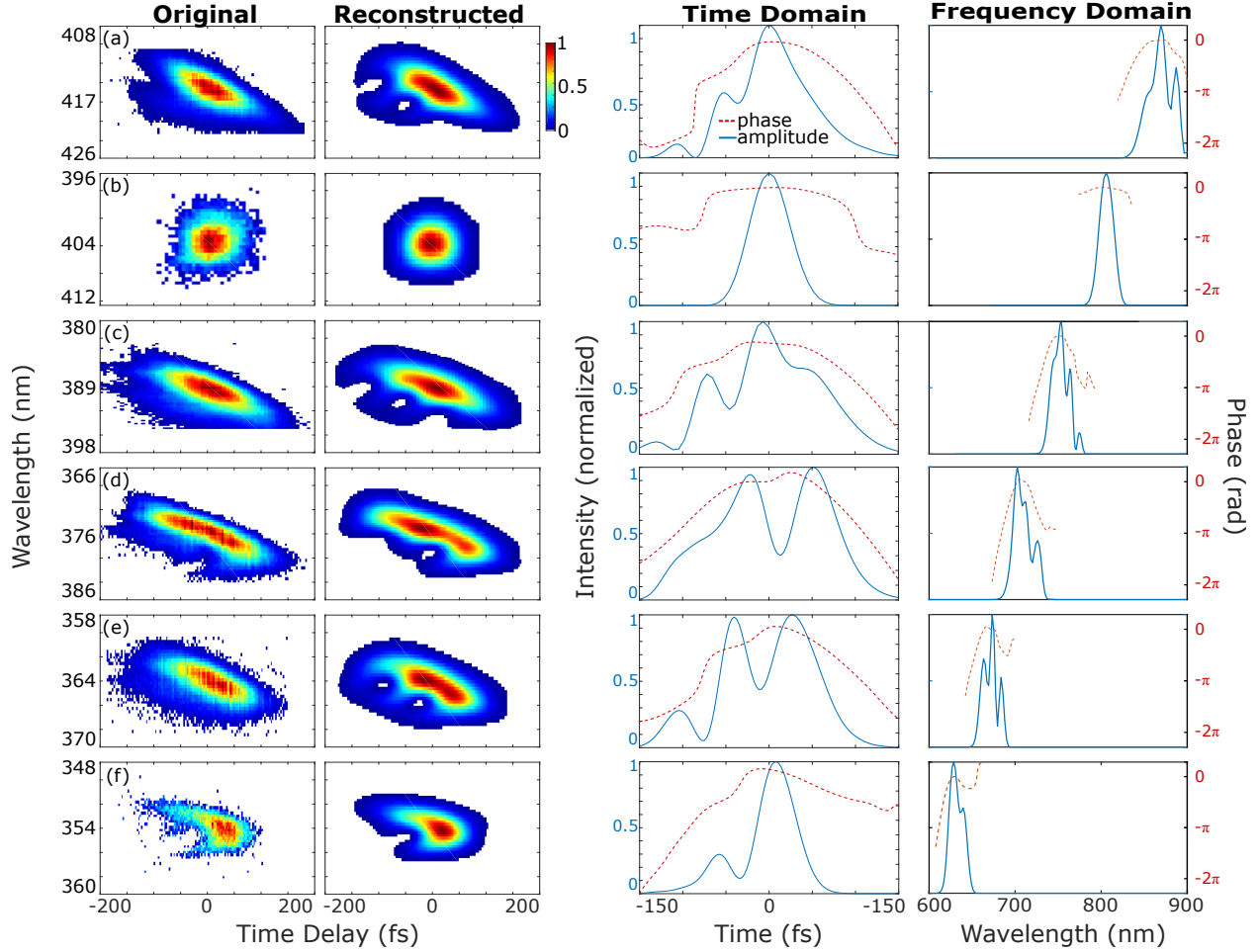


Figure 4.2: Experimental XFROG spectrograms of all beams employed in our setup, using Reference as the known pulse to gate (a) S1, (b) itself in an SHG FROG configuration, (c)-(f), AS1-4. The columns show the measured and reconstructed spectrograms, as well as a plot of the retrieved temporal pulse shapes (phase and amplitude).

of AS2 with the sum-frequency of AS1 and AS3, as well as the interference between Reference and AS4. Detailed descriptions of the terms which contribute to the interference are given in [121].

In this setup, we can vary the delay of any of the sidebands to obtain such an interferometric picture. However, as proof-of-principle, we only examine the results of varying the delay of AS3, as shown in Fig. 4.3(a,d). To make the details of the interference patterns more visible, when plotting the spectrograms we subtracted the constant background and interpolated to a 0.17 fs step size (1/4 of the actual step size) using standard spline interpolation. By adding or removing phase

from a particular beam, the interference channels shift with respect to each other, as discussed further in Section 4.4. In essence, the ix-FROG technique measures relative phase between the sidebands. Combining it with the XFROG pulse measurement technique, we find the shape of the multi-sideband waveform.

Note that in our proof-of-concept setup we do not use carrier-envelope phase (CEP) stabilization of pump or Stokes pulses. It is important to realize that since the OPA is seeded by pump, the CEP of the Stokes beam is preserved during the white light generation process, however, it is impossible to be predicted because it changes on a shot-by-shot basis. This means that the relative phase of the pump and Stokes remains constant, but the CEP changes shot to shot. Since the phase of each anti-Stokes sideband depends on phases of both pump and Stokes pulses, it is reasonable to ask if the shape of our synthesized waveform is stable from one shot to another. To see why that is the case, let us denote the CEP of the pump pulse as  $\phi_p$  and CEP of the Stokes pulse as [11, 125]:

$$\phi_n = \phi_p + n(\phi_p - \phi_S) \quad (4.1)$$

while the frequency of  $n$ -th order sideband is given by

$$\omega_n = \omega_p + n(\omega_p - \omega_S) \quad (4.2)$$

(where  $\omega_p$  is the frequency of pump and  $\omega_S$  is the frequency of Stokes). Mathematically, the frequency and phase of pump and Stokes pulses also follow Eqs. (4.1) and (4.2) with  $n = 0$  and  $n = -1$  respectively, so in the experiment, we combine sidebands with indices  $n = -1, 0, 1, \dots, 4$ . Equations (4.1) and (4.2) show that CEPs of all combined bands are linear in frequency  $\omega_n$ :

$$\phi(\omega_n) = \phi_p + \frac{\omega_n - \omega_p}{\omega_p - \omega_S} (\phi_p - \phi_S) \quad (4.3)$$

It follows then from Fourier theory that random changes in  $\phi_p$  and  $\phi_S$  affect the synthesized waveform in two ways: 1) change in CEP of the waveform and 2) random shift in time. In other words,

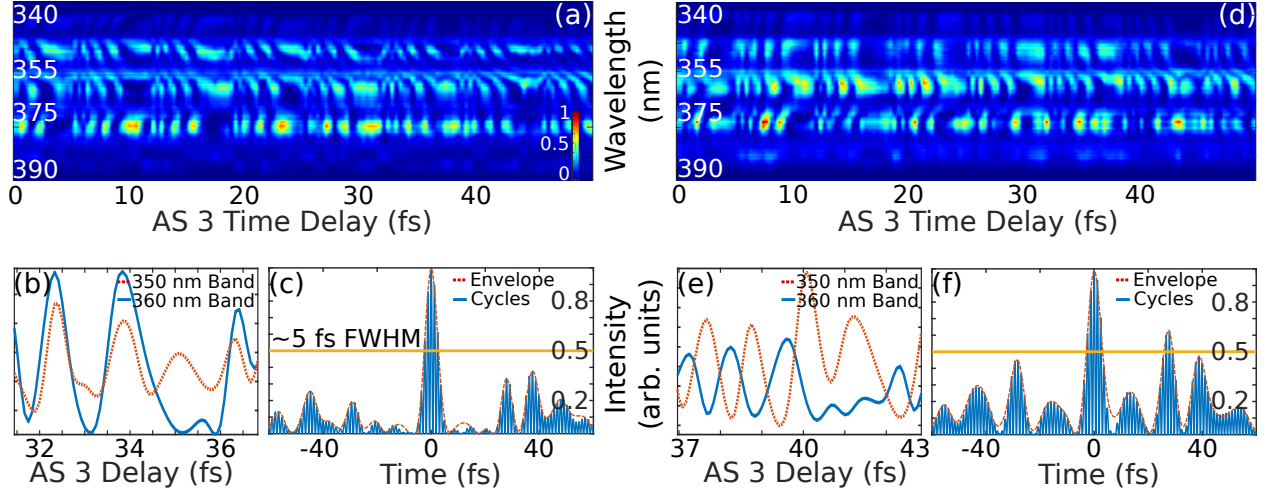


Figure 4.3: Comparison of experimentally measured ix-FROG traces for the waveforms formed by AS2 being in-phase (a–c) and out-of-phase (d–f) with the other sidebands. (a,d) Full spectrograms (spectrum of the sidebands as a function of AS3 sideband delay). (b,e) Cuts of the spectrogram at the 350 nm band (red dashed line) and at the 360 nm band (blue dashed line). When AS2 is in phase with the rest of the sidebands (in-phase waveform, (b)), the maxima of the interference fringes in the 350 nm and the 360 nm bands of the ix-FROG trace are aligned. When AS2 is out of phase with the rest of the sidebands (out-of-phase waveform, (e)), the maxima of the interference fringes in the 350 nm band correspond to the minima in the 360 nm band. (c,f) Reconstructed temporal profile of the in-phase (c) and out-of-phase (f) waveforms; assuming a carrier-envelope-phase of 0.

even though both  $\phi_p$  and  $\phi_S$  are random, the shape of the envelope of the synthesized pulse does not change (although its precise arrival time does).

Essentially, the main knob affecting the pulse shape in our waveform synthesis setup is a constant, additional phase between the sidebands, which depends on  $n$ , but not on CEP  $\phi_p$  or  $\phi_S$ . This extra phase between sidebands is controlled via adjustment of the optical paths of the bands. Finally, as discussed in Section 4.2, our Stokes beam is generated from the pump beam. Hence, in principle, since the carrier-envelope-phase of our setup is only affected from shot to shot by the CEP of our pump laser, our setup is compatible with standard methods of CEP stabilization [126]. Note that our technique is decoupled from the standard CEP stabilizing methods such that CEP stabilization does not affect the results of this manuscript.

## 4.4 Results

Once all pulses are overlapped in space and time, a waveform is synthesized throughout the beam by the coherent addition of the individual sidebands. As discussed previously, the shape of the synthesized waveform is controlled by the phase relationships between sidebands. This is seen qualitatively in the ix-FROG traces of the waveforms which examine the phase of AS2 with respect to the other sidebands (Figs. 4.3(a) and 4.3(d)). For the in-phase waveform the interference fringes in various bands of the ix-FROG spectrogram are aligned, i.e. have maxima at the same AS3 delay (Fig. 4.3(b)). In Fig. 4.3(c)-(f), we add an extra phase to AS2 by moving its piezoelectric stage slightly forward.

This results in an out-of-phase waveform where the spectrogram interference fringes are anti-aligned – maxima at 350 nm and 370 nm bands correspond to minima at 360 nm band and vice versa (Fig. 4.3(e)).

By putting all pulses in phase (i.e. by stopping on a bright spot in Fig. 4.3(a)) we obtain an isolated 5 fs pulse, as shown in Fig. 4.3(c). Setting all beams in phase is essential for optimal synthesis to take place; if AS2 is out of phase with all the other beams, the temporal contrast of the main pulse with respect to the pre- and post-pulse worsens; technically, a 30 fs FWHM pulse is obtained (even though the FWHM of the main pulses increases only slightly to 6 fs). This is also shown in Figs. 4.3(c,f).

A detailed inspection of the ix-FROG traces shows more structure than simply in and out of phase interference fringes. For instance, periodically, fringe visibility drops dramatically for about  $\sim 4$  fs of the AS3 delay. Fringes in the 360 nm band are also tilted, i.e. fringe maxima at different wavelengths within a band correspond to different AS3 time delays. Our qualitative model of ix-FROG does not account for any of these effects, and these will be the subject of a future publication.

## 4.5 Conclusions

We have demonstrated that, by using our ix-FROG technique, we can synthesize and measure an isolated (3:1 signal-to-noise) 5-fs pulse. This setup is only limited in bandwidth and power by what is produced in the Raman process and can be scaled in both to produce single-cycle isolated pulses at a much higher power, ideal for studying ionization and other processes on the single-femtosecond time scale.

## 5. TOWARDS ULTRASHORT PULSES BY SYNTHESIZING COHERENT RAMAN SIDEBANDS<sup>†</sup>

### 5.1 Introduction

In this chapter, I will elaborate on our published work in chapter 4. The data in this chapter includes up to 7 sidebands added to the collinear synthesis. Our initial aim was to add even more sidebands, however, due to the reduction of the power of the final ultrashort pulse, the last anti-Stokes sideband (i.e. AS5) was left out of the data and the analysis on the manuscript. The results in the following sections discuss both cases of synthesis of 6 beams (pump, Stokes, AS1-4) as well as 7 beams (pump, Stokes, AS1-5). Moreover, time-resolved beats in the interferometric cross-correlation frequency-resolved optical gating (ix-FROG) spectrograms are shown and discussed later on in this chapter. At the end of the chapter, I will discuss our preliminary results from Xenon (Xe) multi-photon ionization experiment using our synthesized pulses.

### 5.2 Experimental Setup

Figure 5.1 illustrates the experimental setup we built to synthesize an ultrashort pulse by the collinear combination of 7 sidebands. This is the exact setup that is used in chapter 4 and is fully explained in section 4.3. The only difference is one more sideband that is added to the configuration at the end of the collinear path. The inset shows the non-quantified spectra of all the sidebands. The crystal used in this section is the same 0.5 mm thick single crystal diamond (Element Six 145-500-0385) that is described in table 2.1.

Table 5.1 shows the optical and mechanical parts used in AS5's path. All the bands are collimated separately by using several concave and convex thin lenses in their paths. The reason for the collimation is that all the sidebands diverge while leaving the crystal due to the initial focus of the pump and the Stokes. Finding the right place for these thin lenses was a matter of trial and error

---

<sup>†</sup>This chapter further elaborates and presents more data from previous chapter

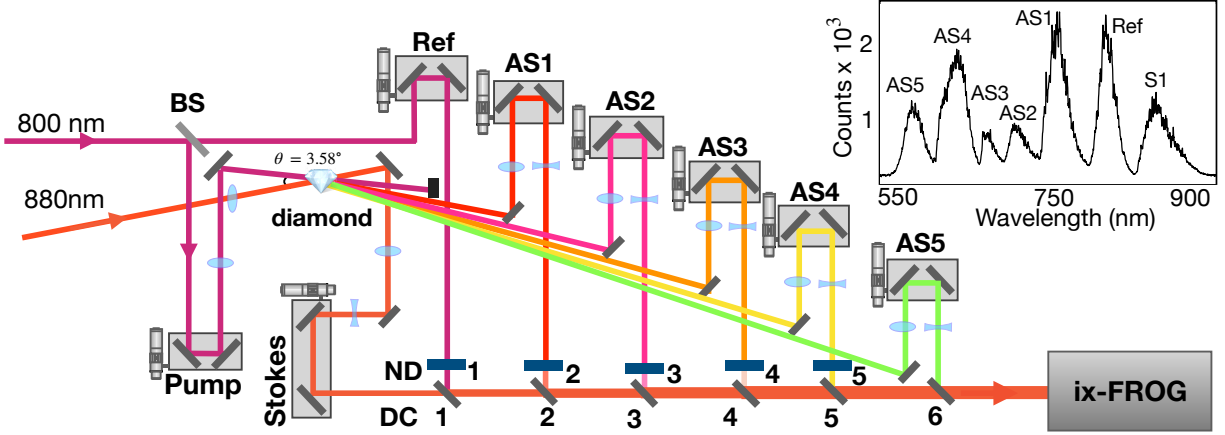


Figure 5.1: The experimental setup for the synthesis of a near-single-cycle pulse by adding 7 coherent Raman sidebands collinearly. The temporal delay between all the sidebands is The dark navy bars (ND 1-5) before each DC mirror represent variable neutral density filters which we use to adjust the intensity of each beam to match the intensity of AS5. Abbreviations for the optical elements: BS, 50/50 beamsplitter, DC 1-6, dichroic mirror 1-6, ix-FROG, interferometric cross-correlation frequency-resolved optical gating. Inset: recorded average spectrum of our synthesized pulse, spanning from AS5 to S1 ( $\sim 350$  nm of bandwidth). Here, the bands are not optimized for phase recombination yet.

Table 5.1: Part numbers for the dichroic mirror and translation stage; focal lengths for the collimation lenses used in the path of AS5. AS stands for anti-Stokes and DC stands for the dichroic mirror. The DC used for this section is purchased from Semrock.

Band	Delay stage	Collimating lens	DC mirror
AS5	Newport 433 series	40 cm & $-30$ cm	FF605-Di02

since the complexity of the setup causes frequent blockage in the path of each individual sideband. Collimating the beams is necessary to preserve the same focal point for all the sidebands at the end of the collinear path where the synthesized pulse enters the ix-FROG setup.

However, using this number of lenses to achieve the collimation could be avoided if we use a custom-made achromatic doublet, but this option is not cost-friendly. We used a single achromatic doublet (Thorlabs AC254- 100-B-ML) to focus the beams into the beta-barium-borate (BBO)

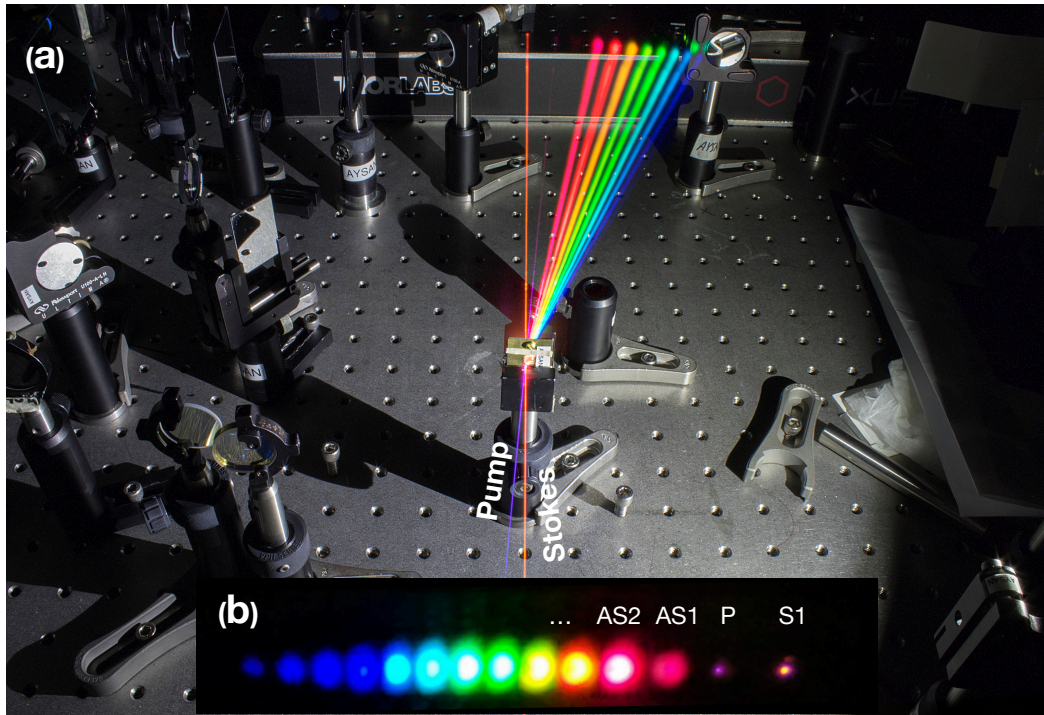


Figure 5.2: Real photograph of the Generation of the coherent Raman sidebands in the diamond. (a) Two Gaussian laser beams, pump (purple - 800 nm) and Stokes (dark orange - 880 nm) enter the diamond and generate a broadband spectrum of higher-order anti-Stokes. This photo is taken by moving a white screen in front of the sidebands in a dark room and increasing the camera exposure to 30 seconds. The camera used for taking this high-quality image is a Canon EOS 80D. Later, another mask that is taken in a slightly brighter room is edited on the photo. (photo and editing credit: Dustin Scriven from Cyclotron Institute at Texas A&M University). (b) Image of the coherent Raman sidebands on the screen (True color, taken by the author and with a Canon EOS 90D).

crystals. Two different BBO crystals are used, one for visual detecting purposes (1 mm, Newlight Photonics, BTC5100-SHG800(I)-P) and a thinner one (10 microns, crystal (Newlight Photonics BTC5001-SHG800(I)-P) to collect the final and more precise results. They both were mounted on a rotation mount (Thorlabs RSP1) for proper phase-matching angles (stronger SHG/SFG signals) for each pair of the sidebands. For example, to find the sum frequency of two different sidebands we focus them both into the BBO. Then we block one of the beams and rotate the crystal until we find the beam's SHG signal which usually is detectable by using a UV filter to filter out the fundamental beams. Then, we record the angle and repeat the process for the second beam. We

then, unblock both beams and set the mount to an angle right in the middle of the two recorded ones. If the beams are aligned well and overlapping both spatially and temporally, we should be able to see their SFG signal in the middle wavelength. These nonlinear signals are detectable using credit card-size fluorescent cards (Thorlabs, VRC1) for stronger signals and a spectrometer (Ocean Optics, HR4000) for the weaker ones. Figure 5.3 shows an example of a detected SFG signal on a spectrometer. After detecting the SFG signal, we adjust the mirrors and the delay stages to get the SFG signal as strong as possible. We repeat the whole process for all of the sidebands.

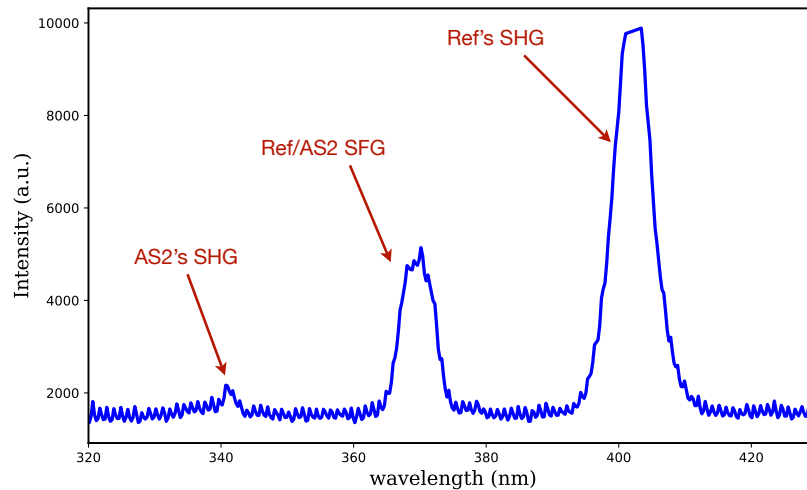


Figure 5.3: Spectrum of the SFG of the reference and AS2 beams. The SFG signal for most of the sidebands is in the UV range which is hard to detect with the naked eye or a UV detection card due to the weakness of the higher-order sidebands. The BBO crystal is fixed on a rotating mount. A UV filter and an AC lens are placed right after the crystal to remove the spectrum of the fundamental signals and direct the SHG and SFG beams into a spectrometer. By rotating the mount, the angle for the SHG signals of the reference pulse and each sideband (S1-AS5, separately) are recorded. Then, the mount is rotated and set on the angle right in between the two recorded numbers for the SHGs. Afterward, small changes in the time delay between the two pulses are made (keeping the reference delay stage fixed) until the highest peak for the SFG signal is obtained. This is the best temporal and spatial overlap for the two pulses. This process is repeated for each individual sideband in cross-correlation with the reference pulse.

As reported in chapter 4, we were able to produce a  $\sim 4.8$  fs pulse using 6 Raman sidebands (in-

cluding the reference and S1) whose bandwidth spans over 300 nm. However, to generate a single fs pulse, the bandwidth needs to be extended to 435 nm which means the collinear recombination of 10 sidebands (up to AS8). With our current setup described in figure 5.2, this recombination is possible, however, there are two factors that currently interfere with adding more sidebands. First, is the physical limitation: there are many optical and mechanical parts used in the setup, and managing more parts without blocking the path of the other beams is challenging. Second, the intensity of each sideband decreases, and since we are using a sum frequency generation (SFG) setup to find the temporal and spatial overlap between the reference beam and each anti-Stokes, the detection of the UV SFG signals becomes harder and harder for higher order anti-Stokes. To partially filter the reference and Stokes bands while detecting their SFG, we used a UV bandpass filter (Thorlabs FGB25) before the spectrometer. The same filter was used to filter out the reference and AS1 bands while detecting their SFG. For the interference between the rest of the sidebands (AS2-5) with the reference pulse, another UV bandpass filter was used (Thorlabs FGUV11). More detail and data are available in Appendix A.

Table 5.2: The power of each sideband after exiting the single-crystal diamond, before entering the collinear combination path, and after the collinear combination path and right before the ix-FROG setup. P stands for power; DC stands for dichroic; Ref, reference; AS1-5, anti-Stokes 1-5.

Sideband order	P after diamond (mW)	P before DC mirror (mW)	P after DC6 (mW)
Ref	NA	66	62
Stokes	1.58	0.5	0.4
AS1	0.310	0.250	0.2
AS2	0.070	0.050	0.040
AS3	0.035	0.020	0.003
AS4	0.020	0.007	0.007
AS5	0.011	0.004	0.004

To measure the power of each Raman sideband, we use two different power meters based on

the power range: a Coherent Field Max II power meter with PS10 head for more intense sidebands (Ref, S1, and AS1 whose powers are higher than 0.5 mW), and an Ophir Vega meter with PD10-pj-C head for the rest of the sidebands. The powers of the pump and the Stokes before entering the diamond are 18.28 mW and 1.86 mW, respectively. Since the Stokes beam is the SHG of the idler out of the OPA (OperA ), its profile needed to be cleaned by inserting an iris in its path before focusing on the diamond. After entering the diamond, the pump power reduces to 10.78 mW, meaning a conversion efficiency factor of 0.4. The maximum power of each sideband is described in table 5.2. The reason that the power of AS3 is decreased significantly after the last DC compared to the rest of the sidebands is that the DC used for AS4 reflects the wavelength range that partially covers the wavelength of AS3. In the later iteration of this experiment, this problem is resolved by substituting DC4 with another mirror. At the end of this chapter, new data is presented that shows that indeed we can improve the power of all sidebands by using several experimental tricks. The main factor that improved the power of the sidebands was to change the wavelength of the Stokes beam from 870 nm to 880 nm. This, indeed, resulted in sidebands with slightly different wavelengths.

### **5.3 SHG-FROG and x-FROG Traces**

Frequency-resolved optical gating is an excellent technique to measure a weak unknown pulse using a strong known pulse. FROG exploits an algorithm called "the method of generalized projection," which is explained in detail in section 2.3.1. We combine the SHG-FROG and cross-correlation FROG with interferometry techniques to measure and analyze each coherent Raman sideband alongside the final synthesized near-single-cycle pulse. The FROG traces shown earlier in section 4.3 are taken while the reference beam was aligned using Edmond Optics DC mirror. The results presented in this section are obtained using a different DC mirror from Semrock. We were able to recombine up to 7 sidebands using the latter one; however, due to the significant distortion in the pulse shapes, the temporal profile of the final synthesized pulse is unavoidably asymmetric. Although these distortions coincide well with the GDD of the mirror, to obtain better profiles, we

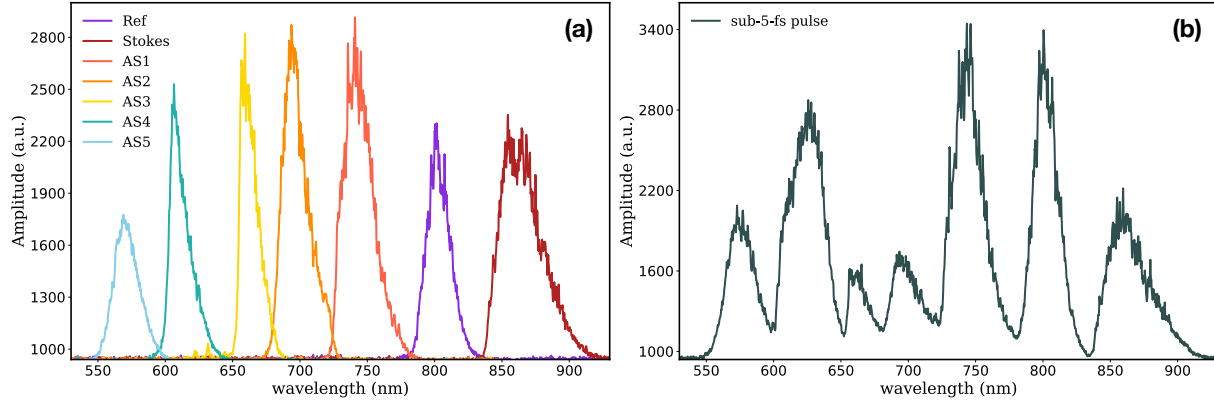


Figure 5.4: (a) Spectra of all the coherent Raman sidebands which were included in the collinear combination to generate a near-single-cycle pulse. These spectra are taken separately, and their maximum peak is not quantitative at the recombination point. (b) The total spectrum of our sub-5-fs pulse, combined from 7 coherent Raman sidebands ( $\sim 350$  nm of bandwidth). All the sidebands, except AS5, are partially reduced in power by dichroic mirrors and neutral density filters to match the intensity of the weakest sideband (AS5); however, the bands are not optimized yet for phase recombination. This spectrum is taken at the point of the ix-FROG measurements in figure 5.1.

decided to change the DC mirror by the end of our experiment, which resulted in adding one less sideband to the collinear combination because the alignment of the setup with the new mirror was a difficult and tedious process, especially for the weakest sideband, i.e., AS5. This difficulty is caused by the instability of the source, beams traveling through long distances, collinear recombination, and the fact that the temporal and spatial overlaps are done by passing each couple of beams through a BBO crystal at a zero angle which cannot follow the phase matching angle protocols. The results taken by using the Semrock DC mirror are presented in this section. Figure 5.5 shows the SHG-FROG and the cross-correlation FROG (x-FROG) traces for the reference pulse and the rest of the sidebands, respectively.

The retrieved pulse envelope and phase for this data set are shown in figure 5.6, which visibly shows the distortion compared to the envelope and phase in figure 4.2 where Edmond Optics DC mirror was used. Results in this section suggest that we can scale our setup to add as many sidebands to the collinear recombination until the synthesized pulse at FMHM reaches the minimum duration that we are looking for. However, aligning these many sidebands without running into

experimental difficulties is almost impossible.

Figure 5.6 shows the retrieved pulse phase and envelope for all the coherent sidebands (Ref, S1, AS1-5). The noticeable asymmetry in each plot indicates the distortion that was caused by the DC mirror that was used at the collinear path to align the reference beam. This distortion was partially avoided by changing the mirror in the results from section 4.3. To fully remove this added dispersion, one can use chirped mirrors at the end of the path of each sideband; however, that will not be cost-effective. Moreover, according to our simulations, the second or third-order dispersion of each pulse does not substantially affect the final synthesized pulse. The synthesized pulse duration is mainly affected by the total frequency span of the sidebands which participate in the synthesis, and this factor is not affected by the dispersion added from the lenses, neutral density (ND) filters, etc. Figure 5.7 shows the pulse envelopes and the sub-cycle structure of the synthesized pulse's electric field that is calculated by Fourier transforming the spectrum that is taken by experimental measurement. The pulse length at FWHM changes from  $\sim 4.8$  fs to  $\sim 4.5$  fs when AS5 is added to the collinear combination. The full pulse envelope repeats every 120 fs. By changing the relative phases between the sidebands, the temporal profile and temporal length are adjustable.

#### 5.4 Beat Notes Analysis

To improve the temporal profile of the final synthesized pulse, we make sure that all the involving beams in the collinear combination are in phase with each other since Fourier transform theory (FTT) implies that the narrowest pulse envelope is achievable when  $\phi_n$  which is the spectral phase of the  $n$ th sideband is constant and it satisfies the linear relation  $\phi_n = \phi_{CEP} + n\phi_m$ . Here,  $\phi_{CEP}$  is the carrier-envelope phase, and  $\phi_m = \phi_p - \phi_{St}$  is the modulation phase, and both only depend on the initial phase of the pump and the Stokes.

The importance of this in-phase and out-of-phase analysis is shown in figure 4.3 (c,f). By combining all the sidebands in phase, we can change the pre- and post-pulse wing temporal shapes through constructive and destructive combination and can subside the pre- and post-pulse wings

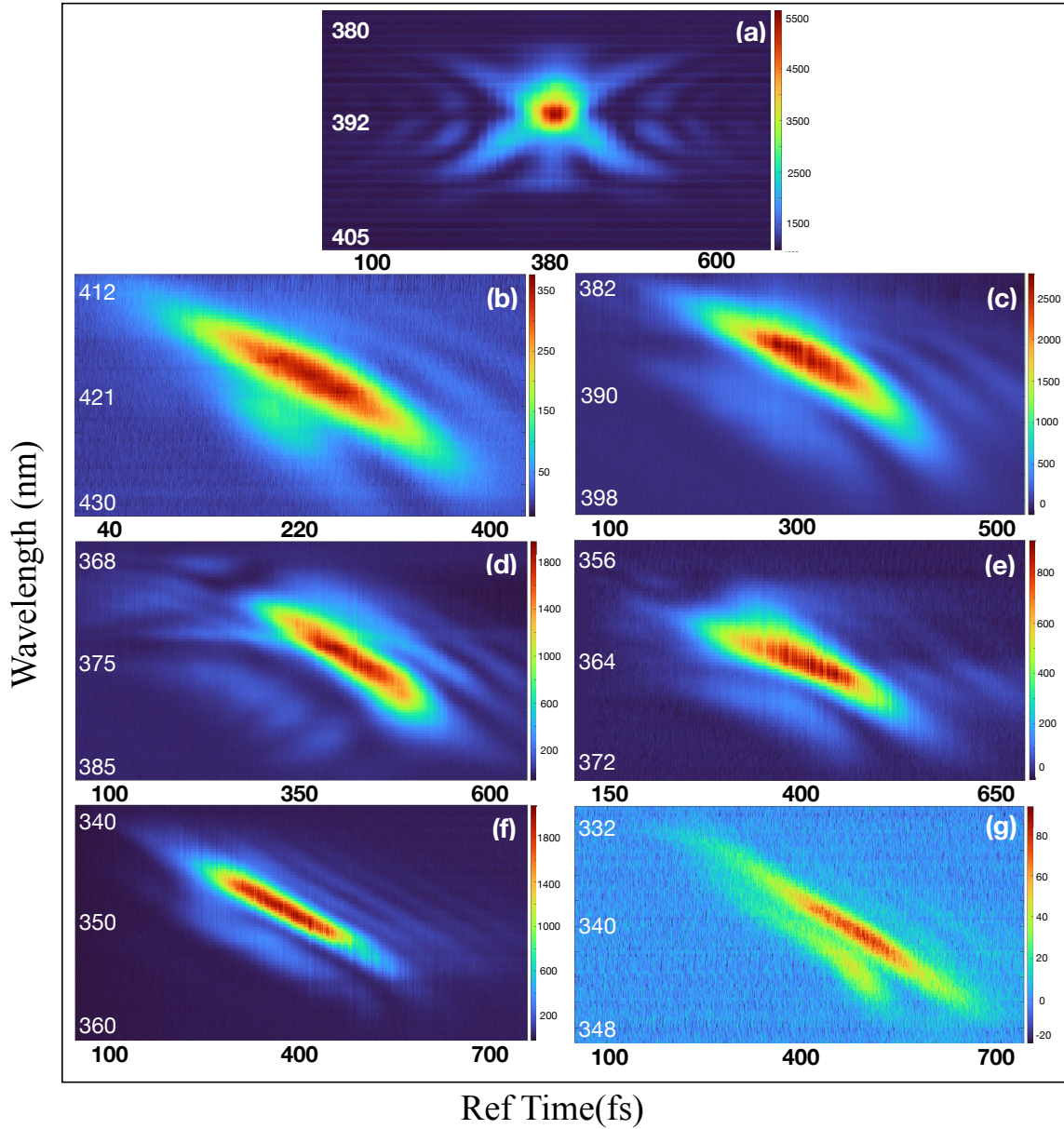


Figure 5.5: x-FROG spectrograms of each sideband taken after the 10-micron BBO crystal. The spectrogram for each beam (Ref, S1, AS1-5) is taken using the reference beam as the strong known pulse. (a) SHG-FROG trace of the reference pulse, (b-g) x-FROG traces of the S1-AS5 beams. The spectrogram distortions show a similar dispersion for all the sidebands, which is consistent with the GDD of the Semrock DC mirror. All the measurements are taken with respect to the time delay of the reference pulse. The similarity of the traces indicates that each beam is a Raman-shifted copy of the original beam with a slight difference in the distortion due to the dispersion added up from each DC mirror (DC 1-4 illustrated in figure 5.1).

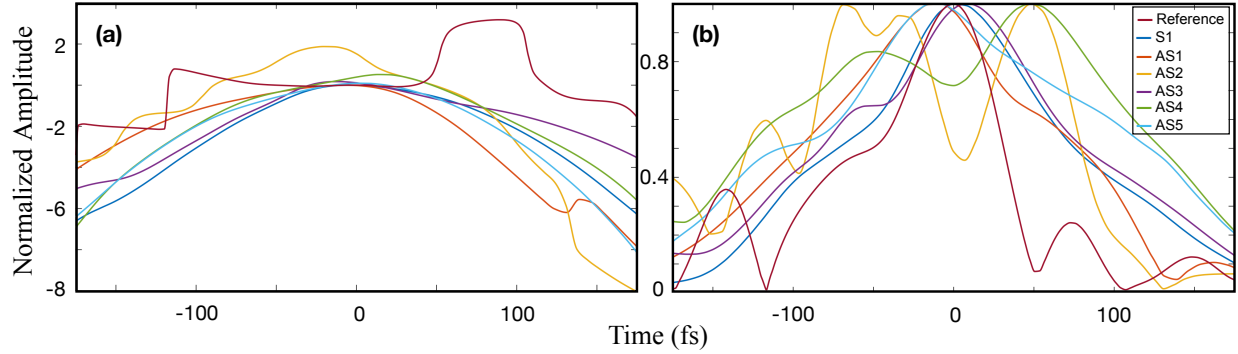


Figure 5.6: (a) Retrieved pulse phase, and (b) retrieved pulse envelope for all coherent Raman sidebands. Although the asymmetry in these curves is more visible compared to the curves in section 4.3 (due to the GDD of the Semrock DC mirror), each sideband was retrieved with less than 2% RMS error.

significantly. Our setup enables both coarse and fine-tuning of the spectral phases between the mutually coherent Raman sidebands by utilizing several manual and electric translation stages. The fine-tuning of these stages needs to be as precise as  $\sim 200$  nm for the highest order added ASs (i.e. AS4, AS5) corresponding to  $\phi = \pi/2 = \lambda/2$ . This precise adjustment is extremely important since, for example, in figure 4.3 (c,f) we can see that the slightest changes in the phase of AS2 result in a drastic change in the group delay of the final synthesized pulse.

The relative phase of the sidebands is adjustable by observing the coherent beating between the SFG signals of  $AS_n$  and  $AS_{n+2}$  and the SHG signal of  $AS_{n+1}$ . For example, in figure 5.8, we measure the beating between the SFG signal of the reference pulse ( $AS_0$ ) and  $AS_2$  with the SHG of  $AS_1$ . Theoretically,  $I_{(\text{SHG of } AS_2)} \propto \cos(2\phi_2 - \phi_1 - \phi_3)$ , where  $\phi_n$  corresponds to the spectral phase of the  $AS_n$ .

Figure 5.8 illustrates the theoretical and experimental beating interferograms between the non-linear signals (SHG and SFG) of several trios of sidebands. These interferograms are taken to verify that all the sidebands are in phase, meaning that the beams are spatially and collinearly aligned with high precision but are roughly aligned in the time domain, and the condition for the synthesis of a near-single-cycle pulse is mathematically met. The electric field of the pulse train

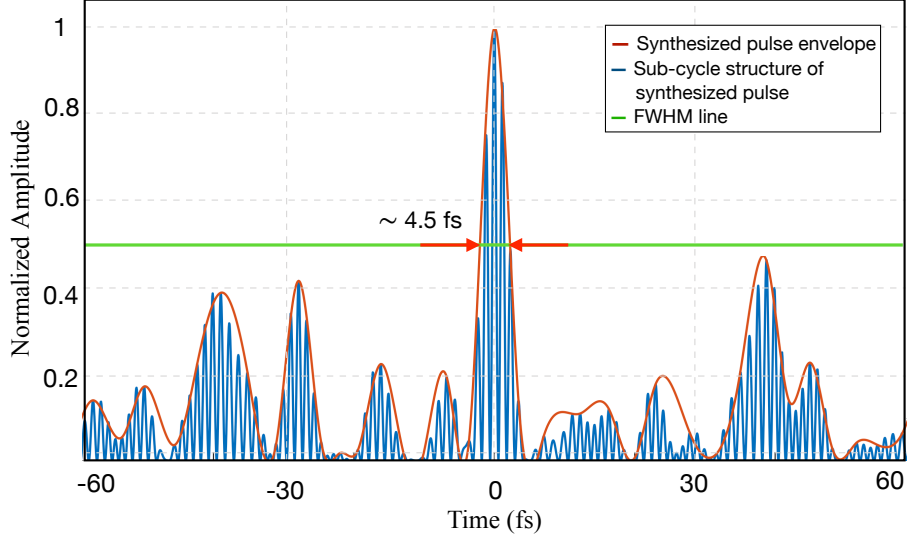


Figure 5.7: Synthesized pulse produced from the linear combination of 7 coherent Raman sidebands (A, ref, AS1-5). The pulse duration at the FWHM is around 4.5 fs.

synthesized from the sidebands can be written as [125]:

$$E(t) = \sum_n E_n(t) = \sum_n A_n(t) \cos(\omega_n t + \phi_n), \quad (5.1)$$

where  $n$  represents the order of the sidebands;  $n = -1$  is the Stokes beam,  $n = 0$  is the reference beam, and  $n = 1, 2, \dots$  represent AS1, AS2, ....  $A_n(t)$ ,  $\omega_n$ , and  $\phi_n$  are the time-dependent envelope function, carrier frequency, and retrieved spectral phase of  $n$ th sideband, respectively.  $\omega_n = n\omega_m$ , where  $\omega_m$  is the modulation frequency. For sidebands generated by molecular modulation, the phase relationship  $\phi_n = \phi_{CEP} + n\phi_m$  is always satisfied; hence, the field can be rewritten as  $E(t) = \sum_n A_n(t) \cos[n\omega_m(t + \phi_n/\omega_m) + \phi_{CEP}]$  which represents the narrowest envelope. Here,  $\phi_{CEP}$  and  $\phi_m$  are determined only by the initial spectral phases of the two input beams, i.e. pump and Stokes.

Here, one should note that we are not using any active CEP stabilization techniques, however, since the OPA is pumped and seeded by the pump laser, in principle it may be possible to CEP stabilize it when a CEP stable pump laser is used. Moreover, our scheme allows, in principle, f-2f-like CEP

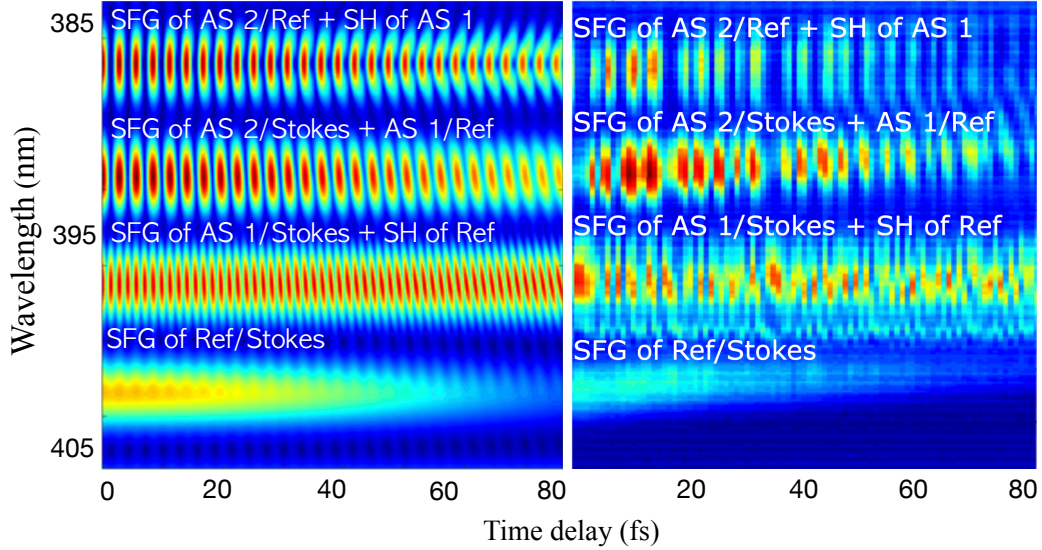


Figure 5.8: Comparison of the theoretical and experimental interferograms of different combinations of the nonlinear signals (SHGs and SFGs) of the sidebands covering the frequencies from S1 to AS2. Left: simulated interferogram obtained by a linear interference of the SHGs and SFGs of four chirped Gaussian pulses in the time domain. Right: experimental interferograms of the SHG and SFGs of the same pulses whose spectra are shown in figure 5.4. While all four experimental interferograms resemble their theoretical simulated counterparts, there are period differences between them which get worse by adding more nonlinear pulses (SHGs and SFGs of the main sidebands) to the combination. The distortion in the beats can be due to the extra dispersion that the DC mirrors and the BBO crystal bring to the equation, which is not considered in the theoretical simulation, but there is no solid explanation for the temporal mismatch, and it is yet to be explored.

measurement (and hence stabilization) whereby the second harmonic of the Stokes pulse interferes with one of the anti-Stokes sidebands. One may argue that if the OPA is seeded by the pump, the CEP should be preserved, however, this is true if the pump itself is CEP stabilized, which is not the case in our experiment. The OPA being seeded by the pump keeps the relative phase of the pump and Stokes constant, but the CEP changes shot-to-shot. We have discussed this in length in 4.3 and explained why our results are decoupled from the CEP stabilization of the original pulses.

Figure 5.9 shows a series of beat note interferograms that are taken after a 10-micron BBO crystal for several trios of the nonlinear signals of the sidebands. These interferograms were taken while the reference beam was aligned using Semrock DC. The DC of the last sideband (AS5) was fil-

tering the fundamental beams from their nonlinear signals, hence, AS5's nonlinear signals are not contributing to this series and the trace which includes AS5 appears faded at around 350 nm. The three first beat note traces from the top (355 nm - 390 nm) are slightly out of phase. We can correct this problem by first adjusting the phase of AS4, and then adjusting the phases of AS3 and AS2, respectively. Here, the thinner BBO (1 micron) is used instead of the 1mm BBO to avoid unwanted phase mismatching problems.

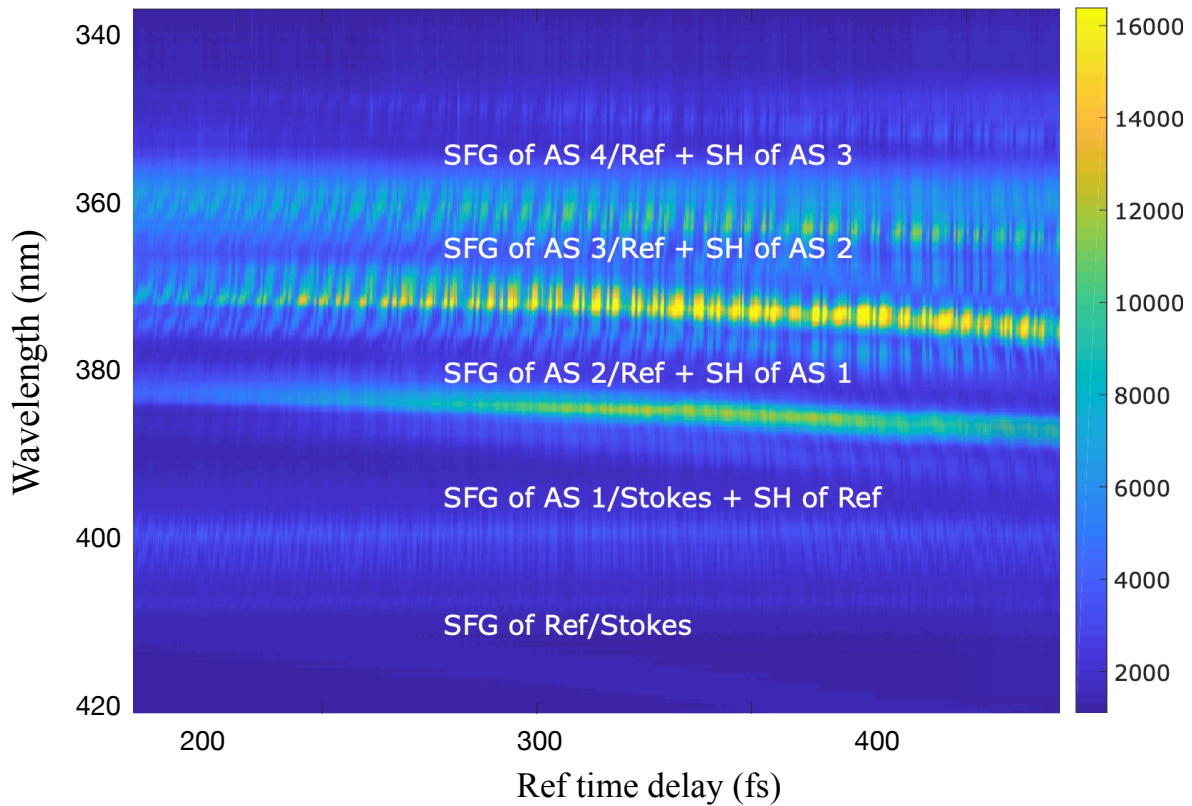


Figure 5.9: Time resolved interferograms of the nonlinear signals (SHG and SFG) of the 6 sidebands (S1, Ref, AS1-4). AS5 is excluded from these interferograms since DC5 is used to eliminate the strong fundamental signals of the other 6 beams. These beat note interferograms are taken after a  $10\ \mu\text{m}$  BBO crystal to avoid unwanted phase mismatching that is present while using the thicker BBO (1 mm). Here, the three middle interferograms (350 nm-390 nm) are slightly out-of-phase with each other, which can be corrected by changing the spectral phases of AS4, AS3, and AS2, respectively. Since this adjustment corresponds to a couple of hundred of nm, fine-tuning is required.

For more clear interferograms, unlike figures 5.9 and 5.10 that many sidebands are involved in each beat note trace, we only interfere trios of sidebands at each time chosen based on their well-defined relative phases.

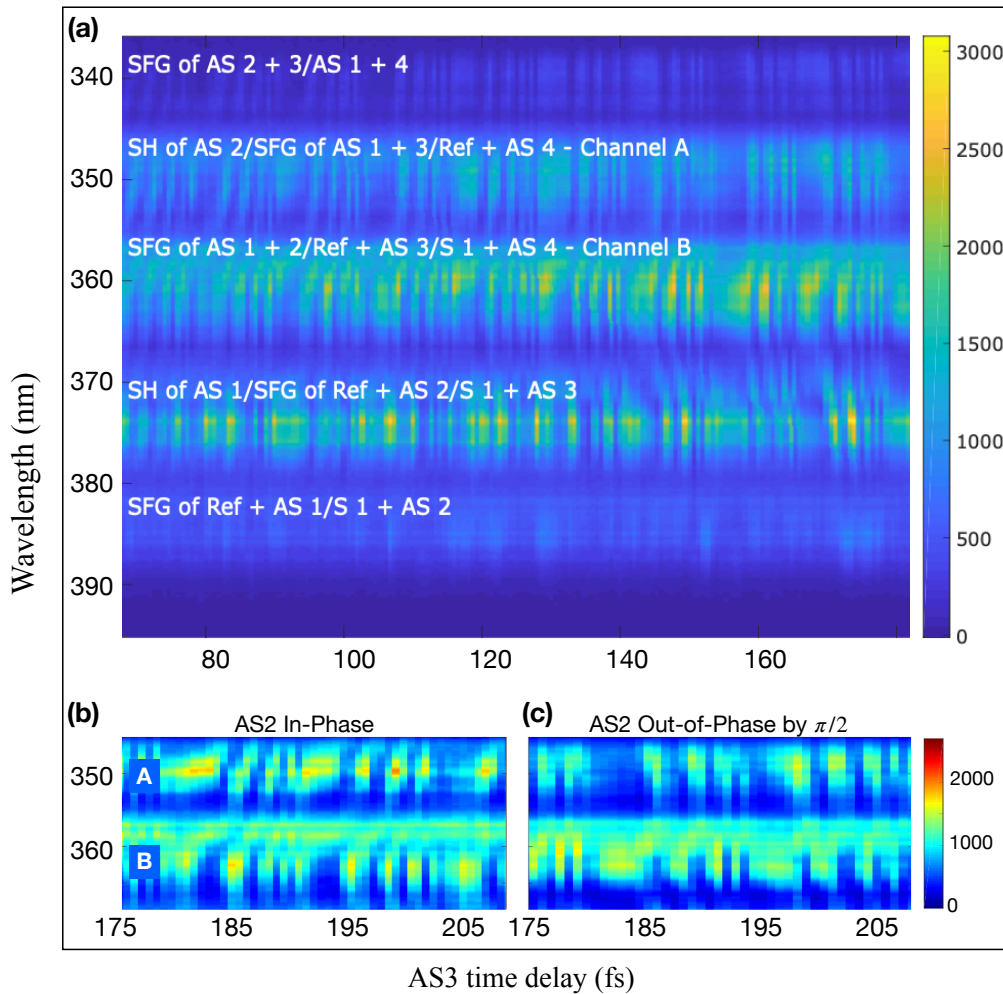


Figure 5.10: (a) Time-resolved interferograms of 6 beams (S1, Ref, AS1-4). Here, instead of using the DC mirror of AS5 to separate the fundamentals from their nonlinear signals, two UV filters (Thorlabs FGB25, Thorlabs FGUV11) are used. These beat note interferograms are taken after a 10  $\mu\text{m}$  BBO crystal to avoid unwanted phase mismatching. (b,c) Close-up views of channels A and B, while AS2 is in-phase and out-of-phase by  $\pi/2$  with the rest of the sidebands, respectively. AS2 participates as an SHG in channel A and as an SFG in channel B resulting in the channels being shifted. Hence, AS 2's phase is doubled for Channel A in relation to Channel B and results in the channels being shifted with respect to each other. This demonstrates the importance of fine phase adjustments in our synthesis setup.

This relative phase is resulted from the equally separated frequencies between the three sidebands. All four interferograms are taken in the 1mm BBO for the advantage of more defined traces due to a larger signal-to-noise ratio compared with the thinner BBO.

From the beat note analysis, we observe 1-2 fs beats corresponding to 16 fs in the group delay change in the synthesized pulse. However, this result do not constitute a direct measurement of this 16 fs group delay as reported by Zhi et. al. [121].

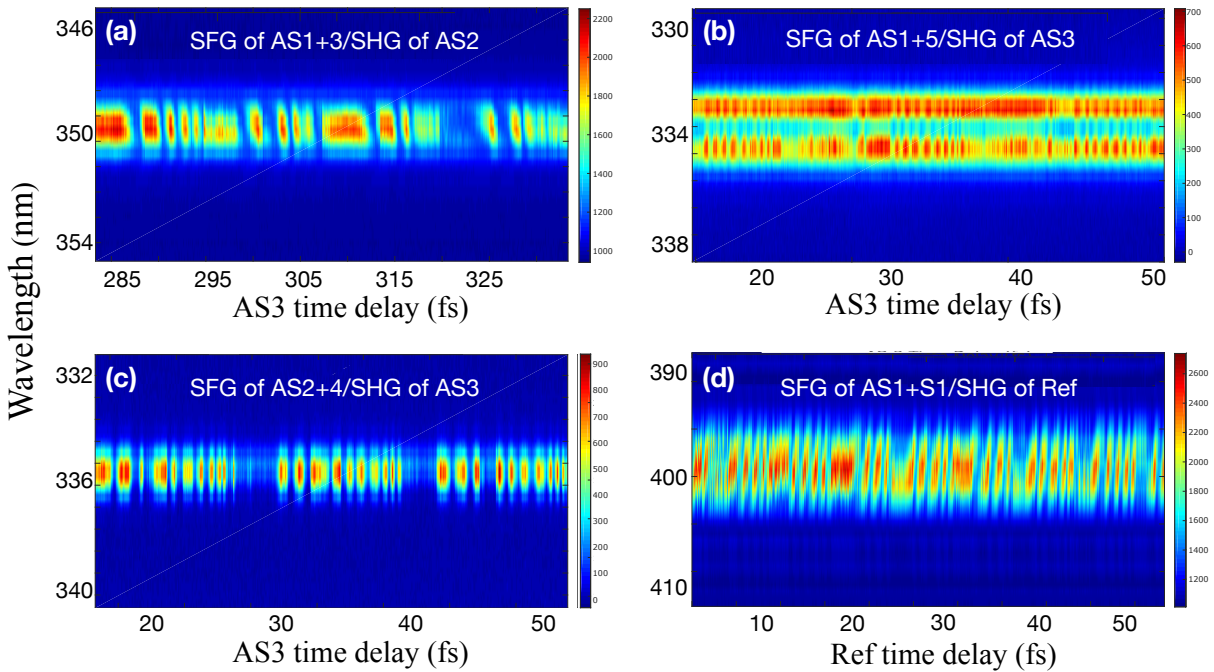


Figure 5.11: Four interferograms resulted from different interference between the nonlinear signals. (a) Beat notes generated by interference between the SHG signal of AS2 and the SFG signal of the AS1 and AS3, (b) interference between the SHG signal of AS3 and the SFG signal of the AS1 and AS5, (c) interference between the SHG signal of AS3 and the SFG signal of the AS2 and AS4, while fine-tuning the AS2's delay stage. (d) Beat notes generated by interference between the SHG signal of Ref and the SFG signal of the AS1 and Stokes beam while fine-tuning the Ref's delay stage. These trios are chosen based on their well-defined relative phases, which is resulted from their equally separated frequencies. All four interferograms are taken in the 1mm BBO for more defined results. We obtain the same results from the 1-micron BBO; however, the traces are less clear due to the lower signal-to-noise ratio. In all four cases, the beats follow a very similar pattern, but the periods of both the fringes and sections of incoherence are different.

Figure 5.11 shows four different combinations of the trios of sidebands. Our observations show that in all four cases, the beats are periodically chirped. Moreover, for example in (a), the beats appear and disappear with a period that roughly equals to  $T_{32} = 2\omega_3 - 2\omega_2$ . A key observation here is that the  $T_{32}$  stays the same no matter which BBO we use.

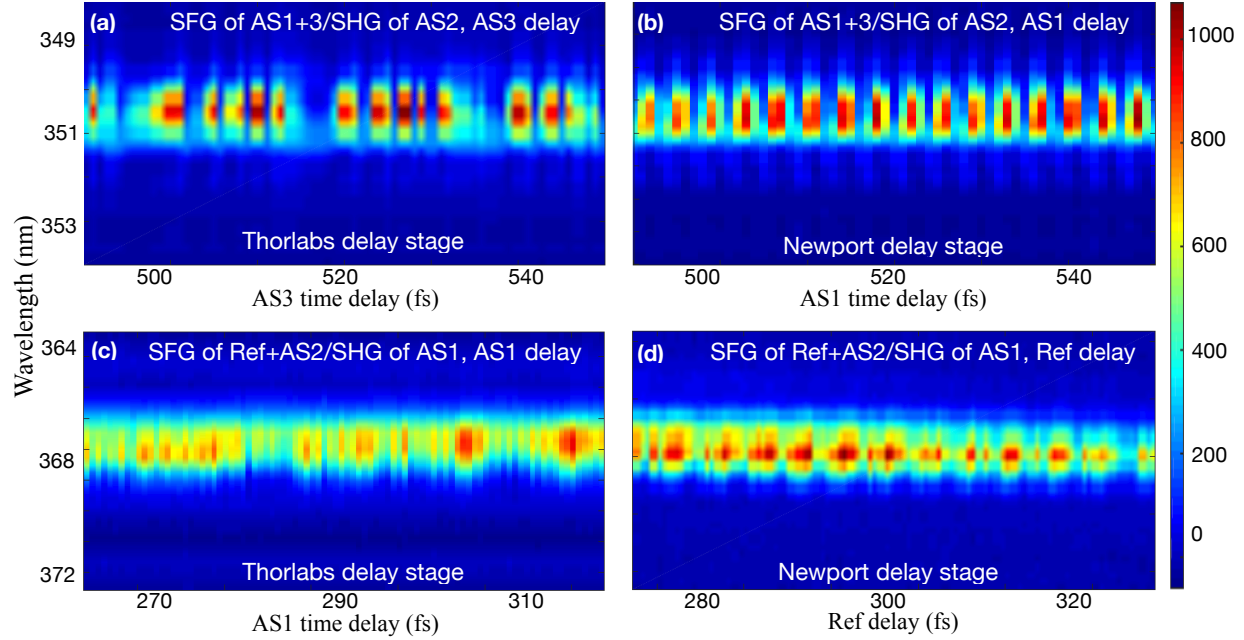


Figure 5.12: (a,b) Interferograms of the SFG of AS1 + AS3 with SHG of AS2 while tuning (a) AS3's delay stage and (b) AS1's delay stage in 1 mm BBO at the same time resolution. (c,d) Interferograms of the SFG of Ref + AS2 with SHG of AS1 while tuning AS1's and delay stage and (b) Ref's delay stage in 1 mm BBO at the same time resolution.

Another important point is that depending on which sideband we are scanning over by tuning its delay stage, the beats contain different frequency components. Such frequencies that we first assumed as the noise coming from the translation stage of AS1 with a resolution of 200 nm corresponding to 0.667 fs disappear for the AS1+AS3/AS2 measurement. But for the combination of Ref+AS2/AS1, the disappearing frequency component happens by moving AS1's stage but does not happen when moving the Ref's stage, which is the same model as AS1's stage (figure 5.12). We guess this happens due to the cross-phase modulation between  $\omega_1 + \omega_3$  and  $\omega_2$ .

Another valid concern while having all the sidebands' SHG after BBO in phase is if the fundamentals are in phase as well. In our setup, assuming perfect phase-matching in the BBO crystal, the SHG of each beam is in phase with its fundamental meaning that by passing through the BBO, the SHG signals do not gain an extra phase. This has been proven in detail [127] and experimentally shown by Kress et al. and Cook et al., separately [128, 129].

## **5.5 conclusion**

We have demonstrated the construction of a 4.5 fs pulse using 5 coherent anti-Stokes Raman sidebands generated in single-crystal diamond in conjugation with the original reference and Stokes pulses. We analyze all the sidebands separately using a combination of XFROG and interferometric techniques called ix-FROG. Our experiment is scalable by adding more sidebands to the collinear combination by improving the overall power of the sidebands exiting the crystal. Our beat note analysis shows the crucial role of fine-tuning the relative phases of the sidebands. The next step is to characterize the resultant pulse through multiphoton ionization in low-density xenon gas. The methods and the preliminary results are discussed in the following chapter.

## 6. MULTI-PHOTON IONIZATION IN XENON USING SYNTHESIZED NEAR SINGLE-CYCLE PULSES GENERATED IN RAMAN INTERACTION

### 6.1 Introduction

As the continuation of the previous work in chapters 4 and 5, we perform a multi-photon ionization experiment in low-density xenon (Xe) gas to characterize our synthesized pulses fully described in previous chapters. We perform this experiment using a collinear combination of a selected subset of mutually coherent Raman sidebands generated in diamond. It has been shown that the peak ion signal is reversely proportional to the ionizing pulse length [32]. Our ultimate goal is to add as many sidebands to the collinear combination in order to have a shorter and shorter synthesized pulse, and therefore, have a strong ion peak in the time-of-flight (TOF) mass spectroscopy spectrum. However, the energy of our Raman sidebands is a significant drawback in this experiment. Since the construction of a Fourier transform limited (FTL) relies on the fact that all sidebands have the same energy, the final pulse energy is only scalable to the energy of the highest-order sideband added to the combination. To have a relatively strong pulse for the ionization purpose, the highest-order sideband that we added in the following experiment is AS2. Table 6.1 presents the measured wavelength and the power for each Raman sideband before entering the Xe-filled pressure-controlled vacuum chamber. Depending on the range of the measurement, two different power meters are used; the first one is Coherent FieldMax II which measures the power of the reference beam and the Stokes beam when a PM10 head and a PS 10 head are connected to it, respectively. For the weaker sidebands (AS1 and AS2), the power is measured using an Ophir Vega meter connected to a PD10-pj-C head.

To perform this experiment, we had to tackle the two major problems that we were facing:

1. vacuum chamber leakage,
2. sidebands' temporal/spatial overlap.

The latter was tricky to achieve using the usual BBO-overlap method used in the previous two

Table 6.1: The measured power and wavelength of each sideband (Ref, Stokes, AS1,2) before entering the pressure-controlled vacuum chamber.

Sideband order	Wavelength (nm)	Power before Chamber (mW)
Ref	800	62
Stokes	870	0.35
AS1	750	0.15
AS2	700	0.027

chapters. I will expand on these problems and discuss our solutions to each of them in the two following sections.

## 6.2 Vacuum Chamber Preparation

In order to perform the xenon ionization at proper pressure, a reliable vacuum chamber is needed. The full description of the vacuum chamber parts is presented in table 6.2. We noticed that the chamber had signs of leakage that we had to address before starting the experiment.

Table 6.2: The part numbers and descriptions of the vacuum system. All the vacuum parts are from Pfeiffer Vacuum systems and all the pump parts are from Kurt J. Lesker. Manuals are available upon request. OD and ID stand for outer and inner diameters, respectively. P stands for pressure.

Vacuum Chamber Part	Part Number	Part Description
Vacuum body	C-0275	2 – 3/4" flange, 4-way CF cross
Main turbo pump	TMU 071 P	$1 \times 10^8$ mbar minimum pressure
Backing Diaphragm pump	MVP 035	1 mbar minimum pressure
Vacuum gauge	PKR 251	Pirani (high-P) and cold cathode (low-P)
Angel valve	VAT 284	on/off valve connected to the gas chamber
Copper gaskets	GA-0275LB	2 – 3/4" flange, 1.895" OD, 1.528" ID
Sapphire windows	VPZL-275S	2 – 3/4" flange

There are several ways to examine the leakage from the vacuum body or the windows:

- Methane/acetone detection.

- Diluted soap detection.
- Helium detection.

For the first two methods, we filled the chamber with dry nitrogen slightly above the atmospheric pressure. The first method exploits the change of the pressure due to methane or acetone evaporation; we cover all the joints of the vacuum chamber with methane or acetone and instantly use a hair dryer to dry it. If there is a hole in any of the joints, methane or acetone would get sucked in that and freeze and we expect to see a drastic change in the pressure read-out. However, we were not able to detect the leak using this method. Then we went ahead and used a foaming soap to cover the joints while the vacuum was full of dry nitrogen. We were looking for any bubbling to come out of the possible hole. Unfortunately, we did not detect any leakage. The next step was to try helium detection. A helium leak detector, also known as a Mass Spectrometer Leak Detector (MSLD), is used to locate and measure the size of leaks into or out of a system or containing device. In this method, the vacuum is pressurized with helium gas or a mixture of helium gas and air. The potential leakages then are scanned using a sniffer probe connected to the inlet of the leak detector. This detector was not available to us at the time of the experiment. We needed to schedule an appointment with an expert at the cyclotron institute at Texas A&M which might have taken us a week, so we decided to give the soap method another chance by using a different non-foaming liquid hand soap diluted in water. This time we carefully covered all the joints as well as the sapphire windows. We finally detected a small leakage on one of the sapphire windows which we missed the first time (we did not cover the windows the first time). We, finally, resolved the problem by purchasing a new sapphire window, and we were able to achieve a pressure as low as  $1.1 \times 10^{-8}$  mbar and maintain the pressure of  $1.4 \times 10^{-7}$  mbar after several hours of stopping the pump.

Every time that each of these detection methods is used, the whole chamber needs to be baked down and then cooled down to room temperature. This is done to eliminate the trapped air molecules and other potential impurities in the microscopic holes of the aluminum of the vacuum chamber's body. Afterward, we run the vacuum pump for several hours to reach the lowest

possible pressure, and then, we close the valve that is located between the pump and the vacuum chamber. We wait for about two hours to see how the pressure raises and if the increase in the pressure is too drastic, we conclude that there is a leak in the vacuum system. For baking the vacuum, we wrap all the metal parts with an electric heating tape (AWH-101-060DC- MP, HTS/Amptek). We then cover the whole taped area with aluminum foil to act as a heat shield. The baking process needs to be done very slowly by increasing the voltage connected to the electric heating tape. The reason is that a large heat gradient can damage the sapphire windows and can cause loosening in the flange's bolts and nuts. We increase the voltage from 0 to 60 V by 1 V and wait for about 5 minutes before the next increment. We use a variable transformer (Staco, 3PN 1010) to perform this task. After we reached our desired temperature which is around 150 °C we leave the pump running for a day or two and bake the vacuum system. After the baking is over, we reduce the temperature following the exact opposite procedure (lowering the voltage gradually).

Figure 6.1 (a) shows the vacuum chamber we used for this experiment. The electric heating tape wrapped around it that we used for the baking process can be seen in this photo. Figure 6.1 (b) shows the order of the tightening for the bolts. The order is very important to avoid an uneven seal which results in leakage. The tightening process is as follows:

1. Using a drive-click torque wrench on a lower setting to go around the flange from bolt number 1 to bolt number 6 (for example if the proper final torque recommended by the company is 20 in-lb, we start from 5 in-lb),
2. using a feeler gauge, covered with a lubricant, to go around and examine the gaps and make sure that the same feeler blade with a specific thickness fills all the gaps equally,
3. if one of the gaps is bigger, we slightly tighten the two bolts next to it and repeat the whole process from 1, if not, we continue,
4. increasing the setting on the torque wrench by 2-5 in-lb at the time and repeating from 1 until we reach the final setting of the 20 in-lb which is recommended by the company for this specific flange.

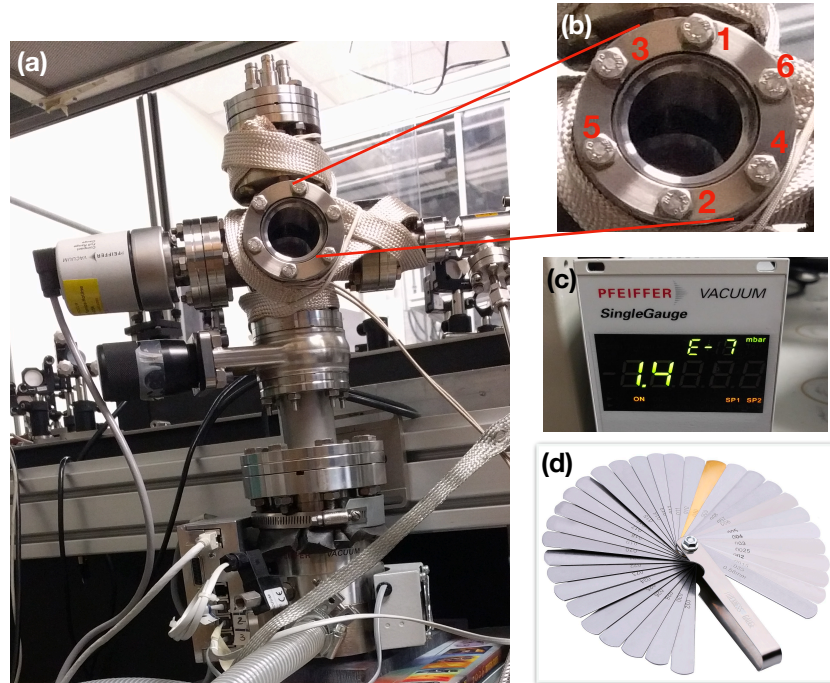


Figure 6.1: (a) Vacuum chamber used for the Xe ionization experiment. (b) The bolt tightening technique for the best sealing results. The order of the numbers shows the order of the tightening at each round. After a full round of tightening is completed, the gap between the two flanges is examined by a feeler gauge to assure the same size gap all around the flange. This procedure is continued until one of the thinner feeler gauge blades (depending on the torque) can fit all the gaps, equally. (c) The pressure inside the chamber as read by the Pfeiffer SingleGauge which goes as low as  $10^{-7}$  mbar. (d) The feeler gauge that was used to examine the gaps between the two flanges. Lubricant is used on the blades for an easier process.

We possibly can do this process using a regular wrench, however, a drive-click torque wrench eliminates guessing work and the risk of over-tightening the bolts causing the copper gasket deformation and uneven seal. We change the vacuum copper gasket every time that we need to open and close the chamber because after the pump runs, the suction in the seal causes deformation in the gasket.

### 6.3 Beams overlap potential solution

In the previous experiments described in chapters 4 and 5, the sidebands' temporal and spatial overlap was achieved by the detection of the SFG signal generated by each couple of the sidebands in the BBO crystal. However, while performing the xenon ionization experiment, the air is a better medium compared to a solid crystal such as a BBO to replicate the phase-matching condition in the low-pressure xenon in the vacuum chamber. Moreover, the previous alignment was disrupted when we removed the ND filters that were used for the Stokes, AS1, and AS2 beams in the previous experiment. Therefore, we exploit a method suggested by Peter Zhokhov and Ilya Fedotov called "plasma overlap". In this method, by observing the diffraction patterns generated by each collinear beam after interacting with the plasma that is generated from the strong reference beam, we can indicate whether the beams are temporally and spatially overlapping. If the diffraction patterns are produced, it means that the beams are spatially overlapping, and the beams are temporally overlapping at the moment of the plasma formation when is at the peak of the pulse. To ease the inspection of the diffraction patterns, we used a notch filter (Semrock NF03-808E) after the plasma to remove the strong reference beam.

## 6.4 Experimental Setup

### 6.4.1 Main Setup Description

Figure 6.2 shows the experimental setup used for this study. The first part of the setup until the collinear recombination is fully described in section 4.2 except for the ND filters that are removed from the paths of St, AS1, and AS2. After the collinear recombination, the FTL pulse generated from the four sidebands, Ref, St, AS1, and AS2, spanning over 100 nm, is guided into a vacuum chamber filled with low-pressure ( $\sim 1 \times 10^{-6}$  mbar) xenon gas (Matheson). To reach this exact pressure, we first filled the vacuum with the Xe gas at atmospheric pressure and then pumped the vacuum out until we reached  $\sim 1 \times 10^{-6}$  mbar. Unfortunately, this method is not very reliable and repeatable, hence, one would benefit from investing in a leak valve.

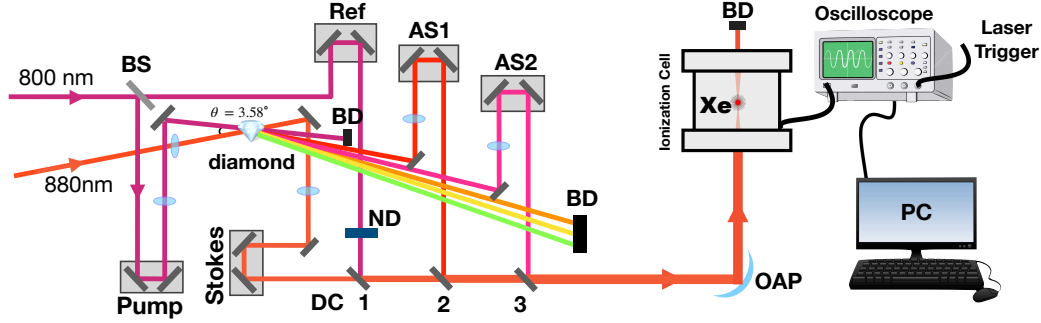


Figure 6.2: Experimental setup used for phase-controlled multi-photon ionization in xenon in a pressure-controlled ( $\sim 10^{-7}$  mbar) vacuum chamber. A neutral-density mirror is used to decrease the intensity of the reference pulse. To focus the beams in the chamber, an off-axis paraboloid is used instead of a lens or an achromatic doublet to minimize dispersion. Abbreviations for the experimental elements: AS 1 and 2, anti-Stokes 1 and 2, BS, 50/50 beam splitter, ND, neutral density filter, DC 1-3, dichroic mirror 1-3, OAP, off-axis paraboloid.

We loosely focus the synthesized pulse into the Xe gas chamber using an off-axis paraboloid (OAP-Newport 50332AL) which is placed outside the chamber right before the sapphire window. The St, AS1, and AS2 beams were set to their maximum power but the Ref beam was attenuated by sets of ND filters until an ionization signal was detectable ( $62 \mu\text{J}$  over 100 fs which corresponds to a peak power of 620 MW). After focusing the reference to  $\sim 100 \mu\text{m}$  radius of spot size, the peak power reached  $1.9 \times 10^{16} \text{ W/m}^2$ . However, since the measured signal was very weak we concluded that the dispersion coming from the window might contribute negatively to the local focusing. We decided to substitute the OAP with a spherical mirror that had a very short focal length (1.25 cm), but this time, placing the mirror inside the chamber that resulted in a slightly stronger signal.

## 6.4.2 Channeltron Description

Figure 6.3 shows the channeltron we use for ion detection. The channeltron is mounted on the top of the vacuum chamber with a ConFlat (CF) flange whose top view is shown in Figure 6.3 (a). As seen in this photo, there are four separate ports located at the top. Of these four ports, only three of them are useful and marked as SIG (signal), HV (high voltage), and GND (ground). We connect the SIG port to an oscilloscope (Tektronix - C3000) to read the signal and the HV port to

a high bias voltage source (Burle power supply -PF1056, 670  $\mu$ A). We also connect the GND port to the power supply's ground by running a wire between them and fixing the wire to the optical table. The channeltron operates at a high voltage of 1.5-3 kV, however, the recommendation is to use the lowest possible voltage to prevent the shortening of the lifetime of the channeltron. We use BNC (Bayonet Neill–Concelman) cables for all these connections.

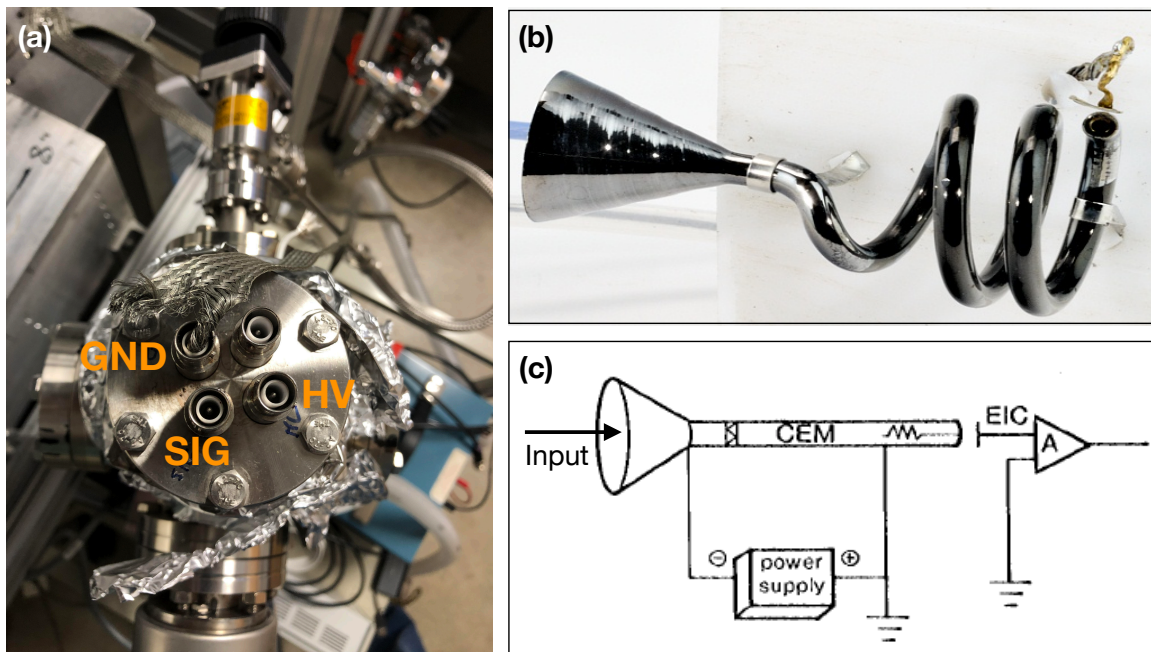


Figure 6.3: (a) Top view of the channeltron mounted on a CF flange. The channeltron collector is connected to the CF flange vertically with the ion collector head hanging down in the chamber. (b) A real image of a channeltron. (c) Schematic of a typical channeltron circuit for detecting positive ions. More detail is provided in the manual available upon request. Abbreviations for the elements: SIG, signal port, HV, high voltage port, GND, grounded port, CEM, channeltron electron multiplier, EIC, electrical isolated collector.

A sample signal obtained by the oscilloscope in our first measurement trial is shown in figure 6.4. This plot shows the signal in the presence (red curve) and absence (blue curve) of Xe gas.

To get a better signal-to-noise ratio we trigger the scope using the “SYNC OUT DELAY”

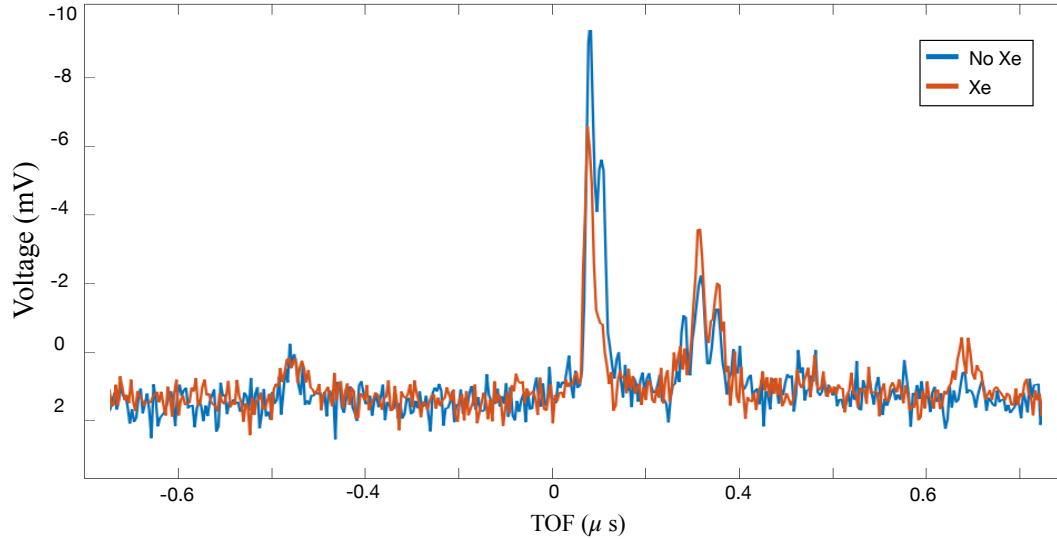


Figure 6.4: First trial of measuring the TOF from the mass spectroscopy recorded by the oscilloscope in the presence (red curve) and the absence (blue curve) of low-pressure Xe in the vacuum chamber.

output of the Coherent Synchronization and Delay Generator (SDG) box, therefore, we can use the highest resolution scope settings on the oscilloscope.

## 6.5 Results

Figures 6.5 and 6.6 summarize our findings from the multi-photon ionization in Xe gas using our tailored FTL pulse generated from synthesizing a subset of mutually coherent Raman sidebands generated in a single-crystal diamond. In the spectra taken from the channeltron, we expect to observe an enhancement in the ionization signal when all the sidebands are in phase, and suppression when one of the bands (here Ref) is out of phase with the rest of the sidebands [130]. Figure 6.5 (a) shows the TOF as a function for the reference beam. The top trace (blue) appearance is caused by the impurities in the vacuum chamber and the lower trace (green) is measured from xenon gas. To obtain this spectrogram, we first set all the beams (Ref, St, AS1, and AS2) in phase, using the method described in section 6.3. Then we scan over the Ref beam's time delay by varying the position of its translation stage and record the data. As seen in this spectrogram,

the Xe peak is clearly visible around 275 ns. However, varying the Ref's delay does not have any effect on the signal unlike what we expected. We believe that this abnormal behavior is due to the way that we synthesize our pulse from the four sidebands. In order to correctly generate an FTL pulse by combining Raman sidebands, all the beams need to have roughly the same power which is not the case in this experiment. In the second trial, we performed the same measurement by only using the reference pulse with no sidebands added. The resultant spectrogram is shown in figure 6.5 (b).

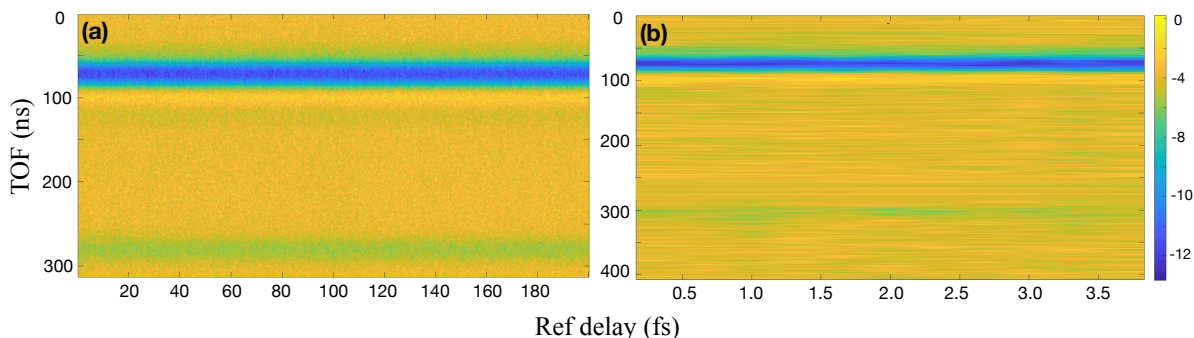


Figure 6.5: TOF Spectrograms measured by an oscilloscope of the photonized species detected in Xe gas using the FTL pulse generated from (a) four coherent Raman sidebands: Ref, St, AS1, and AS2, and (b) only the Ref pulse. Both spectrograms are taken over the Ref's time delay. The blue trace is from the impurities in the vacuum chamber and the green trace is from Xe. The resolution in (b) is lowered to save measurement time.

Figure 6.6 shows the power dependence of the TOF on the power of the reference beam. These measurements are taken while the ionization was only from the Ref pulse. As seen in these plots, the two peaks at around  $0.1 \mu s$  and  $0.4 \mu s$  are due to the impurities in the vacuum system as we expected [130]. What we cannot explain is that the first peak, which attributes to carbon, has a much higher non-linear dependence on the power of the Ref pulse than the other two peaks. To further investigate, a much larger power range would be helpful.

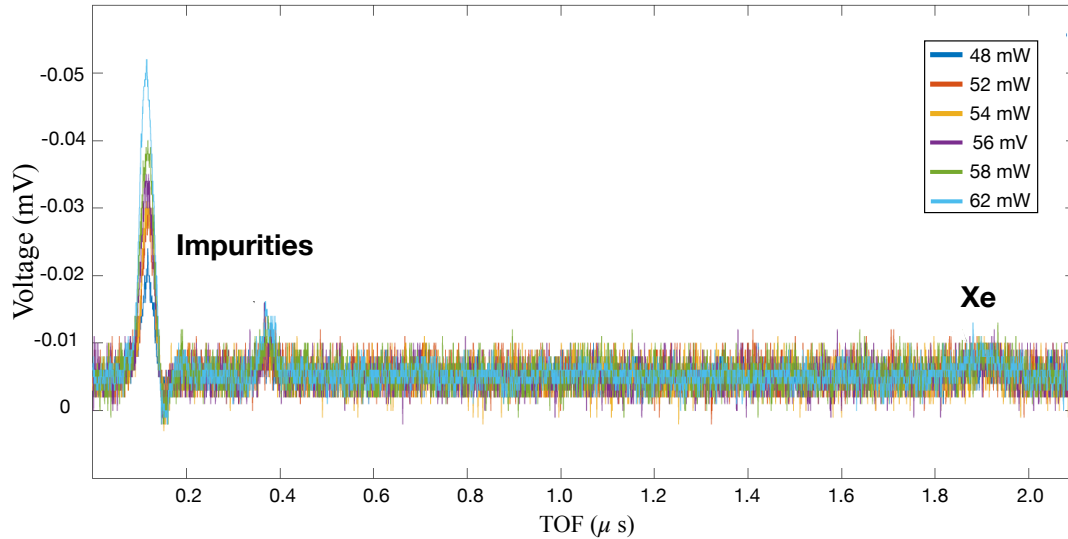


Figure 6.6: TOF spectra dependence of the photionized Xe gas on the Ref beam's power. These spectra are recorded while the ionization was only due to the plasma created by the Ref pulse with no sidebands added.

## 6.6 Conclusion

We were able to perform mass spectroscopy and measure the TOF from the Xe ionization using a synthesized pulse produced from four mutually coherent Raman sidebands generated in a single-crystal diamond. However, our results are limited to the low power of these sidebands, and hence, we were not able to investigate the enhancement/suppression of the Xe peak resulting from the sidebands being in/out of phase with each other. This problem can be resolved by repeating this experiment using our new 8 mJ laser system (Astrella by Coherent Inc.) that can add an order of magnitude to the power available to the OPA (from 500  $\mu$ J to 5 mJ), however, building the setup from the scratch would be a very time-consuming task. Currently, Nathan Marshall is working on the existing setup to improve the results of this experiment.

## 7. PRESSURE CONTROLLED PHASE MATCHING IN KAGOMÉ PC FIBER IN PICOSECOND CARS<sup>†</sup>

### 7.1 Introduction

Flexibility in fiber design gives hollow-core photonic crystal fibers (HC-PCFs) interesting properties such as high non-linearity, tunable dispersion, and low loss which make them suitable for a variety of applications. The two main classes of HC-PCFs are photonic bandgap fibers (PBGs) and the class whose guidance is based on inhibited coupling. Research on the second class of fibers led to a microstructured fiber called Kagomé fiber. The cladding structure and negative curvature in such fibers inhibit the coupling between the fundamental modes of the cladding and the core [131].

Using Kagomé fiber in picosecond CARS experiment improves the efficiency of the four-wave mixing by providing a longer interaction length. Since four-wave mixing is highly phased sensitive (determined by the relative phase of the four beams), its effect can accumulate in longer distances [62]. Another interesting way to optimize phase matching is by controlling the transverse beam profile [31].

In this work, we calculate the group velocity dispersion (GVD) and the dispersion factor ( $D$ ) of a specific Kagomé fiber (PMC-C-RD-700/1500-7C/GLOphotonics) and compare the results with the experimental data which is provided by the factory. After ensuring that both results match in the desired region, we calculate the phase mismatching ( $\Delta k$ ) in Kagomé fiber for four gases as a function of pressure and Raman shift ( $\Delta\omega$ ).

### 7.2 Theoretical Framework

Group velocity dispersion and dispersion factor in a Kagome fiber can be calculated as follows:

---

<sup>†</sup>Reprinted with permission from “Pressure Controlled Phase Matching in Kagome PC Fiber in Picosecond CARS” by A. Bahari, Y. Shen, and A. V. Sokolov, 2019, *Frontiers in Optics + Laser Science APS/DLS, OSA Technical Digest (Optica Publishing Group)*, paper JTU3A.123. Copyright [2019] by A. Bahari.

$$GVD = \beta_2(\lambda) = \frac{\lambda^3}{2\pi c^2} \frac{d^2 n_{eff}}{d\lambda^2} \quad \text{and} \quad D = \frac{-2\pi c}{\lambda^2} \beta_2, \quad (7.1)$$

where  $c$  is the speed of light in vacuum. Effective refractive index ( $n_{eff}$ ) for Kagome fiber in fundamental mode ( $HE_{11}$ ) can be approximated as [132] :

$$n_{eff}(\lambda, P) = \sqrt{n_{gas}^2(\lambda) - \frac{u^2}{k^2 a^2}} \simeq 1 + \frac{P}{2P_0} \frac{T_0}{T} \left( \frac{A}{1 - (\frac{B}{\lambda})^2} + \frac{C}{1 - (\frac{D}{\lambda})^2} \right) - \frac{u^2 \lambda^2}{2\pi^2 d^2}, \quad (7.2)$$

where  $u = 2.405$  is the root of equation  $J_0(u)$  (zeroth order Bessel function) = 0 and  $a = d/2$  is the radius of the core ( $d = 49 \pm 1\mu m$ ). Table 1 shows the experimental values for constants A, B, C, and D for four gases [133]. Applying the phase matching condition in CARS:

$$\Delta k = k_{Stokes} + k_{signal} - 2k_{pump}, \quad (7.3)$$

and noting that  $\lambda_{pump} = 1064$  nm and  $\omega_{signal} + \omega_{Stokes} = 2\omega_{pump}$ , we can rewrite equation 7.2 with respect to  $\lambda_{Stokes}$  setting  $\lambda_{signal} = 532\lambda_{Stokes}/(\lambda_{Stokes} - 532)$ .

Finally, we can calculate and plot the phase mismatching as a function of pressure and  $\Delta\omega$  for four gases.

Table 7.1: Experimental values for constants A, B, C, and D for Argon, Krypton, Nitrogen, and air.

Gas	A	B (nm)	C	D (nm)
Ar	$2.033229 \times 10^{-4}$	14.36	$3.445831 \times 10^{-4}$	89.81
Kr	$2.610288 \times 10^{-4}$	1.418	$5.694682 \times 10^{-4}$	100.2
$N_2$	$3.920995 \times 10^{-4}$	33.85	$1.880648 \times 10^{-4}$	116.08
Air	$1.492644 \times 10^{-4}$	4.4	$4.1807 \times 10^{-4}$	86.22

### 7.3 Results and discussion

Figure 1 (b) shows the comparison between the experimental data and the calculated dispersion factor in an air-filled Kagome fiber. Although the cutoff wavelength is not the same for the two curves, in our desirable range for this particular CARS experiment (with pump wavelength at 1064 nm, Stokes wavelength from 1100 nm to 1700 nm, and the signal wavelength from 750 nm to 1000 nm) the two curves are matching well.

In conclusion, although our preliminary experimental results show a significant enhancement in CARS signal using just an air-filled Kagome fiber in the setup, our calculations indicate that by using Krypton (at around 20 bar) as the buffer gas in Kagome fiber, we can achieve a much higher signal enhancement.

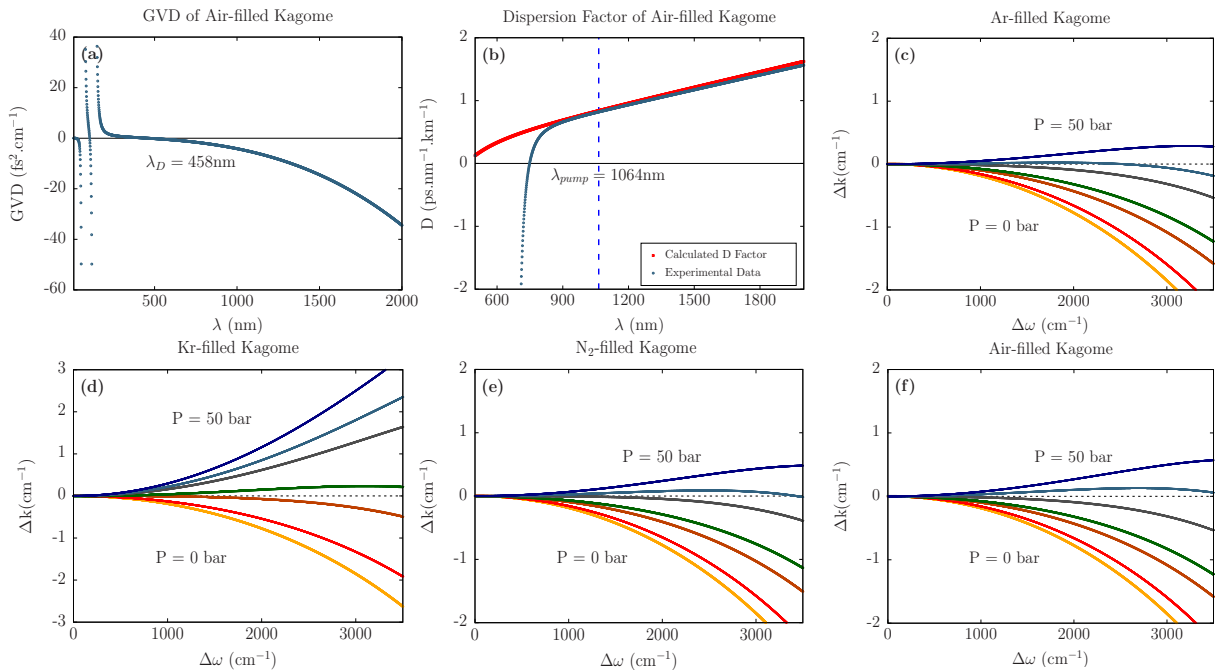


Figure 7.1: (a) Calculated GVD of air-filled Kagome fiber, (b) comparison of the experimental and calculated D factor of air-filled Kagome fiber, (c-f) phase mismatch factor as a function of Raman shift and pressure for Argon-, Krypton-, Nitrogen-, and air-filled Kagome fiber.

## 8. BACKGROUND-PENALTY-FREE WAVE-GUIDE ENHANCEMENT OF CARS SIGNAL IN AIR-FILLED ANTI-RESONANCE HOLLOW-CORE FIBER<sup>†</sup>

### 8.1 Introduction

Photonic crystal fibers (PCFs), also known as microstructured fibers, have a great variety of hole arrangements leading to different properties suitable for versatile applications [134]. Hollow-core PCFs (HC-PCF)s are a new class of PCFs in which light can be guided in the central hollow channel. These types of fibers are ideal candidates for many linear and non-linear optics studies due to their flexibility in design, high non-linearity, and tunable dispersion properties[135]. High harmonic generation, gas-based non-linear optics, and atom and particle guiding are only a few examples of the diverse applicability of HC-PCFs [136]. Aside from the design, the pressure inside their hollow core is a parameter that can be tuned to manipulate the dispersion and achieve better phase matching critical to four-wave mixing (FWM) processes such as coherent anti-Stokes Raman scattering (CARS) [137]. Moreover, due to the HC-PCF's optical confinement and low transmission loss, the distance with constant laser intensity is greatly increased compared to focused laser beams, without the need for optical cavities [138, 139]. The CARS spectroscopy in multi-mode fibers and double-clad fibers has been studied in the past [140, 141]. For example, a specific double-clad HC-PCF has been used in the CARS experiments to reduce the inherent coherent Raman noise that is generated in the optical fibers [141]. Anti-resonance hollow-core fiber (AR-HCF) with a leaky mode nature is a type of fiber that offers even more advantages over conventional PCFs and HC-PCFs. AR-HCFs with the negative curvature of the core-cladding interface, which reduces the optical losses, were first proposed in the Fiber Optics Research Center of the Russian Academy of Sciences (FORC RAS) in 2011 [142]. It is important to realize that the cladding of AR-HCFs is not structured as a crystal, so, they are not classified as PCF. The op-

---

<sup>†</sup>Reprinted with permission from “Background-penalty-free Waveguide Enhancement of CARS Signal in Air-filled Anti-resonance Hollow-core Fiber” by A. Bahari, K. Sower, K. Wang, Z. Han, J. Florence, Y. Wang, S. Gao, H. W. Lee, M. O. Scully, A. M. Zheltikov, and A. V. Sokolov, 2022, *Opt. Lett.*, vol. 47, p. 4339-4342. Copyright [2022] by A. Bahari.

tical properties of this class of fibers are defined only by the reflection of light on the elements of the core-cladding interface. AR-HCF has gained tremendous attention in the fiber optics community due to its low loss properties as well as the moderate cladding fabrication efforts necessary, as compared to many different HC-PCFs [136, 143, 144]. The broadband single-mode operation, high power pulse delivery, and high damage threshold are some of the many advantages of these types of fibers. By decreasing the coupling between particular waveguide modes in AR-HCF, the anti-resonance phenomenon can significantly reduce optical loss and hence, improve the quality of the output beam [145]. Furthermore, the pressure tuning ability of AR-HCF, as well as its peculiar dispersion behavior around the zero-dispersion wavelength, allows for simultaneous phase-matching of all known Raman transitions of multi-species analytes [146].

AR-HCFs provide low-loss broadband guidance even for core diameters as large as tens of micrometers, reducing the pulse energies required for strong non-linear interactions from the millijoule to the microjoule level, therefore, allowing scaling from kHz to MHz repetition rates [147]. Due to this nature of wave-guiding, these classes of fibers are ideal candidates for the enhancement of many non-linear processes by extending the interaction length, and therefore, improving the efficiency of the non-linear processes such as self-phase modulation, supercontinuum (SC) generation, stimulated Raman scattering, and other FWM process. FWM is an extremely phase-sensitive non-linear process, with its efficiency determined by the relative phases of the four interacting beams and how these phases change over longer distances [62]. In this work, we use picosecond, narrowband laser pulses at 1064 nm wavelength as our pump and probe, and a fiber-based supercontinuum source at 1150 - 1700 nm as Stokes to produce nitrogen CARS signal at  $\sim 2331 \text{ cm}^{-1}$  in a 2.96 cm piece of AR-HCF. Our setup allows simultaneous, multiplex CARS signal detection within the range of Raman shifts from 600 to  $3500 \text{ cm}^{-1}$ . We also study different properties of AR-HCF, such as dispersion factor (D) [148] to predict the wave-vector mismatch ( $\Delta k$ ) in air-filled AR-HCF. The fiber that we use has broadband guidance that covers the range of the four beams involved in our CARS experiment. We then show up to  $170 \pm 1$  times enhancement in nitrogen signal when AR-HCF is used in free-coupling regime compared to the case when no fiber is present.

This enhanced signal shows near-zero non-resonant background (NRB), the main limiting factor in CARS spectroscopy [149, 150]. In other words, the fiber's cladding does not add a substantial NRB to the enhanced signal. This fact is attributed to a near-zero overlap between light, confined in the hollow core, and the fiber's cladding. Residual NRB produced in the cladding glass (due to a finite overlap) and in the air is minimal.

## 8.2 AR-HCF Properties

Figure 8.1 (a,b) show the schematic and the scanning electron micrograph (SEM) image of our AR-HCF manufactured using a stack-and-draw technique [151, 152]. We recorded pump and Stokes' beam profiles before and after the AR-HCF (figure 8.1, c-f). This measurement was done when the coupling efficiency for both the pump and Stokes beams was close to 46% in a free-coupling regime. Figure 8.1 (d,f) show the near-field mode profile of the core-guided modes of the fiber for pump and Stokes beams when the CARS signal was observed. Note that the pump beam is not a perfect Gaussian due to the characteristics of the picosecond Nd:YVO<sub>4</sub> laser (APLX-10, Attodyne, Inc.) that we are utilizing in our setup. While the capillary approximation is a convenient way to describe the group velocity dispersion (GVD) and D factor in most HC-PCFs, it does not work for this particular fiber due to its unique structure. However, other models can describe these values for the AR-HCF more accurately. We calculate and plot the dispersion factor of our revolver fiber using the anti-resonant ring model [153], which utilizes the Zeisberger-Schmidt approximation. In this model, the chromatic dispersion is dominated by the resonances of the annuluses while the order and number of these annuluses have a minor impact on the fundamental core dispersion. The effective refractive index ( $n_{eff}$ ) of a waveguide mode confined within the fiber core can be calculated as:

$$n_{eff}(\lambda) = n_g(\lambda) - A\lambda^2/n_g(\lambda) - BE(\lambda)C(\lambda)\lambda^3, \quad (8.1)$$

where  $n_g(\lambda)$  is the refractive index of the gas filled in the core of the fiber and A, B, C and E are defined parameters:  $A = \frac{j_{01}^2}{8\pi^2 R^2}$ ,  $B = \frac{j_{01}^2}{16\pi^3 R^3}$ ,  $C(\lambda) = \cot \frac{2\pi w \sqrt{n_s^2(\lambda) - n_g^2(\lambda)}}{\lambda}$ , and  $E(\lambda) =$

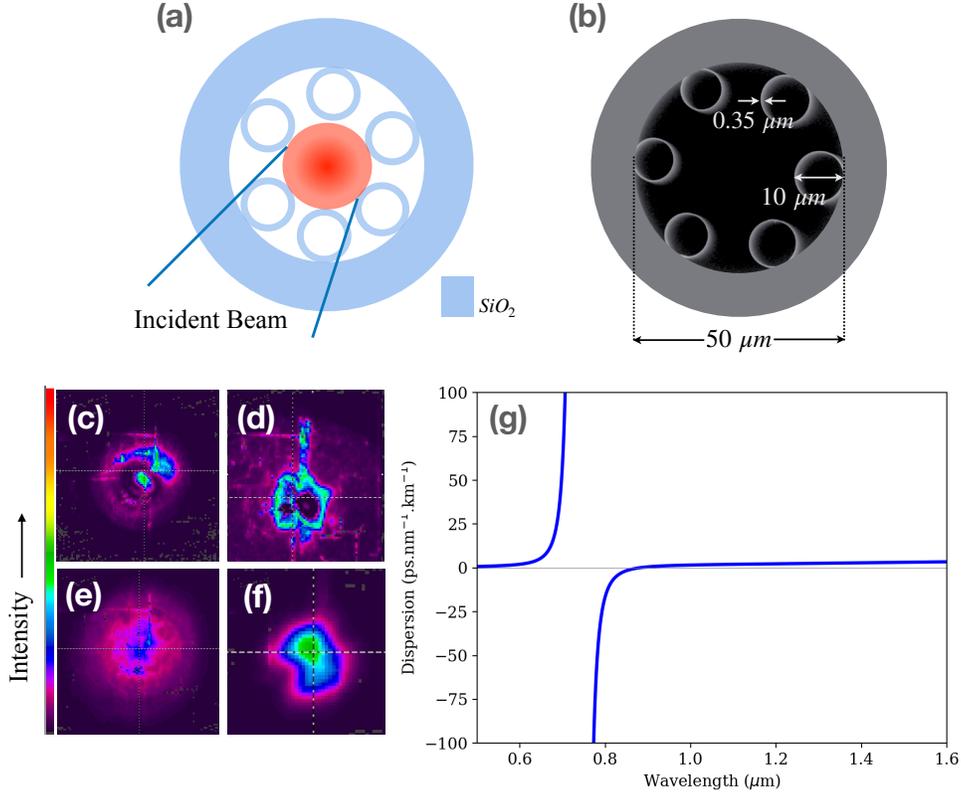


Figure 8.1: Properties of the AR-HCF used in our experiment, (a) schematic of the structure, (b) SEM image of the cross-section and the important measurements (the radius of each ring, the thickness of their walls, and the core size of the fiber), (c,e) before and (d,f) after fiber beam-profiles of pump and Stokes respectively, and (g) the calculated dispersion factor using the ring model.

$\frac{n_s^2(\lambda) - n_g^2(\lambda)}{n_g^3(\lambda) \sqrt{n_s^2(\lambda) - n_g^2(\lambda)}}$  for the fundamental mode ( $HE_{11}$ ) with  $R$  being the core radius,  $n_s$  being the refractive index of the rings' material (glass), and  $j_{01} = 2.405$  being the root of the zeroth order Bessel function ( $j_0(u) = 0$ ) [153]. Here,  $n_{eff}$  is used to calculate the propagation constant and, therefore, the D factor. Due to the cotangent dependence in  $C(\lambda)$ , the zero dispersion wavelengths (ZDWs) can be tuned by the capillary thickness  $w$  (in our case,  $0.35 \mu\text{m}$ ) to optimize the desirable processes at the operating wavelengths. However, if the process of interest spans a broad wavelength range, it is likely to cross a resonance, making simple approximations of the phase mismatch difficult. A Taylor expansion of the propagation constants will fail due to singularities. The resonant wavelengths are given by the wavelengths where the cotangent diverges:

$$\lambda_{ZD} = \frac{2w}{l} \sqrt{n_s^2 - n_g^2}, \quad (8.2)$$

where  $l = 1, 2, \dots$ . The cotangent dependence also produces broad regions of anomalous dispersion, which can be balanced against the normal dispersion of the medium inside the fiber to provide another avenue for phase matching. In our experiment, the coherence length for the CARS process in nitrogen is around 3 mm, which is significantly shorter than the length of the fiber, and hence, the waveguide dispersion should be included in the phase mismatching calculations. Figure 8.1 (g) shows the dispersion factor of our AR-HCF calculated using these considerations, which indicates no singularities in the range of our interest ( $\sim 800$  nm-1700 nm). Applying the phase matching condition in the CARS process:  $\Delta k = k_{Stokes} + k_{signal} - 2k_{pump}$  where  $k_{pump} = k_{probe}$  (degenerate CARS), we can have a decent estimation of the phase mismatching as a function of pressure and wavelength [154] for our experiment giving the possibility of using a pressure-controlled setup which uses different buffer gases to enhance CARS spectroscopy even further.

### 8.3 Experimental Setup

Our setup is shown in Figure 8.2. We use a laser beam generated in an Nd:YVO<sub>4</sub> laser with a 1 MHz repetition rate, 7 ps pulse duration, and a wavelength of 1064 nm divided into two legs using a polarizing beam splitter (PBS). Half-wave plates are used in combination with each PBS to control the power of each leg. One leg is used as our pump and probe, and the other leg goes through an approximately 2 m long large mode area fiber (LMA-20) to generate a broadband SC (900 – 1700 nm) using a plano-convex lens (LA1509-C, Thorlabs, Inc.). The generated SC is then collimated by an off-axis parabola (OAP) (MPD129-P01, Thorlabs, Inc.) and is guided to the rest of the setup. A long-pass filter (FELH1150, Thorlabs, Inc.) is used right after the OAP to cut the lower side of the SC spectrum.

Both beams are then combined on a dichroic beam splitter (LPD02-1064RU-25, Semrock, Inc.) and aligned to a polarizer and a neutral density filter (NDF) to adjust their powers, and then are focused into a 2.96 cm long AR-HCF with an infinity-corrected achromatic lens (AC254-050-C,

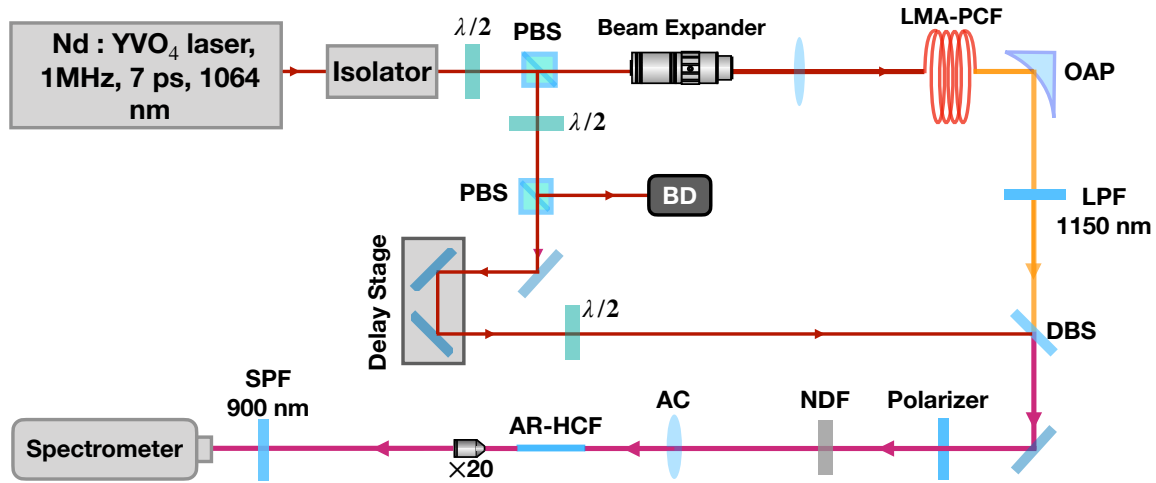


Figure 8.2: Schematic of our experimental wave-guided CARS setup. Abbreviation for the optical elements: PBS, polarizing beam splitter; BD, beam dump;  $\lambda/2$ , half wave-plate; OAP, off-axis parabola; LMA-PCF, large mode area photonic crystal fiber; LPF, long-pass filter; DBS, dichroic beam splitter; NDF, neutral density filter; AC, achromatic lens; AR-HCF, anti-resonant hollow-core fiber; and SPF, short-pass filter.

Thorlabs, Inc.) with a focal length of 5cm. The fiber is cut to this length using high precision, large diameter optical fiber cutter/cleaver (3SAE-LFC II, Technologies, Inc.) and then is mounted on a fiber holder (HFF001, Thorlabs, Inc.) fixed on a manual 3-axis translation stage for a precise alignment. A microscope objective (M-20 x, Newport, Inc.) is used after the fiber to collect and collimate the output beam into a short-pass filter with cut-off wavelength at 900 nm (FES0900, Thorlabs, Inc.), and then a CCD spectrometer (Holospec, Andor with the attached TE-cooled CCD (iDus416, Andor, Inc)). This short-pass filter removes the intense bands of the fundamental and the SC while detecting the relatively weak CARS signal. Argon, neon, and mercury lamps (StellarNet Inc.) are used to calibrate each CCD channel separately. The delay stage in the setup controls the temporal overlap between the pump and Stokes beams. To calibrate our setup further, we optimize a CARS signal of a sample of polystyrene beads, with a bead size of  $3 \mu\text{m}$  (No. 77523, Sigma Aldrich, Inc.) deposited on a coverslip (Micro Cover Glasses, VWR) under the micro-spectrometer [155].

## 8.4 Results

Our experimental results are shown in figure 8.3. The top panel (a) compares the two nitrogen CARS signals obtained, one from the free-coupling pump and Stokes in a 2.96 cm long air-filled AR-HCF (the blue curve) using an AC lens with a 5cm focal length and the other (red curve) from ambient air, meaning no fiber was present, and pump and Stokes were simply overlapped and focused in the air using the same AC lens. The CARS signal collected from AR-HCF is measured on CCD while the coupling efficiencies for the pump beam is around 70% and for the Stokes beam is  $65 \pm 5\%$ . These values are calculated by simply dividing the measured output powers by the measured input powers. The coupling efficiency for multimode fibers can be evaluated more precisely using the overlapping integral theory [156]. The input powers of the pump and Stokes beams are 180 mW and 3.5 mW, respectively.

Comparing these two curves shows  $170 \pm 1$  times enhancement in the collected signal from the AR-HCF. This enhancement was possible by providing a longer interaction path through the HCF and, therefore, improving the efficiency of the phase-matched FWM. We can also calculate the enhancement factor theoretically, considering  $P_{CARS} = I_{CARS} \times S$ , where P, I, and S stand for power, intensity, and the interaction cross-section area, respectively. Considering that the beam size before the focus is 1 cm, the focal length of the AC is 5 cm, the AR's core radius is  $15 \mu m$ , and  $I_{CARS} \propto P_{pump}^2 P_{Stokes} l^2 / S^2$  ( $l$  being the interaction length), we can calculate the enhancement factor  $\eta$  as:

$$\eta = \frac{(l_{AR}/S_{AR})^2 T_{pump}^2 T_{Stokes}}{(l_{ambient}/S_{ambient})^2}. \quad (8.3)$$

Here,  $l_{AR}$  is the length of the fiber,  $S_{AR} = \pi a^2$  ( $a$  being AR's core radius),  $l_{ambient}$  is two times the Rayleigh range in ambient air, and  $S_{ambient}$  is equal to  $\pi w_0^2$  with  $w_0$  being the beam waist at the focus in ambient air.  $T_{pump}$  and  $T_{Stokes}$  are the coupling efficiencies for pump and Stokes beams, respectively. We find the theoretical enhancement factor to be around 170, which perfectly

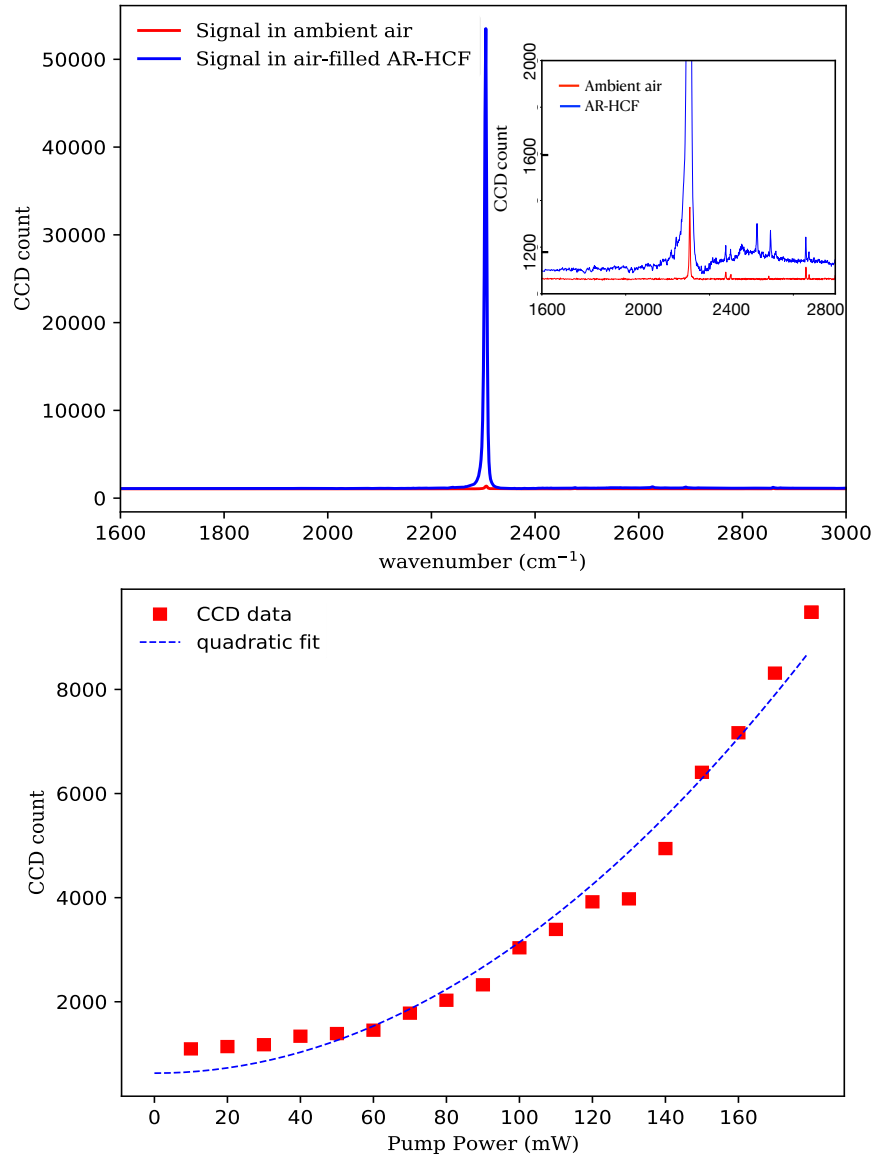


Figure 8.3: (a) The CARS signal of nitrogen at  $2331\text{ cm}^{-1}$  (Q-branch vibrational transition) in a 2.96 cm long air-filled AR-HCF compared to the CARS signal from the ambient air (no fiber present). Inset: enlarged plot in the lower CCD count region for better resolution. The spikes in the region between  $2400\text{ cm}^{-1}$  and  $2800\text{ cm}^{-1}$  only appear at very short acquisition times (here 0.05s). This is because of the way that the CCD spectrometer operates. (b) Pump power-dependent CARS signal measurement. Since the pump beam is used as both pump and the probe beams, the quadratic dependence of the CARS signal is expected.

matches what we obtained experimentally.

Moreover, no substantial NRB is added to the signal from the fiber's cladding due to its unique design properties. This fact is due to a near-zero overlap between light, confined in the core, and

the fiber's cladding. As one can see, the residual non-resonant background produced in the glass cladding (due to a finite overlap) and in the air is minimal. Our measured CARS signal to NRB ratio in the air-filled AR-HCF is  $\sim 350$ , while the same ratio that we measure for ambient air is  $\sim 520$  at its best. One should be careful not to confuse the two separate NRB's contributions that come from both the non-linear interaction of the laser and the fiber material and the non-resonant susceptibility of the nitrogen molecules. When comparing the two NRB in the vicinity of the nitrogen signal in both ambient air (red curve in figure 3) and in the presence of the fiber (blue curve in figure 3), we are only comparing the contribution of the expected NRB produced by the fiber's material. In fact, the background that is magnified in the inset of figure 3(a) is mainly from nitrogen, and the NRB coming from the air stays the same, with and without the presence of the fiber, at its best. There are several techniques for NRB reduction in CARS spectroscopy, such as time-resolved scheme [157, 158], heterodyne detection [159, 160], and polarization control [161–165]. The latter can be achieved through polarization control of the involved beams. In principle, if further background suppression is needed in our future experiments, we can utilize the polarization technique since anti-resonance hollow-core fibers can be sufficiently short and straight and be designed to maintain the polarization of guided fields, thus enabling polarization NRB suppression for waveguide-enhanced CARS.

Note that in both cases, the focal length and the beam size at the focus are the same. The reason that the oxygen CARS signal at  $1556 \text{ cm}^{-1}$  was not detected is because of the efficiency roll-off of the CCD spectrometer at the edge of each channel (channel 1:  $600 - 1500 \text{ cm}^{-1}$  and channel 2:  $1500 - 3500 \text{ cm}^{-1}$ ). Moreover, even though the oxygen signal should be 15 times weaker than the nitrogen one [166], the use of an SPF at  $900 \text{ nm}$  to get rid of the strong fundamental and SC filters the oxygen signal even more.

Finally, although the primary enhancement comes from the elongated interaction length provided with the hollow core of the fiber, for the ultra-short pulses in such non-linear processes, temporal walk-off due to dispersion in the medium is unavoidable [127]. To overcome this obstacle, pressure tuning inside the core is an option to manipulate the dispersion and fulfill the phase

matching condition [62, 64].

In figure 8.3 (b), as a proof of concept that the signal we detected is, in fact, the CARS signal, we demonstrate that its CCD peak count dependence on the power of the pump beam, which is also used as probe, is quadratic as expected.

## **8.5 Conclusion**

We successfully demonstrate  $\sim 170$  times enhancement with a near-zero NRB in nitrogen CARS signal using a short piece of AR-HCF in a free-coupling regime. This method, which utilizes a much less complicated table-top setup compared with most fiber-based experiments, can be extended to many multi-species gas samples and also to biomedical solutions and functionalized residues. In the near future, we are planning to expand this method to detect the CARS signal of liquids such as different types of protein solutions and antibodies.

## 9. COHERENT ANTI-STOKES RAMAN SPECTROSCOPY IN HOLLOW-CORE PHOTONIC CRYSTAL FIBERS<sup>†</sup>

### 9.1 Introduction

This chapter is dedicated to expanding on the previous chapter which was published as a short letter. Hence, I will discuss the full process of the experiment in detail in the next following sections. The motivation for this work was inspired by the pandemic of COVID-19 at the time. We were searching for different options to study the virus itself as well as its antibody. One potential candidate was wave-guided coherent anti-Stokes Raman scattering (CARS) spectroscopy to obtain information about these analytes by observing their CARS signal in the fingerprint region. Our goal was to enhance the signal by using a short piece of hollow-core fiber that was filled with goat anti-human IgG antibody. We had several options in terms of choosing a proper hollow-core photonic crystal fiber (HC-PCF):

1. Kagome HC-PCF,
2. HC-1060 HC-PCF,
3. AR-HCF.

We first study each of these options by performing CARS spectroscopy in the air at atmospheric pressure. In chapter 7, we studied some important properties of the Kagome fiber as a potential candidate for our later CARS spectroscopy in gaseous media even before the pandemic. However, at the time of this experiment, we decided to first start with the fibers that we had readily available and did not need a special design for when using for liquid analytes. We started our experiment with an HC-1060 PCF (HC-1060-02, NKT Photonics) with a small core diameter of 10 microns whose mechanism is photonic bandgap (PBG). In the next section, I will elaborate on the properties

---

<sup>†</sup>This chapter elaborates further and presents more data from previous chapter

of this fiber and why we decided not to use it, and instead, use an anti-resonance HCF also known as revolver fiber with a much larger core diameter.

## **9.2 HC-1060 PCF**

### **9.2.1 Photonic Bandgap Wave-Guiding Mechanism**

Photonic crystal fibers (PCFs) can be classified into two major families: solid-core (SC-PCF) and hollow-core (HC-PCF). Throughout this thesis, my focus is on the second family; HC-PCF. PCFs can also be classified into three main classes based on their wave guidance:

- Modified Step Index (MSI),
- Inhibited Coupling (IC),
- Photonic Bandgap (PBG).

In this section, I highlight some of the features of the last item whose the wave-guidance through HC-1060 takes place. More precisely, I focus on the air-guiding PBG mechanism in HC-PCFs. These classes of optical fibers are characterized by a central hollow core and a micro-structured cladding which exhibit PBG effects that happen as a result of periodic micro-structuring of air holes of the cladding region. Historically, the idea of PBG fibers first emerged in 1991 suggesting that light can be trapped in the core of an HCF that has a periodic wavelength-scale lattice of microscopic holes [167]. This idea suggested that these periodic micro-structures exhibit a range of angles and wavelengths where the incident light would mostly be reflected. These wavelengths are called "stop bands", and this mechanism incorporates some natural phenomena such as butterfly wings and credit cards holograms.

This mechanism in HC-PCFs is slightly different from in PBG materials. In the latter, although these wavelengths are limited, the stop bands block the propagation in all directions and suppress all the optical vibrations within the range of wavelengths through the PBG [136]. For the HC-PCFs, however, the holey cladding runs along the entire length of the fiber, and with a clever design, the fiber can trap light in its hollow core surrounded by micro-structured glass [167].

## 9.2.2 HC-1060 PCF Properties

Figure 9.1 shows salient properties of the HC-1060 PCF that we used initially as a trial fiber for our CARS experiment in the air. This fiber is available with design wavelengths of 800, 1060, 1550, and 2000 nm. Some of its features are listed below:

- Large continuous operation bandwidth.
- Near-zero dispersion at the design wavelength.
- Quasi-Gaussian fundamental mode.
- No Fresnel reflection from the end faces of the fiber (Modal index = 1).
- Small number of core modes and parasitic surface modes.

Tables 9.1 and 9.2 present the HC-1060's essential physical and optical properties, respectively.

Table 9.1: Physical properties of HC-1060, NKT Photonics.

Physical Properties	
Core Diameter (D)	$10 \mu\text{m} \pm 1 \mu\text{m}$
Pitch ( $\Lambda$ )	$2.75 \mu\text{m}$
Air filling fraction PBG region	$> 90\%$
Hole region diameter	$50 \mu\text{m}$
Cladding diameter	$123 \mu\text{m} \pm 5 \mu\text{m}$
Coating diameter (single layer acrylate)	$220 \mu\text{m} \pm 50 \mu\text{m}$

We tried a short piece of HC-1060 in our setup which is fully described in section 8.3. We first, needed to measure the transmission range to assure that it fulfills our desired wavelength range. Figure 9.2 demonstrates non-quantitative spectra of the SC that is used as our Stokes beams in the FWM process before and after a 3-cm-long piece of HC-1060.

To measure the spectrum before HC-1060, we used several ND filters mounted on a manual filter

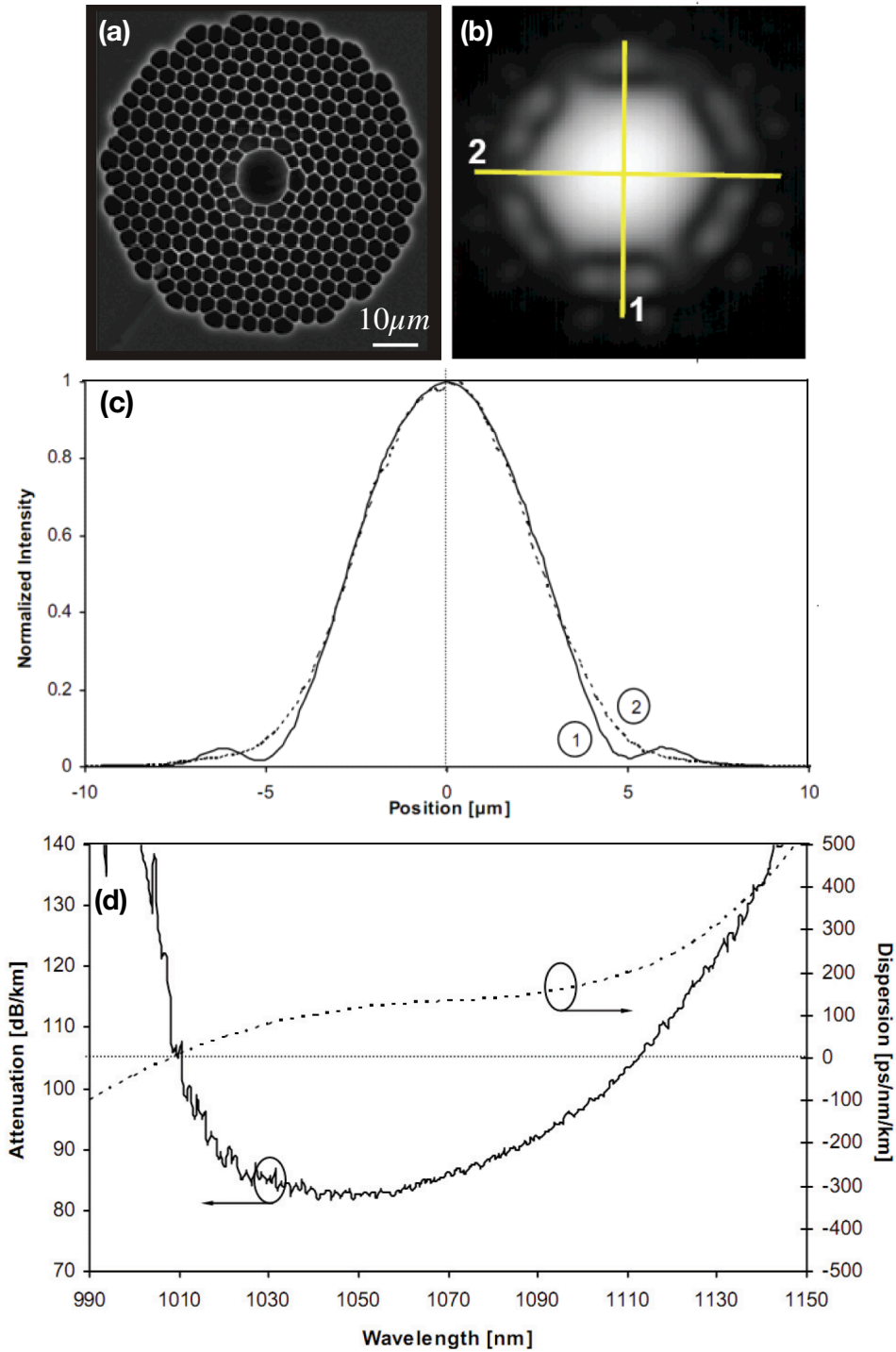


Figure 9.1: Properties of HC-1060 originally used for this experiment. (a) SEM image of the cross-section of the fiber which shows a relatively small core diameter of around 10 microns, (b) near-field spectral phase profile, (c) near-field intensity distribution, and (d) typical attenuation and dispersion over a kilometer. Reprinted from NKT photonics website.

Table 9.2: Optical properties of HC-1060, NKT Photonics.

Optical Properties	
Center wavelength	1060 nm
Attenuation at 1060 nm	<0.1 dB/m
Dispersion factor at 1060 nm	120 ps/nm/km
Dispersion slope at 1060 nm	1 ps/nm <sup>2</sup> /km
Mode field diameter	7.5 $\mu\text{m} \pm 1 \mu\text{m}$
Effective mode index	$\sim 0.99$

wheel (FW2A, Thorlabs) to reduce the intensity of the SC to match the intensity of the spectrum after the fiber. It is worth mentioning that based on the design of HC-1060, the capillary approximation would be a great way to measure the dispersion factor which is a salient feature of a fiber. After several unsuccessful attempts to measure the CARS signal after HC-1060, we concluded that the small core diameter of the fiber was one of the factors that made this process difficult.

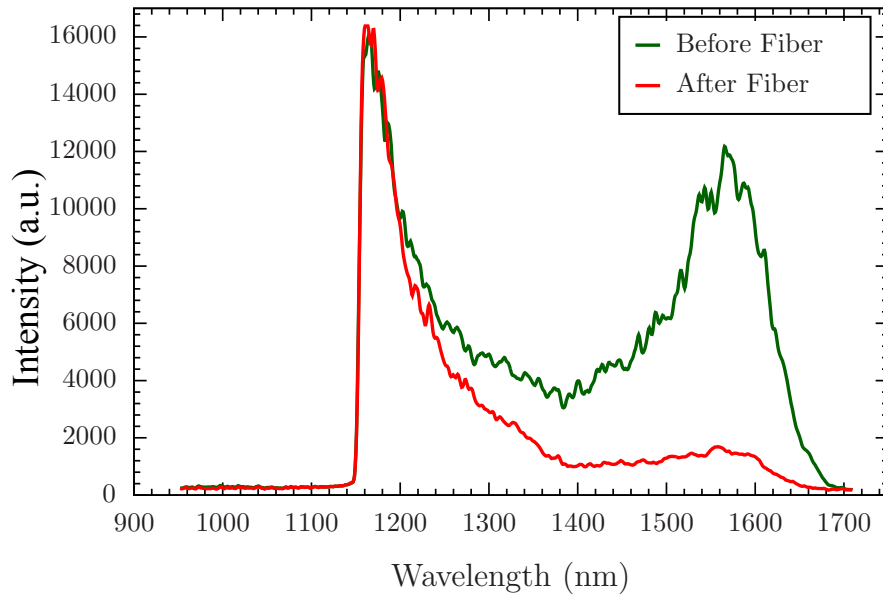


Figure 9.2: Spectra of the SC generated in an LMA fiber which is used as the Stokes beam before (green) and after (red) a 3-cm-long HC-1060 HCPCF. The intensity of the before spectra is scaled by ND filters to match the intensity of the output for a better comparison.

Hence, we decided to use a different fiber with a different design and a larger core diameter to proceed with our experiment. A reasonable option was AR-HCF with a core diameter of  $\sim 30$  microns and a different wave-guiding mechanism which I will explain in the next section.

### 9.3 AR-HCF (Revolver)

The wave-guidance in an AR-HCF follows a simple mechanism so-called anti-resonant reflective optical wave-guiding (ARROW) which indicates that the fiber's core boundary layer acts as a Fabry-Perot resonator. Fabry-Perot resonator supports the transmission of optical frequencies which match the anti-resonance of the core wall [168].

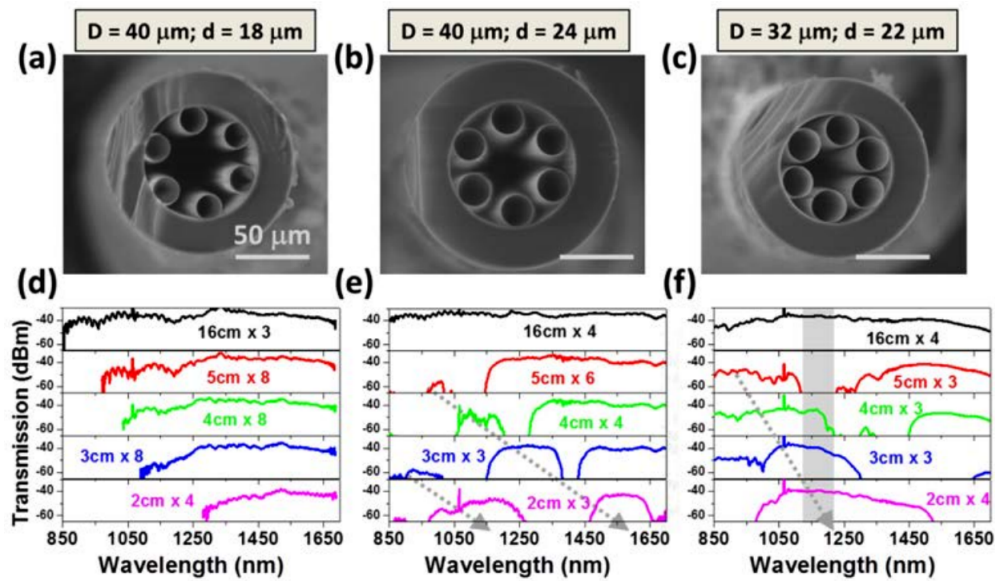


Figure 9.3: Characterizations of three AR-HCFs by the manufacturer. (a,b,c) SEM images of three AR-HCFs with different tube sizes and core radii (the scale bar is the same for all three images). (d,e,f) Transmission spectra of each fiber under different bending radii. Legend on each plot shows the bending radius (cm)  $\times$  number of turns. Reprinted from [152].

Hence, the resonant wavelengths cannot propagate in the core and leak through the cladding. This makes these fibers one of the most reliable low-loss HCFs for many light-matter interaction experiments. The properties of the 2.96 cm AR-HCF used in our experiment are shown in 8.1.

Moreover, figure 9.3 illustrates three AR-HCFs with different core and annulus sizes from the same manufacturer. In the bottom row, the bending loss for each case is presented, however, for our experiment, the bending loss was not a major concern because our fiber was short and straight.

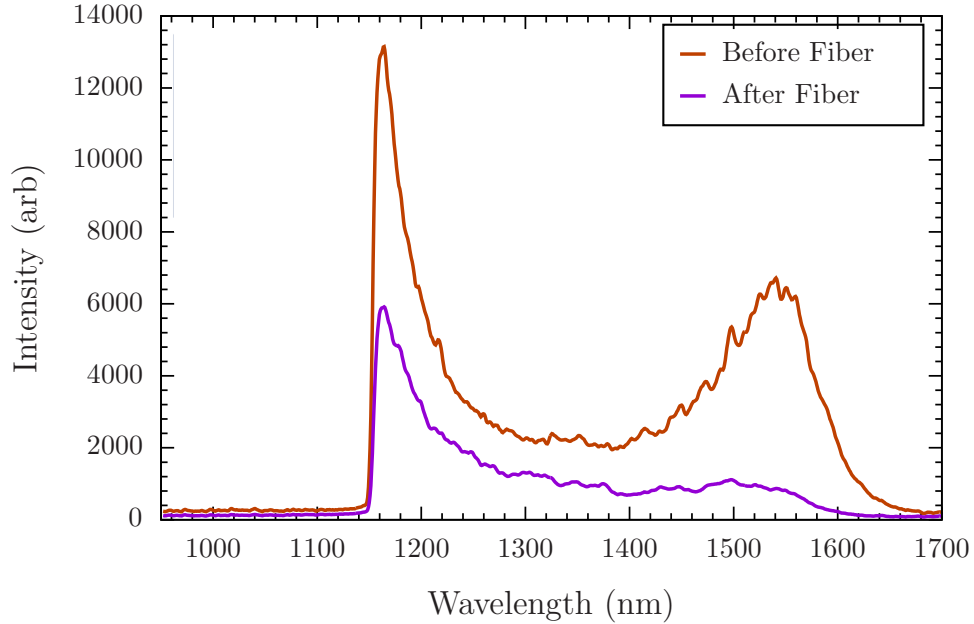


Figure 9.4: Spectra of the SC generated in an LMA fiber which is used as the Stokes beam before (red) and after (purple) a 2.96-cm-long AR-HCF. The intensity of the before spectra is scaled by ND filters to match the intensity of the output.

We can calculate the enhancement factor theoretically knowing the powers of each input beam, their coupling efficiencies, beam sizes, and interaction lengths (which is twice the Rayleigh range in the ambient air, and equals the length of the fiber for the wave-guided case). Power of the CARS signal,  $P_{CARS}$ , can be written as:

$$P_{CARS} = I_{CARS} \times S \propto I_p I_{probe} I_{St} L^2 S, \quad (9.1)$$

where  $I_{CARS}$  is the intensity of the signal, and  $S$  is the area of the interacting beams which we ideally keep the same for all three beams.  $I_p$ ,  $I_{probe}$ , and  $I_{St}$  are the pump, probe, and Stokes

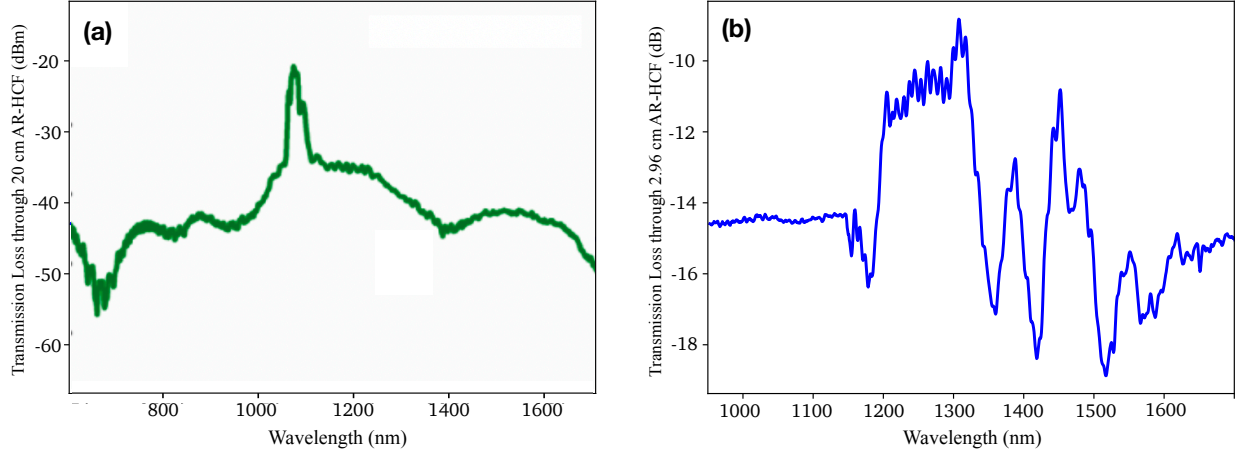


Figure 9.5: Transmission Loss for AR-HCF. (a) Transmission measured by the manufacturer for a 20-cm-long AR-HCF and normalized for a-meter-long fiber. Reprinted from [148]. (b) The transmission loss we measured for our 2.96cm-long AR-HCF. The difference is resulted from the length difference as well as the different coupling methods. The loss we measure is mostly due to the coupling issues since we do not use couplers, and instead, we free-couple the beams into AR-HCF.

beams' intensities, respectively.  $L$  is the interaction length. The fundamental at 1060 nm is used as both pump and the probe beams; hence, equation 9.1 can be written as:

$$P_{CARS} \propto \frac{P_p^2}{S_p^2} \frac{P_{St}}{S_{St}} L^2 S, \quad (9.2)$$

but since the beam size is the same for both beams,  $S_p = S_{St}$  and we call it  $S$ . Finally, the power of the beams should be kept constant, and the coupling efficiency for each beam should be taken into consideration. Therefore, we can write the enhancement factor  $\eta$  as follows:

$$\eta = \frac{L_{fiber}^2 / S_{fiber}^2 T_p^2 T_{St}}{L_{ambient}^2 / S_{ambient}^2}, \quad (9.3)$$

where  $L_{fiber}$  is AR's length, which in our experiment is 2.96 cm,  $S_{fiber} = \pi a^2$  where  $a$  is AR's core radius,  $L_{ambient}$  is the interaction length for the two fundamentals in ambient air, and  $S_{ambient}$  is equal to  $\pi w_0^2$  with  $w_0$  being the beam waist at the focus in ambient air. The interaction length in the fiber can be reasonably assumed to be the entire length of the fiber. But for the ambient air, the

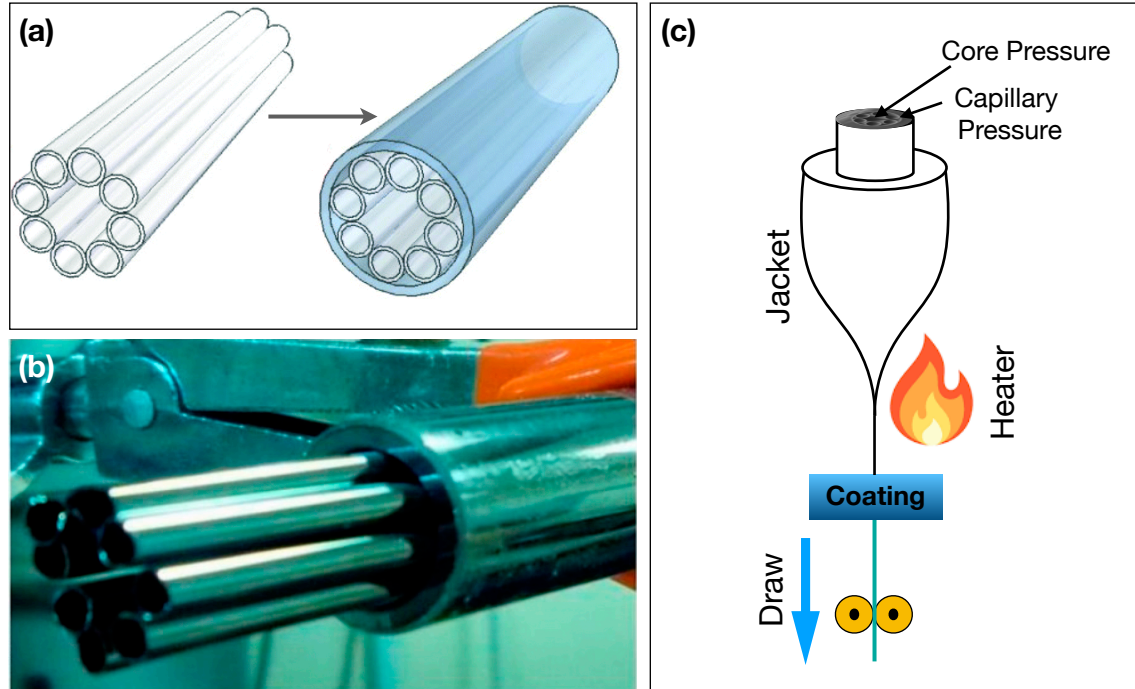


Figure 9.6: The Stack-and-draw technique used for manufacturing an AR-HCF. (a) The process of stacking the capillaries inside a silicon tube. Reprinted from [169]. (b) The same process but for a different material ( $As_{30}Se_{50}Te_{20}$ ). Reprinted from [170]. (c) The procedure of drawing and coating the fiber. The amount of pressure, temperature, and drawing tension determine the fiber's cross-section size (core and the cladding). Adapted from [171].

interaction length is estimated to be twice the Rayleigh range. Finally,  $T_{pump}$  and  $T_{Stokes}$  are the coupling efficiencies for pump and Stokes beams, respectively. After substituting all these values and considering 60% coupling efficiency for both fundamentals, the theoretical enhancement factor is calculated to be around 170, which is perfectly matching with what we obtain experimentally (figure 8.3).

Figure 9.7 shows the coherence length as a function of wavelength for the nitrogen in the AR-HCF. One should note that if the coherent length is sufficiently shorter than the length of the wave-guide, we need to treat the phase mismatch in the CARS process, including the wave-guide dispersion, carefully. As seen on this plot, the coherence length for the CARS process in nitrogen is around 3 mm, which is significantly shorter than the length of the fiber, and hence, the wave-guide dispersion should be included in the phase mismatching calculations as seen in section 8.2.

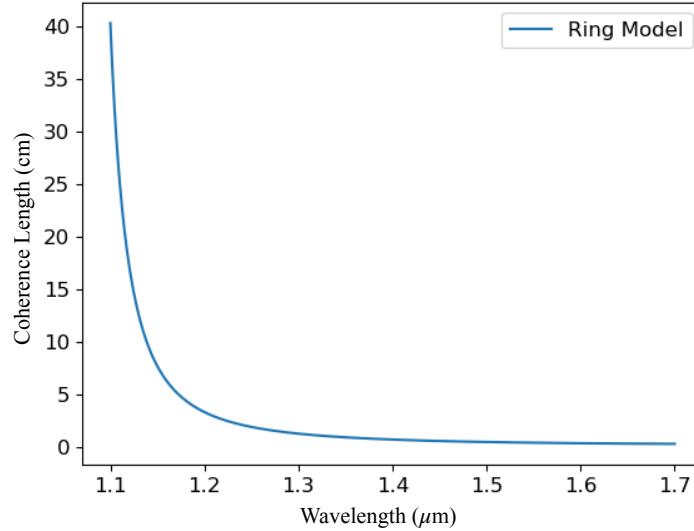


Figure 9.7: Coherence length calculated and plotted as a function of wavelength for the air-filled AR-HCF used in our wave-guided CARS experiment. The ring model is used for the calculation. As demonstrated in this plot, the coherence length can be as small as 3 mm for the range of the SC (1100 nm - 1700 nm) used as the Stokes beam.

#### 9.4 Stack and Draw Technique

Figure 9.6 demonstrates the technique called "stack and draw" used to manufacture the AR-HCF. First, they stack the fused silica capillaries inside a larger capillary as shown in figure 9.6 (a); then, by exerting proper pressure into the core and capillary and applying heat, they draw the ensemble vertically. By changing the pressure and drawing tension, they can achieve the desired fiber size. Figure 9.6 (c) demonstrates the drawing process. In the drawing process, for simple structures like the revolver fiber, one drawing stage is adequate. However, for HC-PCFs with complicated structures in the cladding, such as many layers of air holes, two drawing stages should be employed. In the first stage, the stacked assembly is drawn into a cane with the desired outer diameter. The cane is then inserted into a jacket tube and the final ensemble is drawn through a set of tractors. The reason for a smaller reduction ratio in the first stage is to prevent structure distortions. Afterward, a layer of coating is added to the outside jacket as the fiber passes through the tractors.

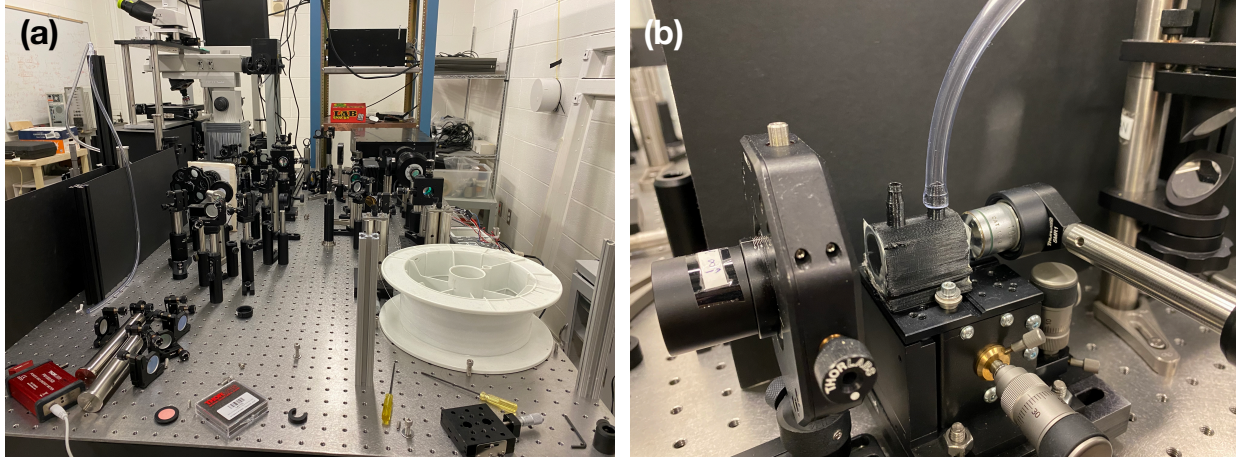


Figure 9.8: (a) CARS setup. The far left is the CARS microscope. The setup is interchangeable between the microscope that we use to align the setup, as demonstrated in appendix B and the wave-guided CARS spectroscopy. (b) 3D-printed gas cell with AR-HCF inside. The cell has two outlets for pressure control and is mounted on a 3D(XYZ) translation stage.

## 9.5 Gas Cell for Pressure controlled CARS

After detecting the CARS signal in the air-filled AR-HCF, we also tried to mount the fiber in a gas cell to repeat this experiment for several gases, such as methane and ethane. We 3D printed a small gas cell with a tray inside to hold the fiber straight. We used SolidWorks software for the design. Figure 9.8b shows the gas cell mounted on a 3D translation stage. The gas cell has two outlets for the entrance and exit of the gas and to conveniently control the pressure. One needs to simply let the gas in from one outlet and let the air out from the other without using fancy gas cells that need to be connected to the two ends of the fiber directly. The windows at the two ends of the cell are two coverslips (Micro Cover Glasses, VWR) glued to the edges with epoxy glue. The rest of the setup is the same as described in section 8.3.

Figure 9.9 demonstrates the beam profiles before and after entering the same piece of AR-HCF used before, but this time in the gas cell. These profiles are taken with a Spiricon beam profiler (Spiricon PY-III-HR-C-A, Ophir Photonics). Even though both beams seemed to be perfectly in the core, the nitrogen signal that we detected was feeble. We believe this is because the two windows used at the ends of the gas cells disperse the two beams differently and cause improper

overlap. Due to the time limitations at the time of this thesis, this part of the experiment could not move further. We plan to continue this project by running a set of diagnostics to improve the nitrogen signal in the gas cell and then try CARS signal detection for other gases such as methane ( $\text{CH}_4$ ) and ethane ( $\text{C}_2\text{H}_6$ ) or a mixture.

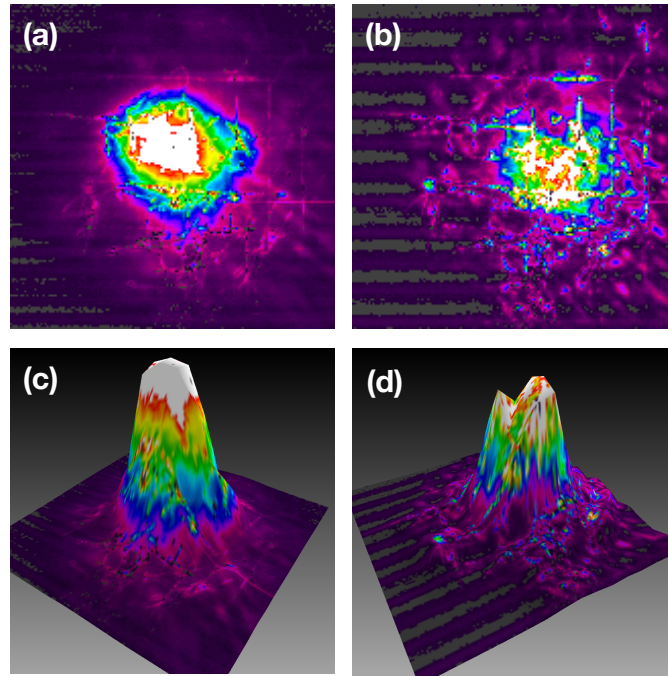


Figure 9.9: Beam profiles of the pump and Stokes beams after the air-filled revolver fiber placed in a gas cell. Both beams are perfectly in the core. (a,c) 2D and 3D near-field profile of Stokes, and (b,d) 2D and 3D near-field profile of the pump beam. As mentioned in 8.2, unlike the Stokes beam, the pump beam does not have a clean Gaussian profile.

## 9.6 CARS in AR-HCPCF filled with Goat Anti-Human IgG Antibody

Human health relies on the accurate and quick detection of antibodies generated in blood for evaluating the immune response of the body to contagious diseases such as the novel coronavirus, also known as COVID-19. Antibodies are Y-shaped proteins (shown schematically in figure 9.10(right)) produced by white blood cells to block the virus from intruding. The human body is capable of producing two different types of antibodies, some of which are temporary and some permanent, meaning that they have a memory to remember the intruder and attack it again in case of exposure. Immunoglobulin M (IgM) is one of the first types of antibodies produced when fighting a virus. The second type that is generated second is immunoglobulin G (IgG) which can be found in the blood test of patients that are exposed to the virus whose bodies had an immune response to the disease. In this section, I will discuss a method of antibody detection using HCPCFs in CARS spectroscopy.

HCPCFs have many applications as fiber-optic chemical sensors (FOCS) and biosensors (FOBS) [172]. They are also a great tool to improve many non-linear processes such as stimulated Raman scattering (SRS) and CARS [141] in biological samples. An analyte, such as a protein solution or blood sample, can flow through the air holes in the core and/or the cladding of an HCPCF through direct pumping, injection, or simply by capillary action[173] and form a periodic or a spatially chirped photonic lattice within the cylindrical rod of the host glass [174]. With suitable optimization of the fiber structure, the optical readout can be dramatically enhanced due to improved spatial overlap between the optical fields and the analyte, improving the output signal up to several orders of magnitude.

For this section, we use the same experimental setup used for section 8.3 but with a different fiber. This time, we use a 3-cm-long AR-HCPCF filled with goat anti-human IgG antibody. To fill this fiber, we use a glass capillary with one side heated and drawn to be as narrow as the AR fiber. We then use a pair of tweezers to gradually break the tip until the fiber fits inside the capillary. We

use relatively weak glue to secure the capillary to the fiber to avoid any leak while pumping the antibody into the capillary.

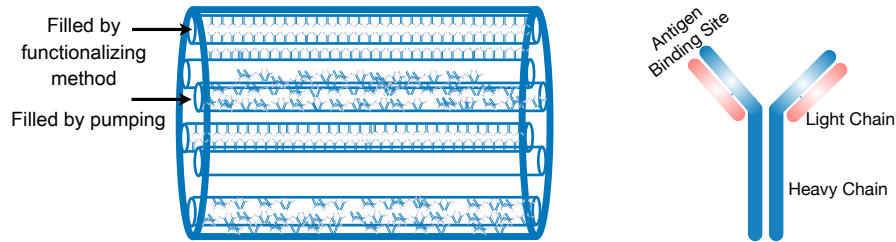


Figure 9.10: The schematic of the IgG-filled AR-HCPCF’s interior filled with two different methods. In the first method, the antibody is coated in the interior and exterior walls of the air holes (the core and the six rings). In the second method that is used in this section, we only pump the antibody solution into the fiber and let it dry. As shown in this figure, antibody molecules are stacked on top of each other in a non-monolayer manner (left). The structure of the antibody molecule (right). The heavy chain labeled on the antibody molecule is the large polypeptide sub-unit, while the light chain is the small polypeptide subunit of an antibody.

We then start pumping the antibody solution into the fiber several times to make sure that all interior surfaces of the AR structure are covered by the solution and then let the fiber air dry for at least four hours to leave a residue in the fiber. The last step is necessary to ensure that the CARS signal will not be absorbed by the water in the solution. A better way to fill the fiber is a proper functionalization in which the antibody molecules stick to the interior parts of the fiber in a monolayer manner, as shown in figure 9.10(left). However, this needs a very specific procedure that we decided to use after trying our pumping method to see if we can detect any signal and then invest in more proper and complicated methods. Figure 9.10(right) shows the simplified structure of the antibody molecule and compares the two methods of filling the fiber.

Figure 9.12 shows the raw data taken on the glass slide covered with the antibody residue compared with the data taken from the antibody residue in AR-HCF. The blue curve is the raw data (the background is not removed) from the sample on the glass slide, and the red curve is taken from the IgG residue in AR-HCF (also, the background was not removed). The two plots have a similar

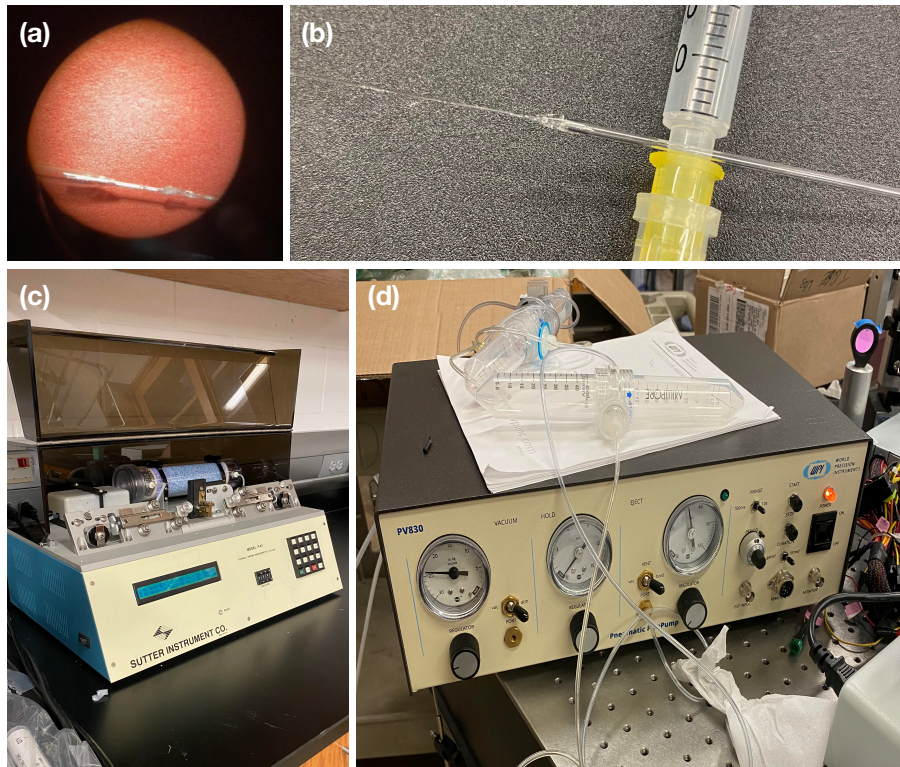


Figure 9.11: Process of filling AR-HCF with goat anti-human IgG antibody. (a) The thinned-out capillary is glued to the AR-HCF under the microscope. The glue is left to dry for no more than 2 hours so the solution does not leak during the injection, but the glue can be easily removed after the filling process is over. (b) Filling the fiber with IgG by injecting the solution of IgG into the capillary. (c) The stretching machine is used to thin out one side of the glass capillary to have a compatible diameter with the AR-HCF. (d) The pump system is used to fill the fiber. The IgG is pumped into the fiber several times to ensure it covers the most internal surfaces of the fiber. After this step is completed, the fiber is left at room temperature for at least four hours for the liquid to evaporate, and the IgG residue remains in the fiber's internal surfaces.

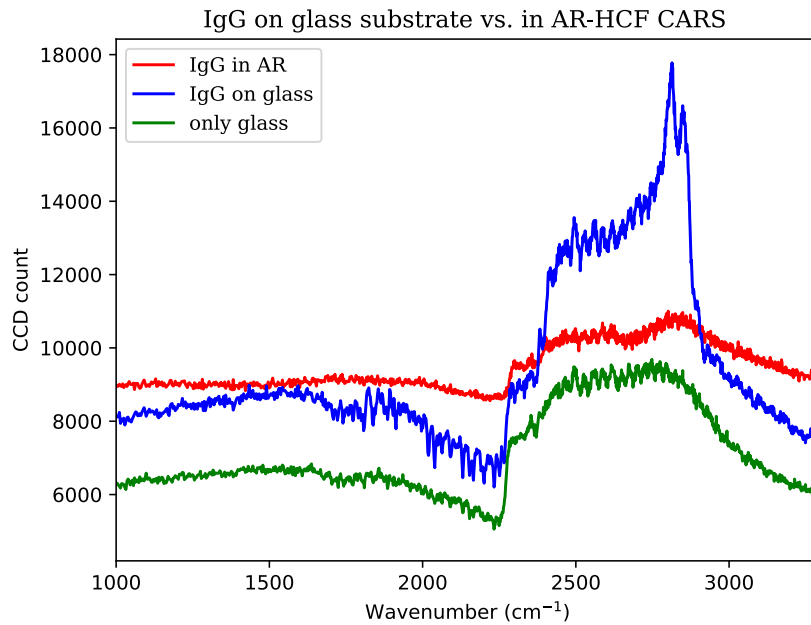


Figure 9.12: The Raw data from an IgG sample on a glass substrate (blue curve) compared to a 3-cm-long IgG-filled AR-HCF (the red curve is scaled to be comparable with the blue curve). However, they both follow the same trace, and the signal taken from the fiber is many times weaker. The green curve is the data taken only from the glass substrate.

trace. However, the data from the IgG-filled AR-HCF is taken in a ten times higher acquisition time and hence, is much weaker. This might be due to the inhomogeneous linear refractive index profile, such as that occurring in biological tissues that is shown to significantly alter stimulated Raman scattering (SRS) and coherent anti-Stokes Raman scattering (CARS) microscopy images.

## 9.7 Conclusion and Future Work

We investigate the CARS signal detection in two types of fiber with different wave-guide mechanisms; HC-1060 with photonic bandgap mechanism and AR-HCF with the anti-resonant reflective optical wave-guiding mechanism. Our findings show that by using a short piece of AR-HCF, we can enhance the CARS signal of nitrogen up to 170 times. We plan to run a similar experiment but for different types of gases, such as methane and ethane. This is the plan for the experiment, as led by graduate student J.T. Florence, next year. AR-HCF also is a great candidate for CARS signal detection in biological analytes such as IgG. Having a large core helps with filling the fiber, and the order of enhancement reduces the need for high pulse energies and consequently damages the sample. We detect a weak signal from IgG-filled AR-HCF, which resembles the signal collected from the same analyte on the glass microscope slide. We also plan to further invest and improve this experiment in the future.

## 10. SUMMARY AND FUTURE WORK

This dissertation details the two imperative applications of molecular coherence; ultrafast waveform production by synthesizing coherent Raman sidebands generated in Raman crystals alongside the CARS signal enhancement in hollow-core photonic crystal fibers. We achieved our goal of generating near-single-cycle pulses (4.8 fs) with desired waveforms by synthesizing the coherent Raman sidebands and optimizing the overall spectral phase. We then measured and analyzed these pulses by employing two separate methods: ix-FROG and multi-photon ionization. Using the first technique, we fully retrieved the phase and the amplitude of the generated pulses; however, the second measurement method has yet to be improved. Graduate student N. Marshall is planning to continue this experiment in the near future. We also investigated the phase-only control by studying the transfer of the TC of optical vortices in coherent Raman processes. Our results show that the value and the sign of the TC of each coherent sideband obey a simple relationship with the TC of the input pump and Stokes beams, resulting from the conservation of angular momentum for created and annihilated photons. We also study another consequential application of the coherent Raman effect; CARS spectroscopy, in particular, wave-guided CARS. We explore the possibility of enhancing the blue-shifted CARS signal for multiple gaseous and liquid samples such as antibodies. We successfully showed that by using a short straight piece of AR-HCF, we could improve the CARS signal in gaseous media up to two orders of magnitude. Although we were not able to show significant enhancement of the CARS signal in biological analyte with a similar benchmarking, we are confident that our current experiment is a strong foundation for our group's future works.

## REFERENCES

- [1] C. V. RAMAN and K. S. KRISHNAN, “A new type of secondary radiation,” *Nature*, vol. 121, pp. 501–502, Mar 1928.
- [2] K. Raman, C.V. Krishnan, “A new class of spectra due to secondary radiation. part i,” *Indian Journal of Physics*, pp. 399–419, 1928.
- [3] R. S. Krishnan and R. K. Shankar, “Raman effect: History of the discovery,” *Journal of Raman Spectroscopy*, vol. 10, pp. 1–8, 1981.
- [4] P. D. Maker and R. W. Terhune, “Study of optical effects due to an induced polarization third order in the electric field strength,” *Phys. Rev.*, vol. 137, pp. A801–A818, Feb 1965.
- [5] G. Sansone, L. Poletto, and M. Nisoli, “High-energy attosecond light sources,” *Nature Photonics*, vol. 5, pp. 655–663, Nov 2011.
- [6] S.-W. Huang, G. Cirimi, J. Moses, K.-H. Hong, S. Bhardwaj, J. R. Birge, L.-J. Chen, E. Li, B. J. Eggleton, G. Cerullo, and F. X. Kärtner, “High-energy pulse synthesis with sub-cycle waveform control for strong-field physics,” *Nature Photonics*, vol. 5, pp. 475–479, Aug 2011.
- [7] V. Shumakova, P. Malevich, S. Ališauskas, A. Voronin, A. M. Zheltikov, D. Faccio, D. Kartashov, A. Baltuška, and A. Pugžlys, “Multi-millijoule few-cycle mid-infrared pulses through nonlinear self-compression in bulk,” *Nature Communications*, vol. 7, p. 12877, Sep 2016.
- [8] M. T. Hassan, T. T. Luu, A. Moulet, O. Raskazovskaya, P. Zhokhov, M. Garg, N. Karpowicz, A. M. Zheltikov, V. Pervak, F. Krausz, and E. Goulielmakis, “Optical attosecond pulses and tracking the nonlinear response of bound electrons,” *Nature*, vol. 530, no. 7588, pp. 66–70, 2016.
- [9] A. V. Sokolov and S. E. Harris, “Ultrashort pulse generation by molecular modulation,” *Journal of Optics B: Quantum and Semiclassical Optics*, vol. 5, p. R1, dec 2002.
- [10] A. Bahari, A. A. Zhdanova, M. Shutova, and A. V. Sokolov, “Synthesis of ultrafast wave-

- forms using coherent raman sidebands,” *Phys. Rev. A*, vol. 102, p. 013520, 2020.
- [11] A. V. Sokolov, M. Y. Shverdin, D. R. Walker, D. D. Yavuz, A. M. Burzo, G. Y. Yin, and S. E. Harris, “Generation and control of femtosecond pulses by molecular modulation,” *Journal of Modern Optics*, vol. 52, no. 2-3, pp. 285–304, 2005.
- [12] R. F. Begley, A. B. Harvey, and R. L. Byer, “Coherent anti-stokes raman spectroscopy,” *Applied Physics Letters*, vol. 25, no. 7, pp. 387–390, 1974.
- [13] A. Zumbusch, G. R. Holtom, and X. S. Xie, “Three-dimensional vibrational imaging by coherent anti-stokes raman scattering,” *Phys. Rev. Lett.*, vol. 82, pp. 4142–4145, May 1999.
- [14] T. W. Kee and M. T. Cicerone, “Simple approach to one-laser, broadband coherent anti-stokes raman scattering microscopy,” *Opt. Lett.*, vol. 29, pp. 2701–2703, Dec 2004.
- [15] H. Kano and H.-o. Hamaguchi, “Ultrabroadband ( $>2500\text{cm}^{-1}$ ) multiplex coherent anti-stokes raman scattering microspectroscopy using a supercontinuum generated from a photonic crystal fiber,” *Applied Physics Letters*, vol. 86, no. 12, p. 121113, 2005.
- [16] J.-X. Cheng, L. D. Book, and X. S. Xie, “Polarization coherent anti-stokes raman scattering microscopy,” *Opt. Lett.*, vol. 26, pp. 1341–1343, Sep 2001.
- [17] D. Oron, N. Dudovich, and Y. Silberberg, “Femtosecond phase-and-polarization control for background-free coherent anti-stokes raman spectroscopy,” *Phys. Rev. Lett.*, vol. 90, p. 213902, May 2003.
- [18] M. Okuno, H. Kano, P. Leproux, V. Couderc, J. Day, M. Bonn, and H.-o. Hamaguchi, “Quantitative cars molecular fingerprinting of single living cells with the use of the maximum entropy method,” *Angewandte Chemie International Edition*, vol. 49, no. 38, pp. 6773–6777, 2010.
- [19] H. Segawa, M. Okuno, H. Kano, P. Leproux, V. Couderc, and H. o Hamaguchi, “Label-free tetra-modal molecular imaging of living cells with cars, shg, thg and tsfg (coherent anti-stokes raman scattering, second harmonic generation, third harmonic generation and third-order sum frequency generation),” *Opt. Express*, vol. 20, pp. 9551–9557, Apr 2012.
- [20] R. Shimada, H. Kano, and H. Hamaguchi, “Hyper-raman microspectroscopy: a new ap-

- proach to completing vibrational spectral and imaging information under a microscope,” *Opt. Lett.*, vol. 31, pp. 320–322, Feb 2006.
- [21] H.-J. van Manen, Y. M. Kraan, D. Roos, and C. Otto, “Intracellular chemical imaging of heme-containing enzymes involved in innate immunity using resonance raman microscopy,” *The Journal of Physical Chemistry B*, vol. 108, pp. 18762–18771, Dec 2004.
- [22] J.-X. Cheng, Y. K. Jia, G. Zheng, and X. S. Xie, “Laser-scanning coherent anti-stokes raman scattering microscopy and applications to cell biology,” *Biophysical Journal*, vol. 83, no. 1, pp. 502–509, 2002.
- [23] S. Roy, J. R. Gord, and A. K. Patnaik, “Recent advances in coherent anti-stokes raman scattering spectroscopy: Fundamental developments and applications in reacting flows,” *Progress in Energy and Combustion Science*, vol. 36, no. 2, pp. 280–306, 2010.
- [24] D. Pestov, R. K. Murawski, G. O. Ariunbold, X. Wang, M. Zhi, A. V. Sokolov, V. A. Sautenkov, Y. V. Rostovtsev, A. Dogariu, Y. Huang, and M. O. Scully, “Optimizing the laser-pulse configuration for coherent raman spectroscopy,” *Science*, vol. 316, no. 5822, pp. 265–268, 2007.
- [25] A. B. Fedotov, A. M. Zheltikov, L. A. Mel’nikov, A. P. Tarasevitch, and D. von der Linde, “Spectral broadening of femtosecond laser pulses in fibers with a photonic-crystal cladding,” *Journal of Experimental and Theoretical Physics Letters*, vol. 71, pp. 281–284, Apr 2000.
- [26] N. G. R. Broderick, T. M. Monro, P. J. Bennett, and D. J. Richardson, “Nonlinearity in holey optical fibers: measurement and future opportunities,” *Opt. Lett.*, vol. 24, pp. 1395–1397, Oct 1999.
- [27] W. Reeves, J. Knight, P. Russell, and P. Roberts, “Demonstration of ultra-flattened dispersion in photonic crystal fibers,” *Opt. Express*, vol. 10, pp. 609–613, Jul 2002.
- [28] J. Knight, J. Arriaga, T. Birks, A. Ortigosa-Blanch, W. Wadsworth, and P. Russell, “Anomalous dispersion in photonic crystal fiber,” *IEEE Photonics Technology Letters*, vol. 12, no. 7, pp. 807–809, 2000.
- [29] E. P. Ippen and C. V. Shank, “Dynamic spectroscopy and sub-picosecond pulse compres-

- sion,” *Appl. Phys. Lett.*, vol. 27, no. 9, p. 488, 1975.
- [30] D. E. Spence, J. M. Evans, W. E. Sleat, and W. Sibbett, “Regeneratively initiated self-mode-locked ti:sapphire laser,” *Opt. Lett.*, vol. 16, no. 22, pp. 1762–1764, 1991.
- [31] M. Shutova, A. D. Shutov, A. A. Zhdanova, J. V. Thompson, and A. V. Sokolov, “Coherent raman generation controlled by wavefront shaping,” *Sci. Rep.*, vol. 9, no. 1, p. 1565, 2019.
- [32] A. V. Sokolov and S. E. Harris, “Ultrashort pulse generation by molecular modulation,” *J. Opt. B Quantum Semiclass. Opt.*, vol. 5, pp. R1–R26, 2003.
- [33] N. Zhavoronkov and G. Korn, “Generation of single intense short optical pulses by ultrafast molecular phase modulation,” *Phys. Rev. Lett.*, vol. 88, no. 20, p. 203901, 2002.
- [34] T. Suzuki, H. Masataka, and M. Katsuragawa, “Octave-Spanning Raman Comb with Carrier Envelope Offset Control,” *Phys. Rev. Lett.*, vol. 101, p. 243602, 2008.
- [35] S. E. Harris, “Refractive-index control with strong fields,” *Opt. Lett.*, vol. 19, pp. 2018–2020, Dec 1994.
- [36] S. E. Harris and A. V. Sokolov, “Broadband spectral generation with refractive index control,” *Phys. Rev. A*, vol. 55, pp. R4019–R4022, Jun 1997.
- [37] D. D. Yavuz, A. V. Sokolov, and S. E. Harris, “Eigenvectors of a raman medium,” *Phys. Rev. Lett.*, vol. 84, pp. 75–78, Jan 2000.
- [38] A. P. Hickman, J. A. Paisner, and W. K. Bischel, “Theory of multiwave propagation and frequency conversion in a raman medium,” *Phys. Rev. A*, vol. 33, pp. 1788–1797, Mar 1986.
- [39] F. L. Kien, K. Hakuta, and A. V. Sokolov, “Pulse compression by parametric beating with a prepared raman coherence,” *Phys. Rev. A*, vol. 66, p. 023813, Aug 2002.
- [40] *“The CVD diamond booklet”*. Diamond Materials: Advanced Diamond Technology, 2014.
- [41] R. Trebino, *Frequency-Resolved Optical Gating: The Measurement of Ultrashort Laser Pulses*. US, New York: Springer, 2000.
- [42] D. J. Kane, “Principal components generalized projections: a review

*invited*

- ,” *J. Opt. Soc. Am. B*, vol. 25, pp. A120–A132, Jun 2008.
- [43] D. Kane, “Real-time measurement of ultrashort laser pulses using principal component generalized projections,” *IEEE Journal of Selected Topics in Quantum Electronics*, vol. 4, no. 2, pp. 278–284, 1998.
- [44] K. W. DeLong, D. N. Fittinghoff, R. Trebino, B. Kohler, and K. Wilson, “Pulse retrieval in frequency-resolved optical gating based on the method of generalized projections,” *Opt. Lett.*, vol. 19, pp. 2152–2154, Dec 1994.
- [45] D. Kane, “Real-time measurement of ultrashort laser pulses using principal component generalized projections,” *IEEE Journal of Selected Topics in Quantum Electronics*, vol. 4, no. 2, pp. 278–284, 1998.
- [46] P. Couillet, L. Gil, and F. Rocca, “Optical vortices,” *Optics Communications*, vol. 73, no. 5, pp. 403–408, 1989.
- [47] M. Brambilla, F. Battipede, L. A. Lugiato, V. Penna, F. Prati, C. Tamm, and C. O. Weiss, “Transverse laser patterns. i. phase singularity crystals,” *Phys. Rev. A*, vol. 43, pp. 5090–5113, May 1991.
- [48] L. Allen, M. W. Beijersbergen, R. J. C. Spreeuw, and J. P. Woerdman, “Orbital angular momentum of light and the transformation of laguerre-gaussian laser modes,” *Phys. Rev. A*, vol. 45, pp. 8185–8189, Jun 1992.
- [49] J. Leach, E. Yao, and M. J. Padgett, “Observation of the vortex structure of a non-integer vortex beam,” *New Journal of Physics*, vol. 6, p. 71, jul 2004.
- [50] P. Hansinger, G. Maleshkov, I. L. Garanovich, D. V. Skryabin, D. N. Neshev, A. Dreischuh, and G. G. Paulus, “Vortex algebra by multiply cascaded four-wave mixing of femtosecond optical beams,” *Opt. Express*, vol. 22, pp. 11079–11089, May 2014.
- [51] W. J. Firth and D. V. Skryabin, “Optical solitons carrying orbital angular momentum,” *Phys. Rev. Lett.*, vol. 79, pp. 2450–2453, Sep 1997.
- [52] C. W. Clark, R. Barankov, M. G. Huber, M. Arif, D. G. Cory, and D. A. Pushin, “Controlling neutron orbital angular momentum,” *Nature*, vol. 525, pp. 504–506, Sep 2015.

- [53] F. Tamburini, G. Anzolin, G. Umbriaco, A. Bianchini, and C. Barbieri, “Overcoming the rayleigh criterion limit with optical vortices,” *Phys. Rev. Lett.*, vol. 97, p. 163903, Oct 2006.
- [54] H. He, M. E. J. Friese, N. R. Heckenberg, and H. Rubinsztein-Dunlop, “Direct observation of transfer of angular momentum to absorptive particles from a laser beam with a phase singularity,” *Phys. Rev. Lett.*, vol. 75, pp. 826–829, Jul 1995.
- [55] L. Paterson, M. P. MacDonald, J. Arlt, P. E. B. W. Sibbett, and K. Dholakia, “Controlled rotation of optically trapped microscopic particles,” *Science*, vol. 292, pp. 912–914, 2001.
- [56] B. Thidé, H. Then, J. Sjöholm, K. Palmer, J. Bergman, T. D. Carozzi, Y. N. Istomin, N. H. Ibragimov, and R. Khamitova, “Utilization of photon orbital angular momentum in the low-frequency radio domain,” *Phys. Rev. Lett.*, vol. 99, p. 087701, Aug 2007.
- [57] L. Yan, P. Gregg, E. Karimi, A. Rubano, L. Marrucci, R. Boyd, and S. Ramachandran, “Q-plate enabled spectrally diverse orbital-angular-momentum conversion for stimulated emission depletion microscopy,” *Optica*, vol. 2, pp. 900–903, Oct 2015.
- [58] G. I. Petrov, R. Arora, V. V. Yakovlev, X. Wang, A. V. Sokolov, and M. O. Scully, “Comparison of coherent and spontaneous raman microspectroscopies for noninvasive detection of single bacterial endospores,” *Proceedings of the National Academy of Sciences*, vol. 104, no. 19, pp. 7776–7779, 2007.
- [59] M. D. Levenson, *Introduction to nonlinear laser spectroscopy*. Reading, Mass.: New York : Academic Press, 1982.
- [60] J.-X. . Cheng and X. Xie, *Coherent Raman Scattering Microscopy*. CRC Press, 2012.
- [61] M. D. Levenson and S. S. Kano, *Introduction to Nonlinear Laser Spectroscopy*. Academic Press, 1988.
- [62] A. B. Fedotov, S. O. Konorov, V. P. Mitrokhin, E. E. Serebryannikov, and A. M. Zheltikov, “Coherent anti-stokes raman scattering in isolated air-guided modes of a hollow-core photonic-crystal fiber,” *Phys. Rev. A*, vol. 70, p. 045802, Oct 2004.
- [63] R. W. Boyd, *Nonlinear Optics*. Academic Press, 2010.
- [64] B. M. Trabold, R. J. R. Hupfer, A. Abdolvand, and P. St J Russell, “Broadband high-

- resolution multi-species CARS in gas-filled hollow-core photonic crystal fiber,” *Opt Lett*, vol. 42, pp. 3283–3286, Sept. 2017.
- [65] F. Yu, W. J. Wadsworth, and J. C. Knight, “Low loss silica hollow core fibers for 3–4  $\mu\text{m}$  spectral region,” *Opt. Express*, vol. 20, no. 10, pp. 11153–11158, 2012.
- [66] T. Wu, Y. Shao, Y. Wang, S. Cao, W. Cao, F. Zhang, C. Liao, J. He, Y. Huang, M. Hou, and Y. Wang, “Surface plasmon resonance biosensor based on gold-coated side-polished hexagonal structure photonic crystal fiber,” *Opt. Express*, vol. 25, no. 17, pp. 20313–20322, 2017.
- [67] R. van Uden, R. Amezcua-Correa, E. Antonio-Lopez, F. M. Huijskens, C. Xia, G. Li, A. Schülzgen, H. de Waardt, , A. Koonen, and C. Okonkwo, “Ultra-high-density spatial division multiplexing with a few-mode multicore fibre,” *Nature Photonics*, vol. 8, no. 11, pp. 865–870, 2014.
- [68] C. Wang, W. Jin, W. Jin, J. Ju, J. Ma, and L. Ho, “Evanescent-field photonic microcells and their applications in sensing,” *Industrial Metrology*, vol. 79, pp. 172–181, 2016.
- [69] B. Debord, F. Amrani, L. Vincetti, F. Gérôme, and F. Benabid, “Hollow-core fiber technology: The rising of “gas photonics”,” *Fibers*, vol. 7, no. 2, 2019.
- [70] R. Buczynski, “Photonic crystal fibers,” *Acta Physica Polonica Series B*, vol. 106, no. 2, pp. 141–167, 2004.
- [71] M. Nikodem, G. Gomôka, M. Klimczak, D. Pysz, and R. Buczyński, “Demonstration of mid-infrared gas sensing using an anti-resonant hollow core fiber and a quantum cascade laser,” *Opt. Express*, vol. 27, no. 25, pp. 36350–36357, 2019.
- [72] Z. Liu and H. Tam, “Fabrication and sensing applications of special microstructured optical fibers,” *Selected Topics on Optical Fiber Technologies and Applications*, 2017.
- [73] S. O. Konorov, A. B. Fedotov, D. A. Sidorov-Biryukov, V. I. Beloglazov, N. B. Skibina, A. V. Shcherbakov, and A. M. Zheltikov, “Hollow-core photonic-crystal fibers optimized for four-wave mixing and coherent anti-stokes raman scattering,” *Journal of Raman Spectroscopy*, vol. 34, no. 9, pp. 688–692, 2003.

- [74] J. D. Joannopoulos, S. G. Johnson, J. N. Winn, and R. D. Meade, *Photonic Crystals: Molding the Flow of Light - Second Edition*. Princeton University Press, rev - revised, 2 ed., 2008.
- [75] P. Jaworski, “A review of antiresonant Hollow-Core Fiber-Assisted spectroscopy of gases,” *Sensors (Basel)*, vol. 21, Aug. 2021.
- [76] R. M. Carter, F. Yu, W. J. Wadsworth, J. D. Shephard, T. Birks, J. C. Knight, and D. P. Hand, “Measurement of resonant bend loss in anti-resonant hollow core optical fiber,” *Opt. Express*, vol. 25, pp. 20612–20621, Aug 2017.
- [77] K. T. Gahagan and G. A. Swartzlander, “Optical vortex trapping of particles,” *Opt. Lett.*, vol. 21, pp. 827–829, Jun 1996.
- [78] G. D. M. Jeffries, J. S. Edgar, Y. Zhao, J. P. Shelby, C. Fong, and D. T. Chiu, “Using polarization-shaped optical vortex traps for single-cell nanosurgery,” *Nano Letters*, vol. 7, no. 2, pp. 415–420, 2007. PMID: 17298009.
- [79] B. Wetzal, C. Xie, P.-A. Lacourt, J. M. Dudley, and F. Courvoisier, “Femtosecond laser fabrication of micro and nano-disks in single layer graphene using vortex bessel beams,” *Applied Physics Letters*, vol. 103, no. 24, p. 241111, 2013.
- [80] F. Cardano and L. Marrucci, “Spin-orbit photonics,” *Nature Photonics*, vol. 9, pp. 776–778, Dec 2015.
- [81] A. Bezryadina, D. N. Neshev, A. S. Desyatnikov, J. Young, Z. Chen, and Y. S. Kivshar, “Observation of topological transformations of optical vortices in two-dimensional photonic lattices,” *Opt. Express*, vol. 14, pp. 8317–8327, Sep 2006.
- [82] A. Pryamikov, G. Alagashev, G. Falkovich, and S. Turitsyn, “Light transport and vortex-supported wave-guiding in micro-structured optical fibres,” *Scientific Reports*, vol. 10, p. 2507, Feb 2020.
- [83] A. Mair, A. Vaziri, G. Weihs, and A. Zeilinger, “Entanglement of the orbital angular momentum states of photons,” *Nature*, vol. 412, pp. 313–316, 2001.
- [84] Y. Shen, X. Wang, Z. Xie, C. Min, X. Fu, Q. Liu, M. Gong, and X. Yuan, “Optical vortices

- 30 years on: OAM manipulation from topological charge to multiple singularities,” *Light: Science & Applications*, vol. 8, p. 90, Oct 2019.
- [85] A. E. Siegman, *Lasers*. University science books, 1986.
- [86] E. J. Galvez, “Chapter 3 - singular optics and phase properties,” in *Structured Light and Its Applications* (D. L. ANDREWS, ed.), pp. 63–77, Burlington: Academic Press, 2008.
- [87] L. G. Gouy, *Sur une propriete nouvelle des ondes lumineuses*. Paris : Gauthier-Villars, 1890.
- [88] A. V. Gorbach and D. V. Skryabin, “Cascaded generation of multiply charged optical vortices and spatiotemporal helical beams in a raman medium,” *Phys. Rev. Lett.*, vol. 98, p. 243601, Jun 2007.
- [89] T. Roger, J. J. F. Heitz, E. M. Wright, and D. Faccio, “Non-collinear interaction of photons with orbital angular momentum,” *Scientific reports*, vol. 3, p. 3491, 2013.
- [90] J. Strohaber, M. Zhi, A. V. Sokolov, A. A. Kolomenskii, G. G. Paulus, and H. A. Schuessler, “Coherent transfer of optical orbital angular momentum in multi-order raman sideband generation,” *Opt. Lett.*, vol. 37, no. 16, pp. 3411–3413, 2012.
- [91] A. A. Zhdanova, M. Shutova, A. Bahari, M. Zhi, and A. V. Sokolov, “Topological charge algebra of optical vortices in nonlinear interactions,” *Opt. Express*, vol. 23, no. 26, pp. 34109–34117, 2015.
- [92] R. Trebino, K. W. DeLong, D. N. Fittinghoff, J. N. Sweetser, M. A. Krumbügel, B. A. Richman, and D. J. Kane, “Measuring ultrashort laser pulses in the time-frequency domain using frequency-resolved optical gating,” *Review of Scientific Instruments*, vol. 68, no. 9, pp. 3277–3295, 1997.
- [93] I. Shpinkov, I. Kamenskikh, M. Kirm, V. Kolobanov, V. Mikhailin, A. Vasilev, and G. Zimmerer, “Optical functions and luminescence quantum yield of lead tungstate,” *physica status solidi (a)*, vol. 170, no. 1, pp. 167–173, 1998.
- [94] K. J. Moh, X. C. Yuana, D. Y. Tang, W. C. Cheong, and L. S. Zhang, “Generation of femtosecond optical vortices using a single refractive optical element,” *Appl. Phys. Lett.*, vol. 88,

2006.

- [95] J. Liao, X. Wang, W. Sun, Y. Tan, D. Kong, Y. Nie, J. Qi, H. Jia, J. Liu, J. Yang, J. Tan, and X. Li, “Analysis of femtosecond optical vortex beam generated by direct wave-front modulation,” *Optical Engineering*, vol. 52, no. 10, pp. 1 – 8, 2013.
- [96] P. Vaity, J. Banerji, and R. Singh, “Measuring the topological charge of an optical vortex by using a tilted convex lens,” *Physics Letters A*, vol. 377, no. 15, pp. 1154–1156, 2013.
- [97] M. Harris, C. A. Hill, P. R. Tapster, and J. M. Vaughan, “Laser modes with helical wave fronts,” *Phys. Rev. A*, vol. 49, pp. 3119–3122, Apr 1994.
- [98] R. L. Phillips and L. C. Andrews, “Spot size and divergence for laguerre gaussian beams of any order,” *Appl. Opt.*, vol. 22, pp. 643–644, Mar 1983.
- [99] S. G. Reddy, S. Prabhakar, A. Kumar, J. Banerji, and R. P. Singh, “Higher order optical vortices and formation of speckles,” *Opt. Lett.*, vol. 39, pp. 4364–4367, Aug 2014.
- [100] A. H. Zewail, “Femtochemistry: Ultrafast Dynamics of the Chemical Bond,” *J. Phys. Chem. A*, vol. 104, no. 24, pp. 5660–5694, 2000.
- [101] P. B. Corkum and F. Krausz, “Attosecond science,” *Nat. Phys.*, vol. 3, pp. 381–387, 2007.
- [102] A. Weiner, *Ultrafast Optics*. New York: Wiley, 2009.
- [103] M. Nisoli, S. D. Silvestri, O. Svelto, R. Szipöcs, K. Ferencz, C. Spielmann, S. Sartania, and F. Krausz, “Compression of high-energy laser pulses below 5 fs,” *Opt. Lett.*, vol. 22, pp. 522–524, apr 1997.
- [104] H.-S. Chan, Z.-M. Hsieh, W.-H. Liang, A. Kung, C.-K. Lee, C.-J. Lai, R.-P. Pan, and L.-H. Peng, “Synthesis and Measurement of Ultrafast Waveforms From Five Discrete Optical Harmonics,” *Science (80-. )*, vol. 331, pp. 1165–1168, 2011.
- [105] I. Christov, M. M. Murnane, and H. C. Kapteyn, “High-Harmonic Generation of Attosecond Pulses in the “Single-Cycle” Regime,” *Phys. Rev. Lett.*, vol. 78, no. 7, pp. 1251–1254, 1997.
- [106] G. Farkas and C. Tóth, “Proposal for attosecond light pulse generation using laser induced multiple-harmonic conversion processes in rare gases,” *Phys. Lett. A*, vol. 168, no. 5-6, pp. 447–450, 1992.

- [107] S. Harris, J. Macklin, and T. Hänsch, “Atomic scale temporal structure inherent to high-order harmonic generation,” *Opt. Commun.*, vol. 100, no. 5-6, pp. 487–490, 1993.
- [108] G. Krauss, S. Lohss, T. Hanke, A. Sell, S. Eggert, R. Huber, and A. Leitenstorfer, “Synthesis of a single cycle of light with compact erbium-doped fibre technology,” *Nat. Photonics*, vol. 4, no. 1, pp. 33–36, 2010.
- [109] A. Wirth, M. Hassan, I. Grguras, J. Gagnon, A. Moulet, T. Luu, S. Pabst, R. Santra, Z. Alahmed, A. Azzeer, V. Yakovlev, V. Pervak, F. Krausz, and E. Goulielmakis, “Synthesized light transients,” *Science*, vol. 334, no. 6053, pp. 195–200, 2011.
- [110] T. Kobayashi and A. Shirakawa, “Sub-10-fs tunable pulses in visible and NIR and visible sub-5fs pulses generated by noncollinear OPA,” *J. Lumin*, vol. 22, no. 87–89, pp. 119–120, 2000.
- [111] D. Herrmann, L. Veisz, R. Tautz, F. Tavella, K. Schmid, V. Pervak, and F. Krausz, “Generation of sub-three-cycle, 16 TW light pulses by using noncollinear optical parametric chirped-pulse amplification,” *Opt. Lett.*, vol. 34, no. 16, pp. 2459–2461, 2009.
- [112] Y. Y. Wang, C. Wu, F. Couny, M. G. Raymer, and F. Benabid, “Quantum-fluctuation-initiated coherence in multioctave Raman optical frequency combs,” *Phys. Rev. Lett.*, vol. 105, p. 123603, 2010.
- [113] D. Yavuz, “High-frequency modulation of continuous-wave laser beams by maximally coherent molecules,” *Phys. Rev. A*, vol. 76, p. 011805, 2007.
- [114] D. Gold, J. Weber, and D. Yavuz, “Continuous-Wave Molecular Modulation Using a High-Finesse Cavity,” *Appl. Sci.*, vol. 4, no. 4, pp. 498–514, 2014.
- [115] M. Zhi and A. V. Sokolov, “Broadband generation in a Raman crystal driven by a pair of time-delayed linearly chirped pulses,” *New J. Phys.*, vol. 10, no. 2, p. 025032, 2008.
- [116] K. Wang, M. Zhi, X. Hua, and A. V. Sokolov, “Ultrafast waveform synthesis and characterization using coherent Raman sidebands in a reflection scheme,” *Opt. Express*, vol. 22, no. 18, pp. 21411–21420, 2014.
- [117] K. Wang, A. A. Zhdanova, M. Zhi, X. Hua, and A. V. Sokolov, “Multicolored Femtosec-

- ond Pulse Synthesis Using Coherent Raman Sidebands in a Reflection Scheme,” *Appl. Sci.*, 2015.
- [118] M. Zhi, K. Wang, X. Hua, H. Schuessler, J. Strohaber, and A. V. Sokolov, “Generation of femtosecond optical vortices by molecular modulation in a Raman-active crystal,” *Opt. Express*, vol. 21, no. 23, pp. 27750–27758, 2013.
- [119] G. Stibenz and G. Steinmeyer, “Interferometric frequency-resolved optical gating,” *Opt. Express*, vol. 13, no. 7, pp. 2617–2626, 2005.
- [120] I. Amat-Roldan, I. G. Cormack, P. Loza-Alvarez, E. J. Gualda, and D. Artigas, “Ultrashort pulse characterisation with SHG collinear-FROG,” *Opt. Express*, vol. 12, no. 6, pp. 1169–1178, 2004.
- [121] M. Zhi, K. Wang, X. Hua, and A. V. Sokolov, “Pulse-shaper-assisted phase control of a coherent broadband spectrum of Raman sidebands,” *Opt. Lett.*, vol. 36, no. 20, pp. 4032–4, 2011.
- [122] J. Hyyti, E. Escoto, G. Steinmeyer, and T. Witting, “Interferometric time-domain ptychography for ultrafast pulse characterization,” *Opt. Lett.*, vol. 42, no. 11, pp. 2185–2188, 2017.
- [123] R. Trebino, “Trebino-Group Code Code for Retrieving a Pulse Intensity and Phase from Its FROG Trace,” 2016.
- [124] Semrock, “Dichroic GDD Values - Personal Correspondence,” 2017.
- [125] W.-J. Chen, Z.-M. Hsieh, S. W. Huang, H.-Y. Su, C.-J. Lai, T.-T. Tang, C.-H. Lin, C.-K. Lee, R.-P. Pan, C.-L. Pan, and A. H. Kung, “Sub-single-cycle optical pulse train with constant carrier envelope phase,” *Phys. Rev. Lett.*, vol. 100, p. 163906, 2008.
- [126] H. R. Telle, G. Steinmeyer, A. E. Dunlop, J. Stenger, D. H. Sutter, and U. Keller, “Carrier-envelope offset phase control: A novel concept for absolute optical frequency measurement and ultrashort pulse generation,” *Appl. Phys. B Lasers Opt.*, vol. 69, no. 4, pp. 327–332, 1999.
- [127] R. W. Boyd, *Nonlinear Optics*. London, UK: Academic Press, 2010.
- [128] M. Kress, T. Löffler, S. Eden, M. Thomson, and H. G. Roskos, “Terahertz-pulse genera-

- tion by photoionization of air with laser pulses composed of both fundamental and second-harmonic waves,” *Opt. Lett.*, vol. 29, pp. 1120–1122, May 2004.
- [129] D. J. Cook and R. M. Hochstrasser, “Intense terahertz pulses by four-wave rectification in air,” *Opt. Lett.*, vol. 25, pp. 1210–1212, Aug 2000.
- [130] A. V. Sokolov, D. R. Walker, D. D. Yavuz, G. Y. Yin, and S. E. Harris, “Femtosecond light source for phase-controlled multiphoton ionization,” *Phys. Rev. Lett.*, vol. 87, Jun 2001.
- [131] C. Wei, R. J. Weiblen, C. R. Menyuk, and J. Hu, “Negative curvature fibers,” *Adv. Opt. Photon.*, vol. 9, pp. 504–561, Sep 2017.
- [132] J. Nold, P. Hölzer, N. Y. Joly, G. K. L. Wong, A. Nazarkin, A. Podlipensky, M. Scharrer, and P. S. Russell, “Pressure-controlled phase matching to third harmonic in ar-filled hollow-core photonic crystal fiber,” *Opt. Lett.*, vol. 35, pp. 2922–2924, Sep 2010.
- [133] A. Börzsönyi, Z. Heiner, M. P. Kalashnikov, A. P. Kovács, and K. Osvay, “Dispersion measurement of inert gases and gas mixtures at 800 nm,” *Appl. Opt.*, vol. 47, pp. 4856–4863, Sep 2008.
- [134] J. Broeng, D. Mogilevstev, S. E. Barkou, and A. Bjarklev, “Photonic crystal fibers: A new class of optical waveguides,” *Optical Fiber Technology*, vol. 5, no. 3, pp. 305–330, 1999.
- [135] F. Benabid and P. Roberts, “Linear and nonlinear optical properties of hollow core photonic crystal fiber,” *Journal of Modern Optics*, vol. 58, no. 2, pp. 87–124, 2011.
- [136] P. Russell, “Photonic crystal fibers,” *Science*, vol. 299, no. 5605, pp. 358–362, 2003.
- [137] P. Russell, P. Hölzer, W. Chang, A. Abdolvand, and J. Travers, “Hollow-core photonic crystal fibres for gas-based nonlinear optics,” *Nature Photon*, vol. 8, p. 278–286, 2014.
- [138] G. Peeters, R. and Berden, A. Apituley, and G. Meijer, “Open-path trace gas detection of ammonia based on cavity-enhanced absorption spectroscopy,” *Appl. Phys. B*, vol. 71, pp. 231–236, Aug 2000.
- [139] X. Li, Y. Xia, L. Zhan, and J. Huang, “Near-confocal cavity-enhanced raman spectroscopy for multitrace-gas detection,” *Opt. Lett.*, vol. 33, pp. 2143–2145, Sep 2008.
- [140] G. He, D. Liu, and S. hao Liu, “Coherent raman spectra and raman-enhanced self-focusing

- in multimode fiber,” *Optics Communications*, vol. 70, pp. 145–150, 1989.
- [141] S. Brustlein, P. Berto, R. Hostein, P. Ferrand, C. Billaudeau, D. Marguet, A. Muir, J. Knight, and H. Rigneault, “Double-clad hollow core photonic crystal fiber for coherent raman endoscope,” *Opt. Exp.*, vol. 19, pp. 12562–12568, Jun 2011.
- [142] A. D. Pryamikov, A. S. Biriukov, A. F. Kosolapov, V. G. Plotnichenko, S. L. Semjonov, and E. M. Dianov, “Demonstration of a waveguide regime for a silica hollow - core microstructured optical fiber with a negative curvature of the core boundary in the spectral region  $>$  3.5  $\mu\text{m}$ ,” *Opt. Express*, vol. 19, pp. 1441–1448, Jan 2011.
- [143] M. H. Frosz, J. Nold, T. Weiss, A. Stefani, F. Babic, S. Rammler, and P. Russell, “Five-ring hollow-core photonic crystal fiber with 1.8 db/km loss,” *Opt. Lett.*, vol. 38, pp. 2215–2217, Jul 2013.
- [144] J. C. Knight, “Photonic crystal fibres,” *Nature*, vol. 424, p. 847–851, 2003.
- [145] A. M. Zheltikov, “Colors of thin films, antiresonant phenomena in optical systems, and the limiting loss of modes in hollow optical waveguides,” *UFN*, vol. 51, p. 591, 2008.
- [146] R. Tyumenev, L. Späth, B. M. Trabold, G. Ahmed, M. H. Frosz, and P. Russell, “Pump-probe multi-species cars in a hollow-core pcf with a 20 ppm detection limit under ambient conditions,” *Opt. Lett.*, vol. 44, pp. 2486–2489, May 2019.
- [147] F. Köttig, F. Tani, C. M. Biersach, J. C. Travers, and P. S. Russell, “Generation of microjoule pulses in the deep ultraviolet at megahertz repetition rates,” *Optica*, vol. 4, pp. 1272–1276, Oct 2017.
- [148] Q. Huang, I. Ghimire, J. Yang, N. Fleer, K. Chiang, Y. Wang, S. Gao, P. Wang, S. Banerjee, and H. W. Lee, “Optical modulation in hybrid antiresonant hollow-core fiber infiltrated with vanadium dioxide phase change nanocrystals,” *Opt. Lett.*, vol. 45, pp. 4240–4243, 2020.
- [149] G. L. Eesley, *Coherent Raman Spectroscopy*. Oxford: Pergamon, 1981.
- [150] S. A. Druet and J.-P. E. Taran, “Cars spectroscopy,” *Progress in Quantum Electronics*, vol. 7, no. 1, pp. 1–72, 1981.
- [151] W. Ding, Y. Wang, S. Gao, M. Wang, and P. Wang, “Recent progress in low-loss hollow-core

- anti-resonant fibers and their applications,” *IEEE Journal of Selected Topics in Quantum Electronics*, vol. 26, no. 4, pp. 1–12, 2020.
- [152] S. Gao, Y. Y. Wang, X. L. Liu, W. Ding, and P. Wang, “Bending loss characterization in nodeless hollow-core anti-resonant fiber,” *Opt. Exp.*, vol. 24, pp. 14801–14811, Jun 2016.
- [153] M. Zeisberger, A. Hartung, and M. Schmidt, “Understanding dispersion of revolver-type anti-resonant hollow core fibers,” *Fibers*, vol. 6, p. 68, 09 2018.
- [154] A. Bahari, Y. Shen, and A. V. Sokolov, “Pressure controlled phase matching in kagome pc fiber in picosecond cars,” in *OSA*, p. JTU3A.123, Optical Society of America, 2019.
- [155] Y. Shen, A. A. Voronin, A. M. Zheltikov, S. O’Connor, V. V. Yakovlev, A. V. Sokolov, and M. O. Scully, “Picosecond supercontinuum generation in large mode area photonic crystal fibers for coherent anti-stokes raman scattering microspectroscopy,” *Sci. Rep.*, vol. 8, p. 9526, June 2018.
- [156] J. Niu and J. Xu, “Coupling efficiency of laser beam to multimode fiber,” *Optics Communications*, vol. 274, no. 2, pp. 315–319, 2007.
- [157] R. Selm, M. Winterhalder, A. Zumbusch, G. Krauss, T. Hanke, A. Sell, and A. Leitenstorfer, “Ultrabroadband background-free coherent anti-stokes raman scattering microscopy based on a compact er:fiber laser system,” *Opt. Lett.*, vol. 35, pp. 3282–3284, Oct 2010.
- [158] A. Volkmer, L. D. Book, and X. Xie, “Time-resolved coherent anti-stokes raman scattering microscopy: Imaging based on raman free induction decay,” *Appl. Phys. Lett.*, vol. 80, p. 1505, 2002.
- [159] T. W. Kee, H. Zhao, and M. T. Cicerone, “One-laser interferometric broadband coherent anti-stokes raman scattering,” *Opt. Exp.*, vol. 14, pp. 3631–3640, Apr 2006.
- [160] E. O. Potma, C. L. Evans, and X. S. Xie, “Heterodyne coherent anti-stokes raman scattering imaging,” *Opt. Lett.*, vol. 31, pp. 241–243, 2006.
- [161] I. I. Song, G. L. Eesley, and M. D. Levenson, “Background suppression in coherent raman spectroscopy,” *Appl. Phys. Lett.*, vol. 29, p. 567–569, 1976.
- [162] A. F. Bunkin, S. G. Ivanov, and N. I. Koroteev, “Gas analysis by coherent active raman

- spectroscopy with polarization discrimination,” *Sov. Tech. Phys. Lett.*, vol. 3, pp. 182–184, 1977.
- [163] S. A. Akhmanov, A. F. Bunkin, S. G. Ivanov, and N. I. Koroteev, “Polarization active raman spectroscopy and coherent raman ellipsometry,” *Sov. Phys. JETP*, vol. 47, no. 667, 1978.
- [164] N. I. Koroteev, M. Endemann, and R. L. Byer, “Resolved structure within the broad-band vibrational raman line of liquid  $H_2O$  from polarization coherent anti-stokes raman spectroscopy,” *Phys. Rev. Lett.*, vol. 43, pp. 398–401, Jul 1979.
- [165] J. Oudar, R. W. Smith, and Y. R. Shen, “Polarization-sensitive coherent anti-stokes raman spectroscopy,” *Applied Physics Letters*, vol. 34, no. 11, pp. 758–760, 1979.
- [166] R. P. Lucht, “Three-laser coherent anti-stokes raman scattering measurements of two species,” *Opt. Lett.*, vol. 12, pp. 78–80, Feb 1987.
- [167] P. S. J. Russell, T. A. Birks, and F. D. Lloyd-Lucas, *Photonic Bloch Waves and Photonic Band Gaps*, pp. 585–633. Boston, MA: Springer US, 1995.
- [168] N. M. Litchinitser, A. K. Abeeluck, C. Headley, and B. J. Eggleton, “Antiresonant reflecting photonic crystal optical waveguides,” *Opt. Lett.*, vol. 27, pp. 1592–1594, Sep 2002.
- [169] A. M. Cubillas, X. Jiang, T. G. Euser, N. Taccardi, B. J. M. Etzold, P. Wasserscheid, and P. S. J. Russell, “Photochemistry in a soft-glass single-ring hollow-core photonic crystal fibre,” *Analyst*, vol. 142, pp. 925–929, 2017.
- [170] I. A. Bufetov, A. F. Kosolapov, A. D. Pryamikov, A. V. Gladyshev, A. N. Kolyadin, A. A. Krylov, Y. P. Yatsenko, and A. S. Biriukov, “Revolver hollow core optical fibers,” *Fibers*, vol. 6, no. 2, 2018.
- [171] N. Mahnot, S. Maheshwary, and R. Mehra, “Photonic crystal fiber- an overview,” 2015.
- [172] M. Pospíšilová, G. Kuncová, and J. Trögl, “Fiber-optic chemical sensors and fiber-optic bio-sensors,” *Sensors*, vol. 15, p. 25208–25259, 2015.
- [173] S. O. Konorov, A. M. Zheltikov, and M. Scalora, “Photonic-crystal fiber as a multifunctional optical sensor and sample collector,” *Opt. Express*, vol. 13, no. 9, pp. 3454–3459, 2005.
- [174] N. Rajil, A. Sokolov, Z. Yi, G. Adams, G. Agarwal, V. Belousov, R. Brick, K. Chapin, J. Cir-

illo, V. Deckert, S. Delfan, S. Esmaeili, A. Fernández-González, E. Fry, Z. Han, P. Hemmer, G. Kattawar, M. Kim, M. Lee, C. Lu, J. Mogford, B. Neuman, J. Pan, T. Peng, V. Poor, S. Scully, Y. Shih, S. Suckewer, A. Svidzinsky, A. Verhoef, D. Wang, K. Wang, L. Yang, A. Zheltikov, S. Zhu, S. Zubairy, and M. Scully, “A fiber optic–nanophotonic approach to the detection of antibodies and viral particles of covid-19,” *Nanophotonics*, vol. 10, no. 1, pp. 235–246, 2021.

## APPENDIX A

### BASIC ALIGNMENT METHODS

This appendix is dedicated to some basic but extremely handy information on optimizing the alignment of the setup to generate the coherent Raman sidebands in diamond (or  $\text{PbWO}_4$ ) crystal, and repeat the optimization if needed. Moreover, some data collected by a spectrometer to detect the weak SHG and SFG signals of the coherent Raman sidebands are presented.

Figure A.1 is a visual display of how to achieve the overlap between the two fundamental beams to produce a set of mutually coherent Raman sidebands in the diamond crystal. (a, b, c) Demonstrate the generation of the SFG, FWM, and simultaneous SFG/FWM signals in a 1 mm-thick BBO crystal. It is best to find each beam's SHG signal while the other beam is blocked. This can be done by placing the BBO crystal on a rotating mount. We then adjust the angle to find the best SHG signal for each beam, separately and then adjust the angle right in between the two recorder values. Afterward, we tweak the delay stage of either beam (we keep the stage of the pump fixed and only vary the Stokes' stage) until we observe the SFG signal. By moving the BBO slightly back and forth manually and fine-tuning the mount's angle again, we can observe the SFG, SHGs, and FWM simultaneously. This would be the perfect position to place the diamond. Figure A.1(d) shows the coherent Raman sidebands exiting the diamond after (c) was achieved and BBO was substituted by the diamond. To increase the power of the input beams while avoiding several parasitic effects in the diamond, we place the diamond slightly off-focus. The Raman sidebands' shape and power can be optimized further by changing the time delay on the SDG box as well as resizing the input beams using irises as long as the parasitic effects are avoided. If the trace of the sidebands appears slanted, we tune the vertical spatial overlap between the two beams. Tuning the pulses' chirp can also improve the quality and the power of the sidebands. Every time that we restart the laser system, there is a risk of losing the sidebands due to the optics, mechanical parts, and oscillator's instabilities. If that is the case, we first tune the time delay between the beams.

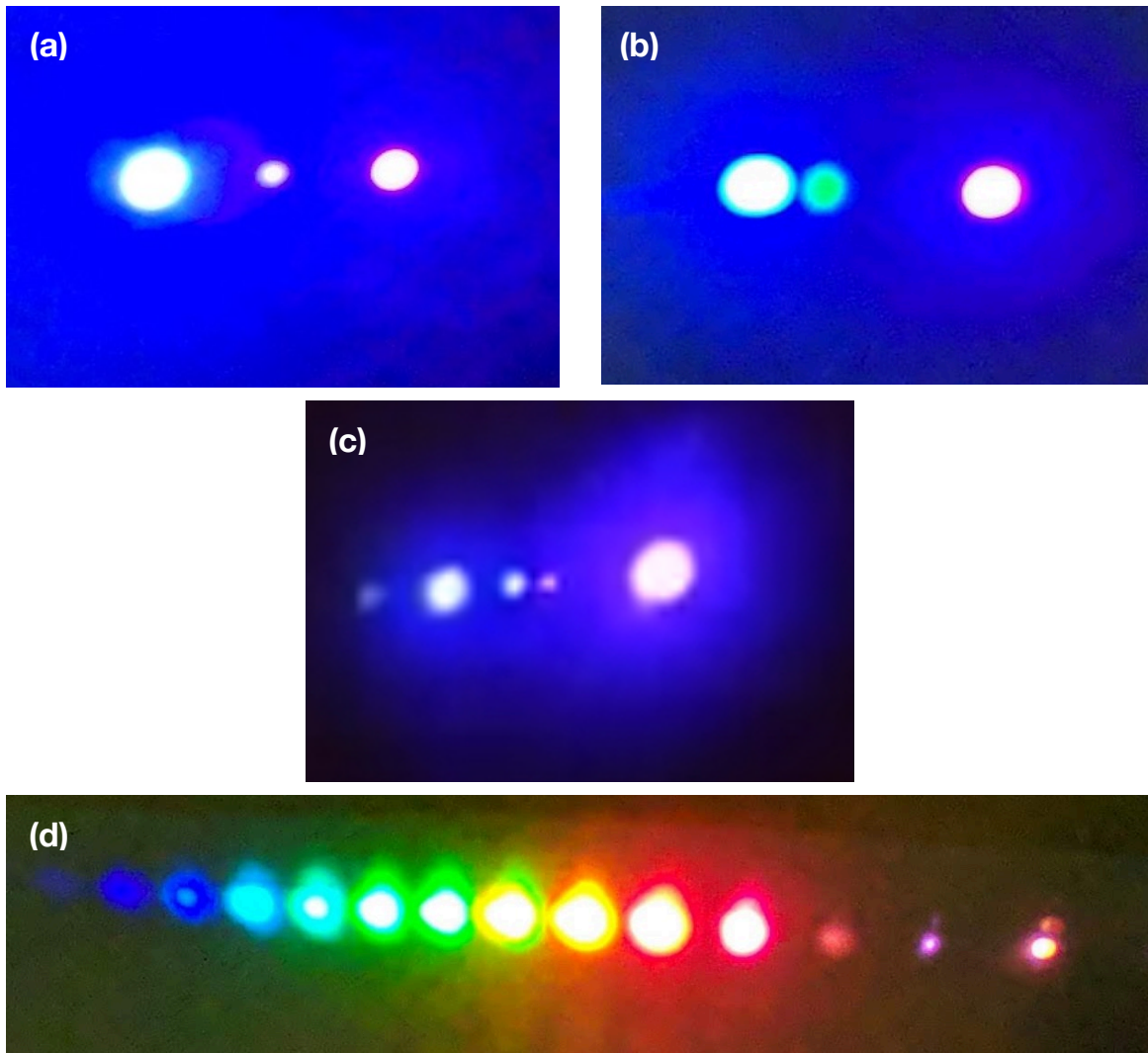


Figure A.1: The overlapping procedure of the pump and Stokes in the BBO and the diamond crystals to generate the multi-color Raman sidebands. Real photos of the SHG of both pump and Stokes beams with (a) their SFG signal in the middle, (b) the FWM signal next to the SHG signal of the pump beam, and (c) both SFG and FWM signals appearing simultaneously. The bright spot on the left side of the SHG of the pump is the reflection of the FWM from a different surface of the diamond. (d) Generation of the coherent Raman sidebands after the diamond. When (c) is observed after the BBO, it means a perfect spatial and temporal overlapping of the two beams. By replacing the BBO with the diamond at the exact same location, sidebands appear with little to no need for extra alignments.

Then, we check the spatial overlap by fiddling with only one designated mirror right before the diamond. If the sidebands did not get restored, we need to run a set of diagnostics and repeat most

of the steps from the beginning. If the sidebands appear, but the power is slightly lower than usual, we would check the OPA (optical parametric amplifier) and adjust the crystal angle and the time delays between the involved beams (delay 1,2 as shown in figure A.2 ) inside it until the power of the Stokes is preserved. These adjustments can be done by changing the numbers on the OPA panel which is shown in figure A.2.



Figure A.2: The OPA panel allows the generation of pulses with adjustable frequencies. The Stokes beam used in chapters 4-6 is the SHG of the idler beam of the OPA. The top four rows allow us to change the wavelength of the Stokes and its power for better results in generating the coherent Raman sidebands. SHG-I stands for the second harmonic generation of the Idler

Figure A.3 illustrates the detection of the weak SFG signal of each sideband in conjugation with the Ref pulse. While for the low-order sidebands SFG signal can be detected by naked eyes (in a dark enough room) or a UV-detecting slow-fading phosphorescent card (250-540 nm, VRC1, Thorlabs), detecting the SFG created by the higher order sidebands with low power is not as simple. Hence, we use a spectrometer to detect the signal while adjust the angle on the BBO crystal's rotating mount and tweak the delay stage as described above.

In figure A.3 (b), the green dotted curves show the SHG of each sideband at their proper angle (these are not shown on the other plots). After each is at its highest, we record the angle and then find the number right in between and set the mount on that number. The SFG does not appear instantly, and we usually need to adjust the time delay between each couple, afterward.

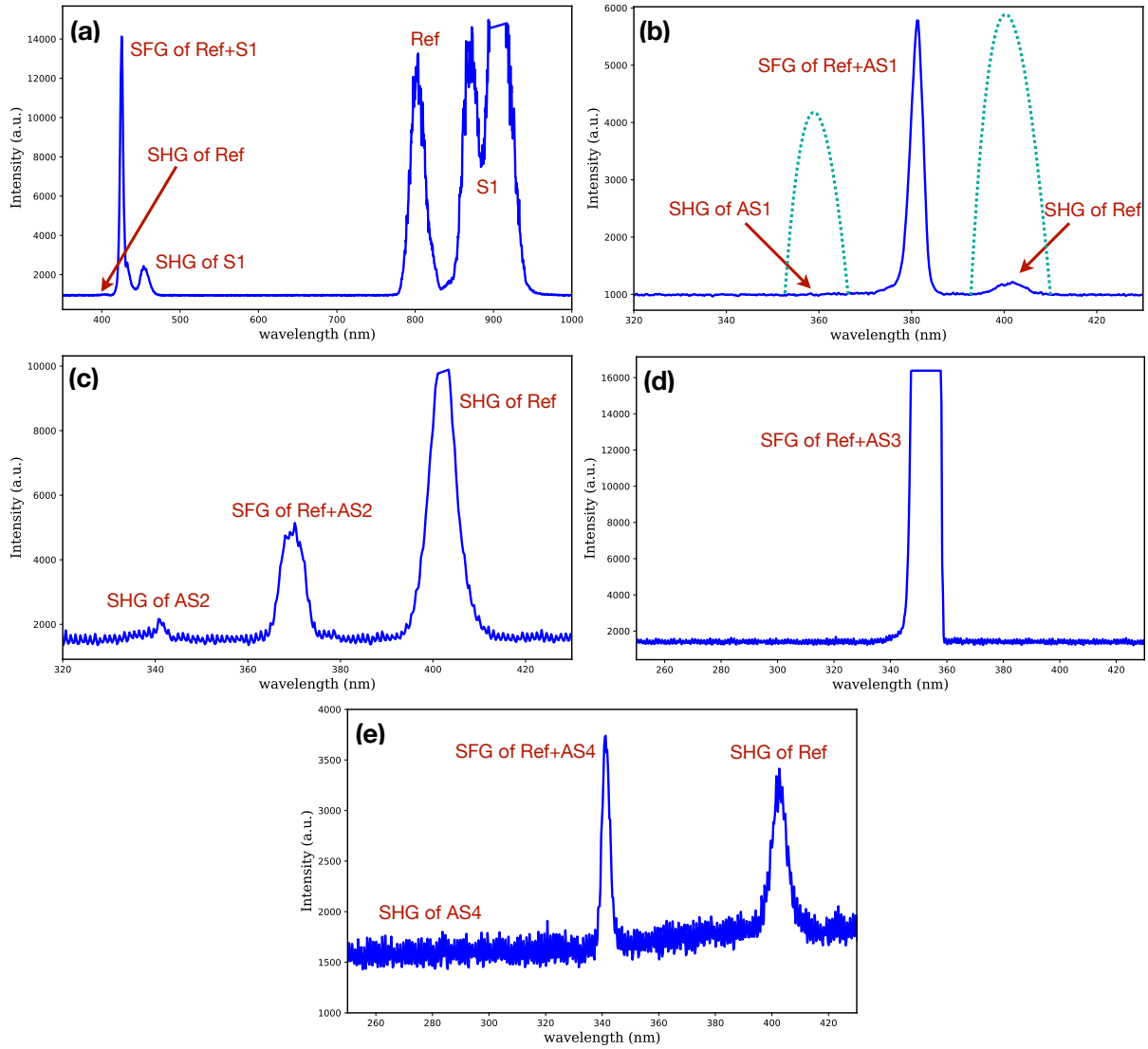


Figure A.3: SFG signal detection for different combinations of the sideband pairs. To find the same frequency of two different sidebands, both beams are focused on the BBO. Then one beam is blocked, and the crystal is rotated until the other beam's SHG signal is detected on the spectrometer. The corresponding angle on the crystal's mount is recorded, and the process is repeated for the second beam. Then, both beams get unblocked, and the mount is set to an angle right in the middle of the two recorded ones. If the beams are aligned well and overlapping both spatially and temporally, their SFG signal should be detectable right in the middle of the two wavelengths. Green dotted lines in (b) show the peak intensity of the SHG signals of each sideband at a different angle. The blue solid line shows the SFG of the combination.

## APPENDIX B

### USING CARS MICROSCOPE FOR BEAM ALIGNMENT

Before detailing the use of our CARS microscope to achieve the best alignment for the CARS in AR-HCF setup (figure 8.2) and overlap the two fundamental pulses (pump and Stokes) in spatial and temporal fashion, in the section below, I briefly describe the CARS microscope that was used for this purpose.

#### **B.1 CARS Microscope Description**

Figure B.1(a) shows our CARS microscope whose main part is a commercial up-right microscope (LV-series, Nikon). Whenever needed, we can easily switch between laser-scanning CARS imaging and bright-field imaging by fixing the top trinocular and using a sliding mirror above the epi-illuminator. We use a 40X reflective objective (LMM-40X-P01, Thorlabs) for the alignment and bright imaging as seen in figure B.1(b,d). The efficiency of the transmission for the fundamentals is 30% after this objective. We then use another objective (20X Plan Fluor, Nikon) with the same numerical aperture (NA) of 0.5 to collect the signal after the sample and send it to the CCD spectrometer. We use proper ND filters to block the strong fundamentals for signal detection. The CARS microscope enables 2D imaging in the horizontal (XY) plane by using a motorized scanning stage (OptiScan, Prior Scientific) with a minimum resolution of 1  $\mu\text{m}$ . For Z-direction scanning, we use two identical z-drives (PS3H122R, Prior Scientific) to move the top and the bottom objectives simultaneously.

#### **B.2 Beam alignment method**

The CARS microscope facilitates the process of setup alignment and fundamental beams' overlap. We record the exact position of each beam (pump and Stokes) on the microscope using a software called uEye Cockpit (UI326xCP-M). Each time the setup needs to be aligned (for example,

when the SC alignment is disturbed due to temperature fluctuation or instability of the stage that the LMA fiber is located on) we refer to the saved position on the software and realign the beams accordingly. The Stokes beam profile captured by the CARS microscope is shown in figure B.1 (d).

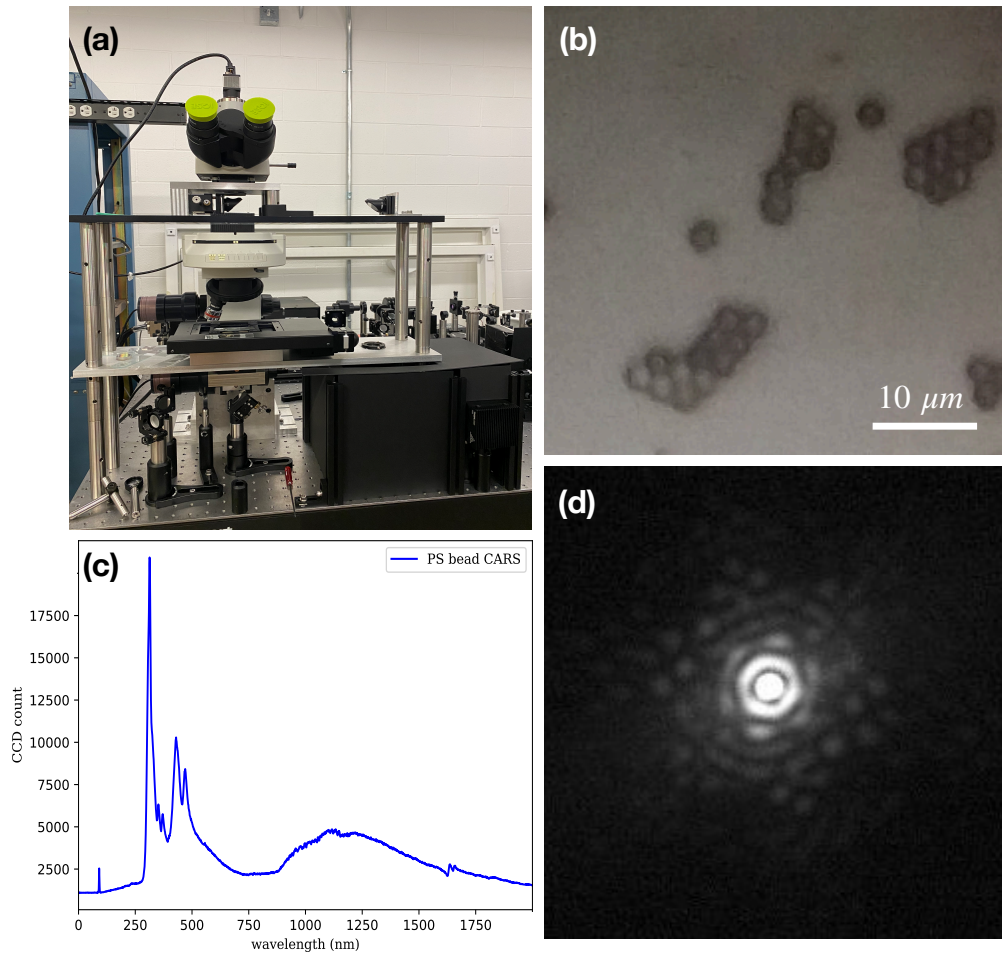


Figure B.1: Using the CARS microscope to align fundamental beams by optimizing the CARS signal of the polystyrene (PS) beads. (a) The CARS microscope, (b) a 2D image of PS beads under the microscope, (c) the CARS signal of the PS beads at  $3050\text{ cm}^{-1}$ , and (d) the beam profile of the Stokes beam under the CARS microscope which illustrates the exact pattern of the SC after exiting the LMA fiber. We then use an iris to clean up the profile to approach a more Gaussian-like profile. By optimizing the CARS signal of the PS beads to reach its highest CCD count, we ensure that the two beams, pump and Stokes, are properly overlapping both spatially and temporally.

For the two fundamental beams' overlapping, we use the same process for a rough alignment and then perform extra fine-tuning by optimizing the CARS signal of polystyrene (PS) beads. We chose PS beads for the alignment because the sample preparation is relatively straightforward, and their CARS signal is easy to detect. Figure B.1 (b) shows the PS beads as singlets and in the cluster under the microscope. Figure B.1 (c) shows the CARS signal of a single PS bead at  $3050\text{ cm}^{-1}$ . By optimizing this signal to its highest CCD count, we ensure that the two beams are perfectly overlapping both spatially and temporally. We achieve the temporal overlap by adjusting the delay stage of the Stokes beam (figure 8.2) located before the microscope.